Development of Micro‑Pattern Gaseous Detectors – Micromegas

Diplomarbeit der Fakultät für Physik
der
Ludwig-Maximilians-Universität München

vorgelegt von
Jonathan Bortfeldt
geboren in Köln

München, den 23.11.2010

Erstgutachter: Prof. Dr. Otmar Biebel
Zweitgutachter: Prof. Dr. Martin Faessler

Abstract

The upgrade of the Large Hadron Collider to sLHC with an increased luminosity of $5 \cdot 10^{34} \, \text{cm}^{-2}\text{s}^{-1}$ and correspondingly increased background rates will result in an occupancy of up to 70% and a considerable degradation of the spatial resolution in the small wheel region of the ATLAS muon spectrometer. Part of the currently installed detectors, monitored drift tubes and cathode strip chambers, will not be able to cope with the expected background rates. In the last years, micro mesh based micro-pattern gas detectors have been developed, known as Micromegas. They have highly segmented readout planes and are intrinsically high rate capable at satisfactory spatial resolution. Large active areas are achievable, such that they present a viable candidate for CSC replacement. The smaller prototypes developed in this thesis will be tested as external track reference for studies with muon MDTs in 140 GeV muon beams or for for position determination of cosmic muons in high background environments of neutrons or γs.

In this thesis $90 \times 100 \, \text{mm}^2$ large bulk Micromegas have been assembled and commissioned. The behavior in measurements with cosmic muons and soft X-rays, emitted by a ^{55}Fe source, will be reported. The readout structure consists of 360 gold and nickel plated copper strips of 100 mm length, 150 µm width and a pitch of 250 µm, having a distance of 128 µm to the micro mesh. The performance of the detector with respect to efficiency, pulse height, energy resolution and spark behavior is investigated, by recording full signal cycles using a single charge sensitive preamplifier and a 1 GHz flash ADC. Thereby all readout strips are connected, forming a single readout plane. The detector currents are remotely monitored. Three different mixtures of Ar:CO_2 are studied, 93:7, 90:10 and 80:20 vol %, resulting in slight advantages of 80:20 vol % at normal pressure. Experimental efficiencies of up to 99% are observed, the energy resolution at FWHM lies at 24%.

A fast 384 channel Gassiplex based strip readout is adapted to negative charge signals by optimizing the circuit around the frontend ADC amplifier. It is furthermore protected against discharges, encountered in Micromegas. Stable operation over several days is possible. A tracking system incorporating three Micromegas allows for reconstructing cosmic muon tracks in two dimensions. The spatial resolution of (62 ± 6) µm is limited by multiple scattering of the low energy cosmic muons. Analysis programs, enabling offline analysis of the data, acquired with the flash ADC and the Gassiplex based strip readout are developed by me.

The signals on anode and mesh are analytically calculated and compared to the measurements. A model, describing the Micromegas' relevant parts as discrete capacitors is developed, enabling the numerical calculation of the detector's response to charge pulses of arbirary shape and height. The agreement between data and expectation is satisfactory.

Kurzfassung

Im Zuge des geplanten Luminositätsupgrades des Large Hadron Colliders zu sLHC mit einer erhöhten Luminosität von $5 \cdot 10^{34}\,\mathrm{cm}^{-2}\mathrm{s}^{-1}$ und einer damit verbundenen Erhöhung der Untergrundrate, wird die Okkupanz von Detektoren im Small Wheel des ATLAS Myon Spektrometers auf bis zu 70% ansteigen. Außerdem wird sich die Ortsauflösung durch Raumladungseffekte deutlich verschlechtern. Ein Teil, der im Moment eingebauten Monitored Drift Tubes und Cathode Strip Chambers, können bei den erwarteten Untergrundraten nicht mehr die geforderte Leistung erbringen. In den letzten Jahren sind mikrostrukturierte Gasdetektoren, genannt Micromegas, unter Verwendung eines gasverstärkenden Mikrogitters entwickelt worden. In Verbindung mit einer hochsegmentierten Auslesestruktur können auch bei sehr hohen Raten Teilchen mit akzeptabler Ortsauflösung und geringer Okkupanz nachgewiesen werden. Da auch große Strukturen realisierbar erscheinen, stellen Micromegas eine gute Möglichkeit dar, um CSCs zu ersetzen. Die zunächst in dieser Arbeit entwickelten kleineren Prototypen sollen versuchsweise als externe Spurreferenz für 140 GeV Myonen oder zur Positionsbestimmung kosmischer Myonen bei starken Neutronen- oder γ-Untergrund eingesetzt werden.

In der vorliegenden Diplomarbeit sind Bulk-Micromegas mit einer aktiven Fläche von $90 \times 100\,\mathrm{mm}^2$ entwickelt und in Betrieb genommen worden. Ihre Charakteristika werden in Messungen mit kosmischen Myonen und niederenergetischer Röntgenstrahlung einer ^{55}Fe Quelle untersucht und vermessen. Die Auslesestruktur, die einen Abstand von 128 µm zum Mikrogitter besitzt, besteht aus 100 mm langen, mit Gold und Nickel beschichteten Kupferstreifen der Breite 150 µm und einer Periodizität von 250 µm. Die Signale eines ladungsempfindlichen Vorverstärkers, der an die miteinander verbundenen Streifen angeschlossen ist, werden mithilfe eines 1 GHz Flash ADCs aufgezeichnet. Dies erlaubt die Parametrisierung des Detektors im Bezug auf Effizienz, Signalhöhe, Energieauflösung und Entladungsverhalten, letzteres durch Slow Control Überwachung der Hochspannung und des Detektorstroms. Drei unterschiedliche Ar:CO_2 Gasmischungen, im Volumenverhältnis 93:7, 90:10 und 80:20 werden untersucht. Nach Variation der Gasmischung und des Drucks zeigen sich leichte Vorteile einer 80:20 Mischung bei Normaldruck. Die Effizienz auf Myonen liegt bei bis zu 99% und die Energieauflösung bei 24% FWHM.

Eine schnelle Ausleseelektronik mit 384 Kanälen, basierend auf Gassiplex Chips, wird durch Optimierung der Beschaltung des Verstärkers am Frontend ADC an negative Ladungssignale angepasst und gegen die Micromegas typischen, negativen Entladungen abgesichert. Ein stabiler Betrieb über mehrere Tage ist möglich. Eine Spurreferenz aus drei Micromegas erlaubt die Rekonstruktion von Spuren kosmischer Myonen in zwei Dimensionen. Die gemessene Ortsauflösung von (62 ± 6) µm wird durch Vielfachstreuung der niederenergetischen kosmischen Myonen begrenzt. Verschiedene Auswertealgorithmen, welche die Analyse der Daten ermöglichen, die mit dem Flash ADC und der Gassiplex Streifenauslese aufgenommen werden, werden von mir entwickelt.

Analytisch berechnete Signalverläufe auf Anode und Mikrogitter werden mit Messungen verglichen. Zusätzlich wird ein Modell entwickelt, das die numerische Berechung der Reaktion des Detektors auf beliebige Ladungssignale ermöglicht. Die wesentlichen Teile des Micromegas werden darin durch Kapazitäten dargestellt. Die Variation der Signalhöhe als Funktion der Streifenzahl und in Abhängigkeit der Mikrogitterkapazität, sowie das Verhalten bei einer Entladung vom Mikrogitter auf die Anode, werden durch eine auf diesem Modell basierende Spice Simulation richtig wiedergegeben.

Contents

Chapter 1

Introduction and Motivation

1.1 The ATLAS Experiment at the Large Hadron Collider

The Large Hadron Collider (LHC) is a proton-proton collider at CERN[1], aiming at the discovery of the elusive Higgs-Boson and physics beyond the standard model of particle physics (fig. 1.1, CERN[2]).

Figure 1.1: The Large Hadron Collider at CERN.

As of now, six experiments have been installed: ATLAS and CMS are large multi-purpose detectors, LHCb is designed to study CP-violation in the B meson sector, TOTEM measures the total pp-cross section, LHCf is meant for investigating the properties of neutral particles in the forward region of ATLAS, and ALICE is designed to study the behavior of quark-gluon plasma, produced in lead ion collisions. The first collisions were observed in 2009, after a year of repairs, necessary after a massive helium leak in the superconducting magnet system

---

[1]European Organization for Nuclear Research, Meyrin
[2]http://lhc-milestones.web.cern.ch/LHC-Milestones/year2008-en.html

in 2008. In March 2010 the operation with protons at a center of mass energy of $7\,\mathrm{TeV}$ was started. Until November 4th, 2010 $49\,\mathrm{pb}^{-1}$ of data were collected[3]. Peak instantaneous luminosities above $10^{32}\,\mathrm{cm}^{-2}\mathrm{s}^{-1}$ have been achieved. The LHC is expected to run from November 7th until December 6th, 2010 with lead ions at a center of mass energy of $287\,\mathrm{TeV}$.

A schematic drawing of the ATLAS[4] experiment can be found in fig. 1.2.

Figure 1.2: Cut away view of the ATLAS detector [G. Aad et al. (The ATLAS Collaboration), 2008].

The experiment consists of several layers of different detector types, both in the barrel and in the endcap region. Close to the collision point, tracking and electron identification is achieved by semiconductor pixel and strip detectors and by straw-tube transition radiation trackers. This inner detector is enclosed by a $2\,\mathrm{T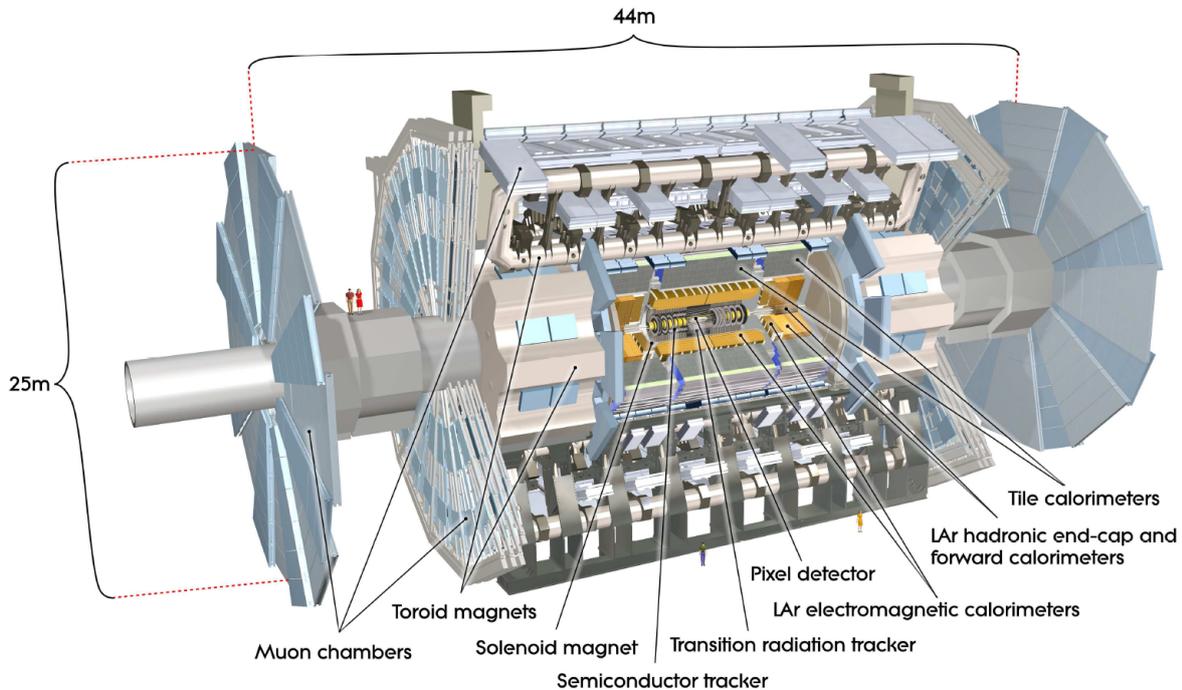}$ solenoidal magnet, needed for momentum measurements and sign of charge determination. Energy is measured in the liquid argon electromagnetic and in the tile hadronic calorimeter, both realized in the barrel and in the endcap region.

The high precision muon system consists of four different types of detectors: Monitored drift tubes (MDT) and cathode strip chambers (CSC), used for precision tracking, resistive plate chambers and thin gap chambers, meant for triggering and providing a second track coordinate. The muon drift tube chambers are constantly monitored by an optical alignment system, to correct for thermal and mechanical deformations. In the barrel region, three layers of MDT chambers in a toroidal, $0.5\,\mathrm{T}$ magnetic field are able to determine the muon momentum, independently of the inner detector. The optimum stand alone momentum accuracy is about 3% for muons with $E_\mu \approx 100\,\mathrm{GeV}$. The same holds for the muon chambers in the small and the two big wheels in the endcap region, where the charged particles' tracks are bent by magnets, providing a $1\,\mathrm{T}$ toroidal field.

The cathode strip chambers are installed in the high rate environment of the small wheel, between the inner tracker and the endcap toroid magnets. They are multi-wire proportional

---

[3]https://twiki.cern.ch/twiki/bin/view/Atlas/AtlasResults
[4]A Toroidal LHC ApparatuS

chambers with cathode strip readout. One cathode plane is finely segmented, leading to a spatial resolution of $60\,\mu m$ in the bending direction of the magnetic field. The other plane is coarsely segmented, resulting in a spatial resolution of $5\,mm$ in the perpendicular plane [G. Aad et al. (The ATLAS Collaboration), 2008].

The LHC's luminosity will be gradually increased within the next couple of years to super LHC (sLHC). The actually build-in detector components in the small wheel region are not suitable for a luminosity of $L = 5 \cdot 10^{34}\,cm^{-2}s^{-1}$, expected to be realized in 2020. The occupancy due to high background rates may be as large as 70% [von Loeben et al., 2010]. Furthermore the spatial resolution of muon drift tubes degrades with increasing background rate, due to space charge effects [Deile et al., 2004].
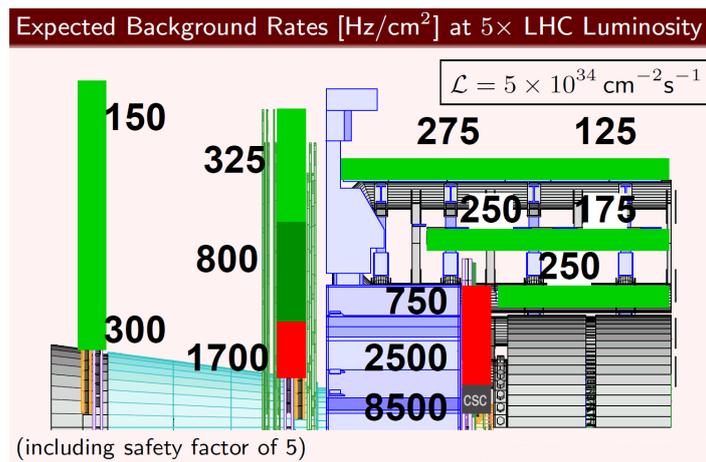

Figure 1.3: Background rates in one quarter of the ATLAS detector at a luminosity of $L = 5 \cdot 10^{34}\,cm^{-2}s^{-1}$, taken from [von Loeben et al., 2010].

Several groups are working on replacements for the CSCs in the small wheel. Conventional drift tubes with $15\,mm$ diameter instead of $30\,mm$ would considerably reduce the occupancy, since the hit area is smaller and the maximum electron drift time is considerably shorter [Bittner et al., 2010]. Nevertheless, the wire detector specific, long drift of positive ions causes a degradation of the spatial resolution in high background environments. Ions, produced in gas avalanche processes in the strong electric field close to the wire, drift from the wire towards the tube. This takes several milliseconds. In this time, they distort the electric field locally, reducing the gas gain and altering the drift times. Another approach for improving the present muon tubes is the use of a faster detector gas with a more linear space-to-drift-time relation. A linear space-to-drift-time relation would diminish the space charge's negative influence [Engl et al., 2010].

A completely different approach is based on a micro-pattern gaseous detector, the Micromegas, that will be introduced in the following section.

1.2 The Micromegas Detector

The Micromegas is an improved parallel plate avalanche counter, introduced by Giomataris et al. [1996]. The acronym stands for MICROMEsh GAseous Structure or for MICROMEsh GAS detector. In the following it will simply be used as the detector's name. It consists of a conductive micro mesh, held by insulating pillars at a distance of around $100\,\mu m$ from the readout structure (fig. 1.4). The readout structure usually consists of strips or pads, printed on a support plate. A drift region is defined by a thin, flat cathode, at a distance of several
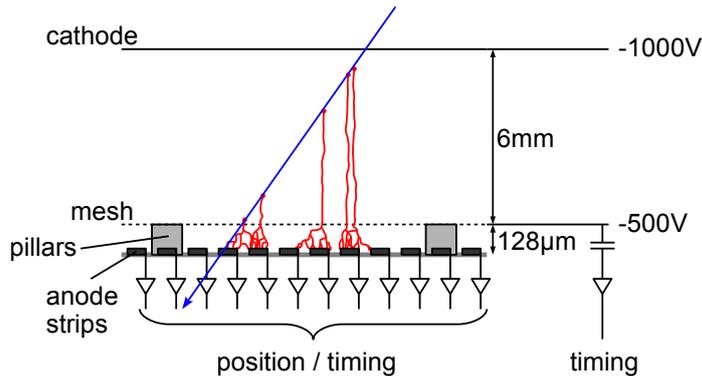
Figure 1.4: Micromegas' functional principle. The 1-2 kV/cm drift field between cathode and mesh separates the positive ions and electrons, created in ionization processes. The electrons drift in some ten nanoseconds into the amplification gap between mesh and anode. There, they start an electron avalanche in the 30-50 kV/cm strong amplification field.

millimeters from the micro mesh. The whole structure is surrounded by a conductive case, providing gas tightness and shielding.

Charged particles ionize the gas in the drift region between the cathode and the mesh. A constant, 1-2 kV/cm strong drift field, makes the electrons drift in some ten nanoseconds towards the mesh. The strong 30-50 kV/cm amplification field around the mesh wires draws the electrons into the amplification region between mesh and anode and accelerates them enough to further ionize the gas. The electrons, created in this gas amplification process, reach the anode strips within 1 ns. The ions drift towards the mesh in about 150 ns, giving rise to the slow component of the signal. A hit-position is deduced by weighting the hit readout strips with their respective pulse height. For readout strips with 150 µm width and 250 µm pitch, spatial resolutions of 30-60 µm were reported. The positive charge signal on the mesh can be used for timing and triggering. The space charge effects encountered in wire chambers, can be largely avoided, due to the ions' much smaller drift time. Together with a fine readout segmentation, Micromegas are thus expected to be intrinsically high rate capable.

Twelve $40 \times 40 \, \text{cm}^2$ large Micromegas are used in the high rate region of the COMPASS experiment at CERN [Bernet et al., 2005]. They encounter single strip count rates of 100-200 kHz, corresponding to $450 \, \text{kHz/cm}^2$ in the high flux zone. At nominal beam intensity, efficiencies of 97%, spatial resolutions of 113 µm and timing resolutions of 9.3 ns have been reported. From 2002-2004 about 1mC/mm^2 of charge was accumulated in the Micromegas' high flux zone, no aging was observed [P. Abbon et al. (The COMPASS Collaboration), 2007].

ATLAS is also working on the development of large Micromegas based chambers, suitable for replacing the small wheel CSCs [Alexopoulos et al., 2010b].

Other groups are planning to use Micromegas in sampling calorimeters [Espargilière et al., 2009] or in time projection chambers [Schade and Kaminski, 2010] for future linear colliders.

In this thesis, the assembling and commissioning of several so called bulk Micromegas will be described (chap. 3). The behavior with respect to cosmics and soft X-rays will be investigated. Two different readout electronics have been set up. In chap. 4 the setup, applying a single preamplifier in combination with a fast flash ADC to record complete charge signals, is described. A modified electronic readout based on Gassiplex chip is used, to read out all 360 strips (chap. 5).

Experimental results are presented in chaps. 6 and 7. It will be shown, that the detector performs best with a gas mixture of Ar:CO$_2$ 80:20 at normal pressure. Efficiencies to cosmics of up to 99% are achieved, the energy resolution of around 25% lies in the expected range (chap. 6). A tracking system, consisting of three Micromegas with 360 strips each was built achieving a spatial resolution of 62 µm. The effect of the mesh supporting pillars is studied (chap. 7).

Apart from investigating the general behavior, a model is developed (chap. 8), allowing for analytically calculating the expected signals and for numerically simulating the detector's signal response.

1.3 Micromegas Based Tracking Systems

Apart from the ATLAS upgrade, necessary under sLHC conditions, three further application of Micromegas are envisaged. Small 15 mm muon drift tubes with the standard gas mixture of Ar:CO$_2$ 93:7 as well as standard 30 mm ATLAS drift tubes, filled with an alternative mixture of Ar:CO$_2$:N$_2$ are tested in the muon beam at the CERN's SPS H8 beam line.
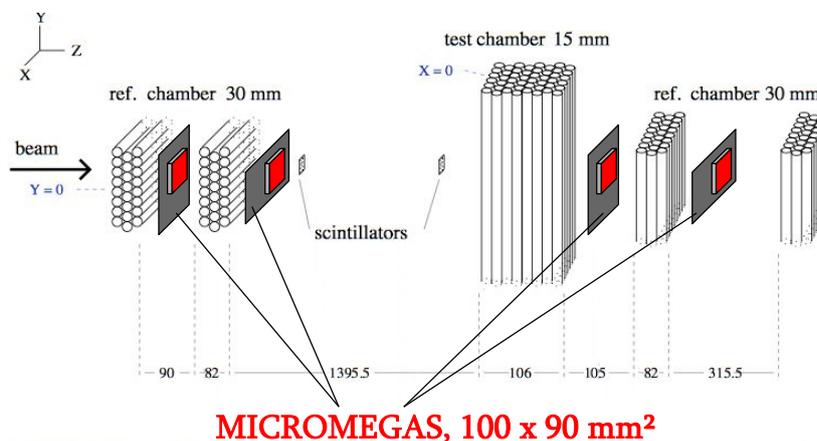

Figure 1.5: *MDT test setup in the CERN H8 experimental area [Engl, 2010]. The reference system, at the moment consisting of standard MDT detectors could be replaced by a Micromegas track reference, consisting of six to eight strip detectors.*

An external, high rate capable track reference system would simplify the offline analysis considerably, providing an unbiased track information independent of internal shifts and twists, regularly observed for MDT chambers. At the moment, standard MDT detectors are used as track reference. The track reference should have a spatial resolution of about 40-60 µm, twice as good as the mean MDT's resolution. Since the beam size, determined by the trigger, is about $8 \times 8 \, \text{cm}^2$, the small Micromegas in combination with the fast Gassiplex based strip readout, presented in this thesis would be suitable for this purpose.

Recently, small ATLAS muon tubes were irradiated with 20 MeV protons at the Munich tandem accelerator[5]. Furthermore, a neutron source, providing a clean beam of 5 MeV neutrons, resulting from an $\alpha + \text{Be}$ reaction, was set up [Ruschke, 2010].

Further irradiation tests, with special emphasis on the efficiency and spatial resolution of ATLAS drift tubes for cosmics under neutron irradiation, are planned. $96 \times 500 \, \text{mm}^2$ large Micromegas with 384 strips could provide an external track reference, since it is expected, that their spatial resolution is not as strongly dependent on neutron background as no space

---

[5]http://bl.physik.uni-muenchen.de

Figure 1.6: Setup for neutron irradiation tests at the Munich tandem accelerator.

charge effects are present. This would as well be a realistic test for their radiation hardness (fig. 1.6).

The trigger scintillators or cherenkov detectors can be efficiently shielded, the Micromegas though will experience the high neutron flux. The cosmic spectrum should be hardened, using a lead absorber on top of the lower trigger to reduce the spatial resolution's increase due to multiple scattering.

To study the behavior of ATLAS MDTs in high rate gamma background with different geometries and different gas mixtures, tests at CERN's Gamma Irradiation Facility are performed.

Figure 1.7: Setup for gamma irradiation tests of MDTs in the Gamma Irradiation Facility at CERN [Engl, 2010].

The tracks of cosmic muons, determined in a track reference system, consisting of standard ATLAS MDTs, are interpolated into the chambers under investigation. Efficiency, occupancy and spatial resolution as a function of the gamma rate are studied. The replacement of the actual reference system by $256 \times 1000\,\text{mm}^2$ large Micromegas with 1024 strips, parallel to the wires in the MDTs, would have two advantages: First, the whole setup would be more compact, due to the smaller thickness of Micromegas, resulting in a considerably larger cosmic muon count rate. Second, due to the absence of space charge effects, Micromegas might not show a large increase of the spatial resolution under irradiation, resulting in a better track prediction.

The goal of this thesis was to evaluate in small prototypes, whether Micromegas are suitable for the described purposes. Furthermore, the underlying principles and the general behavior should be investigated and described.

Chapter 2

Theoretical Background

2.1 Interaction of Particles and Photons with Matter

Particles can interact with matter on the basis of the four forces, but since the cross sections for weak, strong or even gravitational interaction are extremely small compared to the electromagnetic ones, the electromagnetic force dominates the interaction of charged particles and photons with matter in gas detectors.

Five different interaction processes of charged particles can occur within gas detectors: Excitation, ionization, bremsstrahlung, Cherenkov radiation and transition radiation. The photo absorption ionization model, introduced by Allison and Cobb [1980], allows for calculating the mean energy loss of charged particles through excitation, ionization and Cherenkov radiation starting from the interaction of (virtual) photons with matter. It leads to the well known Bethe-Bloch formula

$$\left\langle \frac{\mathrm{d}E}{\mathrm{d}x} \right\rangle = -4\pi r_e^2 m_e c^2 \rho N_A \frac{Z z^2}{A \beta^2} \left(\ln \frac{2 m_e c^2 \beta^2 \gamma^2 T_{\max}}{I^2} - 2\beta^2 - \delta - 2\frac{C}{Z} \right) , \qquad (2.1)$$

r_e: classical electron radius, m_e: electron mass, ρ: target material's density, N_A: Avogadro constant, Z: atomic number and A: mass number of target material, z: charge number of incident particle, $\beta = v/c$: velocity of incident particle, $\gamma = 1/\sqrt{1-\beta^2}$: Lorentz factor, $T_{\max} = 2 m_e c^2 \beta^2 \gamma^2$: maximal kinetic energy transferable to an electron in an elastic collision, δ: density correction, C/Z: atomic structure correction

with the density and atomic structure corrections in the Sternheimer-Peierls and Barkas-Berger parametrization respectively [Sternheimer and Peierls, 1971; Barkas and Berger, 1964].

Cherenkov radiation is produced, when a particle's velocity within matter is greater than the velocity of light within that specific medium with refraction index n. Bluish radiation is emitted under an angle θ_{Ch} to the direction of flight

$$\cos \theta_{\mathrm{Ch}} = \frac{1}{\beta n} . \qquad (2.2)$$

Eq. (2.2) implies already the condition for occurrence of Cherenkov radiation: $\beta \geq 1/n$. A singly charged particle emits

$$\frac{\mathrm{d}N}{\mathrm{d}x} = 490 \sin^2 \theta_{\mathrm{Ch}} \ \mathrm{cm}^{-1} \qquad (2.3)$$

photons per centimeter in the visible range between $\lambda = 400\,\mathrm{nm}$ and $700\,\mathrm{nm}$, dependent on the angle θ_{Ch} [Grupen and Shwartz, 2008]. Since the refractive index of Argon gas at NTP[1] is $n-1 = 2.81 \cdot 10^{-4}$ [Kaye & Laby Online, 2005], the maximum Cherenkov angle is $\theta_{\mathrm{Ch}} = 1.36°$, corresponding to a maximum of 0.28 Photons/cm.

Bremsstrahlung is the emission of a hard photon by a particle in the proximity of a nucleus. Since the mean energy loss per unit length is proportional to the particle's energy E and its inverse mass squared $1/m^2$, bremsstrahlung is only relevant either for light particles such as electrons or at very high energies ($E \approx 1\,\mathrm{TeV}$ for muons). Furthermore, the radiation length X_0 for gases, which is the distance after which a particle has lost 63% of its initial energy, is much larger than the typical dimensions of gas detectors. Thus, bremsstrahlung is generally negligible for gas detectors, especially when detecting muons.

Transition radiation is produced by a fast particle, crossing layers with different refractive indices. The charged particle forms a variable dipole with its mirror charge and thus emits radiation. Although the photons emitted in this process can be detected in gas detectors (e.g. in the ATLAS transition radiation tracker), this effect can also be neglected in Micromegas.

Fig. 2.1 shows the stopping power for positive muons in copper. In the low momentum range, more or less phenomenological corrections are displayed. For a $\beta\gamma$ above ≈ 0.05, the energy loss according to Bethe-Bloch is relevant. As the interaction cross section has a global minimum for $\beta\gamma \approx 4$, particles within this momentum range are called minimum ionizing. The muons detected with the Micromegas in the course of this thesis are mostly within that range. After the so called relativistic rise, bremsstrahlung sets in at $\beta\gamma > 1000$.

Figure 2.1: Stopping power for positive muons in copper as a function of momentum $p = mc\beta\gamma$ [Groom et al., 2001].

It has been shown, that excitation and ionization are the relevant interaction processes for minimum ionizing muons in Micromegas. A charged particle itself ionizes the detector gas in the primary ionization. Some of the particles produced in this process have an energy high

---

[1]normal temperature and pressure, $\vartheta = 20°\mathrm{C}$ and $p = 1013\,\mathrm{mbar}$

enough to further ionize the gas in the secondary ionization. The total amount of charge created is the sum of both processes. The total amount of charge created by ionization of various gases by minimum ionizing particles is tabulated and will be used often in the following discussion (see tab. 2.1).

Gas	W_I [eV]	$dE/dx|_{min}$ [keV/cm]	N_T[1/cm]
Ar	25	2.53	106
CH_4	30	1.61	54
CO_2	34	3.35	100

Table 2.1: *Properties of rare and molecular gases at NTP [K. Nakamura et al. (Particle Data Group), 2010]. W_I [eV]: average energy deposited in gas per creation of an ion pair, $dE/dx|_{min}$ [keV/cm]: minimum ionizing particle's differential energy loss, N_T [1/cm]: total number of electron-ion pairs per centimeter.*

The total number of electron-ion pairs $n_{t,i}$ resulting from an energy deposition ΔE in a specific gas i, can be calculated by

$$n_{t,i} = \frac{\Delta E}{W_{I,i}} \ . \tag{2.4}$$

For a gas mixture, consisting of two gases i and j with a particle number fraction of a and $1-a$ respectively, a simple composition law [Sauli, 1977] gives for the total number of electron-ion pairs

$$n_t = n_{t,i} \cdot a + n_{t,j} \cdot (1 - a) = \frac{\Delta E}{W_{I,i}} \cdot a + \frac{\Delta E}{W_{I,j}} \cdot (1 - a) \ . \tag{2.5}$$

Because of the production of so called delta electrons in hard collisions with large energy transfer of the incident particle with the absorber's electrons [Landau, 1944], the energy loss of charged particles in thin absorbers is not Gaussian shaped, but has quite a long tail to higher losses. To distinguish several theoretical descriptions of energy loss in thin absorbers, a parameter

$$\kappa = \frac{\overline{\Delta E}}{T_{max}} \tag{2.6}$$

is introduced, where $\overline{\Delta E}$ is the mean energy loss in the detector and $T_{max} \approx 2m_e c^2 \beta^2 \gamma^2$ is the maximal transferable kinetic energy onto an absorber's electron [Leo, 1994]. Absorbers with $\kappa < 10$ are classified as thin, the Landau theory is applicable for $\kappa \lesssim 0.05$ [K. Nakamura et al. (Particle Data Group), 2010]. For minimum ionizing muons with $\beta\gamma \approx 4$, the mean energy loss in the 6 mm wide drift gap of Micromegas, running with Ar:CO_2 80:20 at NTP is $\overline{\Delta E} = 1.62$ keV. The maximal energy transfer on the other hand is $T_{max} \approx 2 \cdot 511$ keV $\cdot 16 = 16.4$ MeV. Thus $\kappa \approx 0.0001$.

It has been argued by Bichsel [2006], that the Landau distribution fails to describe the energy loss of minimum ionizing particles in very thin gas detectors such as the Micromegas. The measured distributions are much wider, due to an overestimation of the number of collisions of the incident particle with the absorber's atoms in the Landau theory (fig. 2.2).

The energy loss distribution of 3 GeV muons in the 6 mm drift gap of a Micromegas, filled with Ar:CO_2 80:20 at NTP, can be seen in fig. 2.3. The distribution has been calculated with GEANT4[2]. The most probable energy loss of $E_{mpv} = (1.0 \pm 0.1)$ keV is in agreement with the
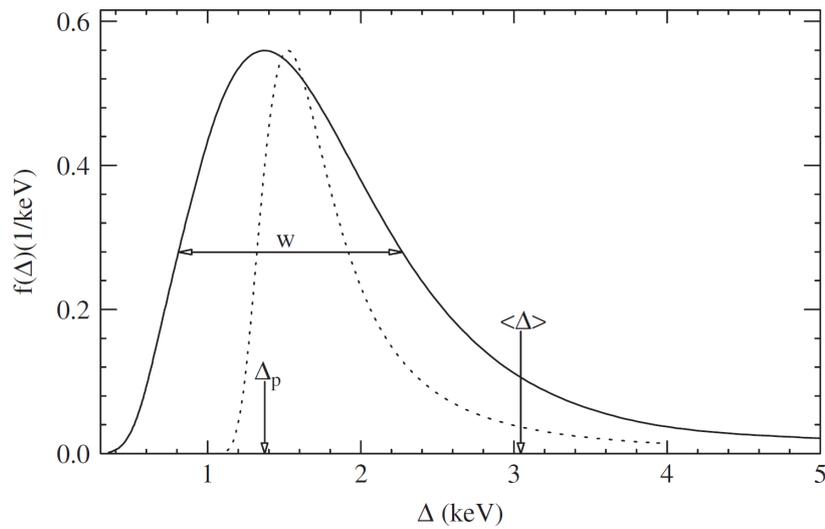
---

[2]http://geant4.cern.ch

Figure 2.2: *Energy loss $f(\Delta)$ for particles with $\beta\gamma = 3.6$ in 1.2 cm argon gas (solid line). The original Landau distribution is given by the dotted line. Taken from [Bichsel, 2006].*
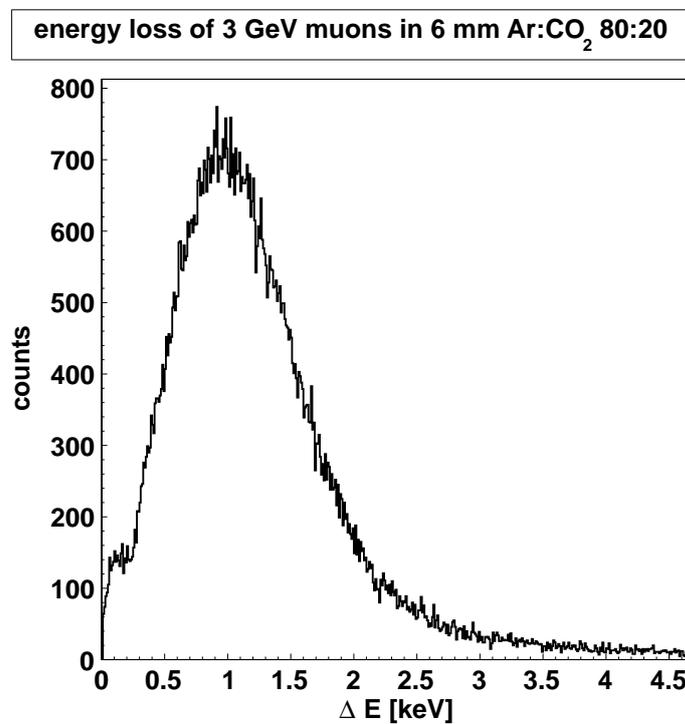

Figure 2.3: *Energy loss of 3 GeV muons in a 6 mm thick layer of $Ar:CO_2$ 80:20 at NTP, GEANT4 simulation.*

measured value, that will be discussed in sec. 6.2. The detector's intrinsic energy resolution, the energy distribution of cosmic muons and the angular distribution of cosmic muons will influence the measured energy distribution's shape. The most probable value though, should remain unchanged.

Photons interact, depending on their energy, essentially in three different ways with matter (fig. 2.4 shows as an example the total cross section in lead). The interaction cross section for low energetic photons is dominated by the photo effect i.e. the emission of a shell electron following the absorption of the photon by an atom. Since the total energy of the incident photon is usually deposited in the absorber, this effect is often the underlying process in energy calibration measurements in gas detectors.
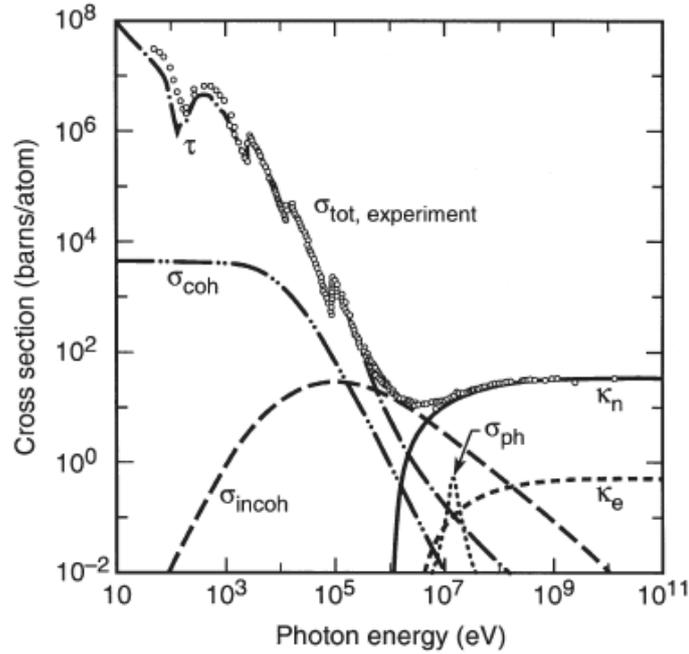

Figure 2.4: *Photon cross section in lead as a function of energy. Distinguished are the contribution of atomic photo effect τ, coherent scattering σ_{coh}, Compton scattering σ_{incoh}, pair production in the nuclear field κ_n and the electron field κ_e and finally the nuclear photo absorption σ_{ph} [Hubbell et al., 1980]. Taken from [Thomson et al., 2009].*

In the medium energy range between 10 keV and 4 MeV the primary interaction process is Compton scattering, which can be interpreted as the quasi-elastic collision of a photon with an electron in the absorber material. The amount of energy transfered is limited by the kinematics. Thereby the electrons carry kinetic energy up to the Compton edge, which can be seen in a detector's energy spectrum.

Production of an electron-positron pair in the nuclear field becomes the dominating process for photons with energy greater than twice the electron mass. The nucleus is necessary for simultaneous energy and momentum conservation.

A ^{55}Fe source is used in several measurements presented in this thesis. ^{55}Fe decays to ^{55}Mn by electron capture. The excited manganese emits photons at basically two different energies: $E_{K_\alpha} = 5.90$ keV in 25.4% and $E_{K_\beta} = 6.49$ keV in 2.99% of the decays. Since the cross section for photo effect dominates at these low energies, almost monoenergetic electrons with $E_e = E_{K_\alpha/K_\beta} - W_e$ are created. W_e is the electron's binding energy. Thus, a ^{55}Fe source can be seen as a charge deposition normal and allows for calibrating the detector.

A third line, the so called K_α escape peak is also visible in the energy spectrum. It corresponds

to an energy of $E_{K_\alpha,\text{esc}} \approx 2.94\,\text{keV}$. When the incident X-ray photon ionizes an argon atom by displacing an electron from the K shell, the excited argon ion emits a photon with $E_{KL} = 2.96\,\text{keV}$ [Deslattes et al., 2005], resulting from a transition of an L electron to the K shell. If this photon leaves the detector without being detected, only the residual energy of the original K electron is visible, forming the escape peak.

2.2 Drift of Electrons and Ions in Gases

An electric field makes ions and electrons move, depending on their charge, in or against field direction. Frequent collisions with gas atoms arranges for the charges to move with a constant drift velocity. For a wide range of reduced electric fields E/p, the drift velocity of ions is proportional to the field

$$v_{\text{d}}^+ = \mu^+ E \frac{p_0}{p} \ , \tag{2.7}$$

where the proportionality constant μ^+ is called mobility, $p_0 = 1013\,\text{mbar}$ and p is the actual gas pressure [Kleinknecht, 1992].

Figure 2.5: Drift velocity of Neon, Helium and Argon Ions in their respective gas [Hornbeck, 1951].

The drift velocity of several ions in their respective gases is shown in fig. 2.5 as a function of the reduced field E/p. Tab. 2.2 summarizes several ion mobilities.

Gas	Ion	mobility μ^+ in cm^2/Vs	source
Ar	Ar^+	1.54	[K. Nakamura et al. (Particle Data Group), 2010; MacDaniel and Mason, 1973]
Ar	Ar^+	1.7	[Sauli, 1977]
Ar/CO_2	CO_2^+	1.72	[K. Nakamura et al. (Particle Data Group), 2010]
CO_2	CO_2^+	1.09	[K. Nakamura et al. (Particle Data Group), 2010]

Table 2.2: Ion mobilities for several ions in different gases. The literature values vary.

Electron drift in electric fields is a more complex business, since the electrons can gain quite a large energy in the field; their de Broglie wavelength is then on the order of the atomic diam-

eter and quantum mechanical interference effects (Ramsauer effect) cause a strong variation in the cross section as a function of electron energy. A complex interplay between the cross section for rotational or vibrational excitation and elastic scattering cause a strong variation of the electron drift velocity in gas mixtures. On the other hand, CO_2 in an Ar:CO_2 mixture for example acts as a quencher since it absorbs UV-photons from excitation of gas atoms and thus prevents the propagation of discharges in the detector. Gas mixtures based on argon and carbon dioxide are used in Micromegas, since they are more or less inert and inflammable.
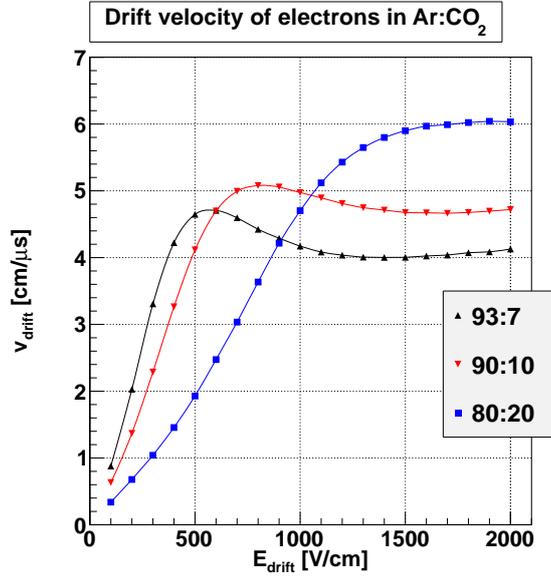

Figure 2.6: Drift velocity of electrons in several mixtures of Ar:CO_2 at NTP, calculated with MAGBOLTZ. The pressure, temperature and electric field range corresponds to values, used in the course of this thesis.

To calculate theoretical electron drift velocities, Stephen Biagi's program MAGBOLTZ[3] is applied. The drift velocity of electrons in the used gases is displayed in fig. 2.6.

2.3 Charge Multiplication in Gas Detectors

As the amount of charge created by minimum ionizing particles in gases is rather small (tab. 2.1), a process of charge multiplication is necessary to achieve accessible signals. In high electric fields electrons can gain a sufficient amount of kinetic energy to further ionize the gas atoms/molecules in collisions. This process is called avalanche multiplication or gas amplification. The amount of charge in the avalanche doubles after each mean free path λ of the electrons, thus half of the total charge is created within the last mean free path. Assuming an uniform electric field, the number of electrons $\mathrm{d}n$ created in an avalanche is proportional to the path $\mathrm{d}x$, covered by n primary electrons, and is given by

$$\mathrm{d}n = \alpha n \mathrm{d}x \ , \tag{2.8}$$

where the proportionality constant α is called first Townsend coefficient [Sauli, 1977]. Its inverse is the electron's mean free path $\lambda = \alpha^{-1}$. Integration yields

$$n(x) = n_0 e^{\alpha x} \ . \tag{2.9}$$

---

[3]http://consult.cern.ch/writeup/magboltz/

The gas specific first Townsend coefficient is a function of the electric field and the gas pressure and temperature. For the discussion in this thesis, values calculated by MAGBOLTZ are deployed and can be seen in fig. 2.7.
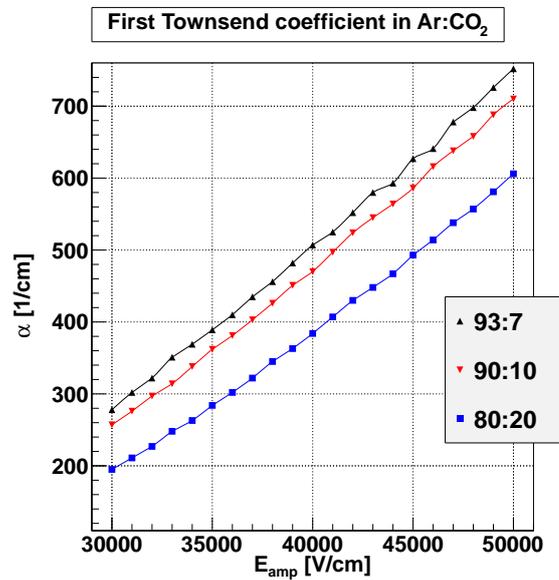

Figure 2.7: First Townsend coefficient α as a function of a uniform electric field E_{amp} for three different mixtures of argon and carbon dioxide at $\vartheta = 20°\,C$ and $p = 1012\,mbar$. The gas amplification in Micromegas will be discussed in sec. 6.3.

Chapter 3

Micromegas Setup

3.1 Introduction

The detectors under study are so called bulk Micromegas, produced by the CERN PCB workshop[1]. Details about the manufacturing process can be found in [Giomataris et al., 2006] and will be briefly summarized below. The term bulk refers to the uncomplicated production process.

3.2 Internal Structure

Figure 3.1: Schematic view of the Micromegas' internal structure. The distance mesh-anode of 128 μm is not drawn to scale. Nylon rings are used to adjust the 6-7 mm width of the gap between cathode and mesh.

A 1.6 mm or 1.7 mm thick epoxy base plate carries 360 anode strips with 100 mm length. They are 150 μm wide and spaced by 100 μm. This adds up to an active area of $100 \times 90 \, \text{mm}^2$. For shielding, the PCB's back side is covered with a mass plane. High voltage is passed into the gas volume by strip lines, that are several millimeters wide. All conducting paths are made of copper and plated with nickel/gold.

The woven stainless steel mesh, formed by 18 μm thick wires with a pitch of 45 μm, is laminated together with a photo resistive film and the base plate at high temperature. The film is photolithographically etched to produce a few centimeters wide supportive frame and pillars of 300 μm diameter. Since the pillars are spaced at intervals of 2.5 mm, around $100 \, \text{mm}^2$ of the active area is covered, corresponding to 1.1%. The electric amplification field is expected

---

[1]CERN Department EN-ICE-DEM, responsible Serge Ferry; PCB: printed circuit board

to be deformed by the pillars in an area considerably larger than this. As the pillars are placed periodically, every tenth readout strip is covered by 40 pillars. Thus in the worst case 13.2 % of those strips' area is covered by pillars.

Four nylon screws support the drift cathode, made of the same stainless steel mesh and glued to a robust glass-reinforced plastic frame of 2 mm thickness. Adjustment of the distance between mesh and cathode is possible by adding machined nylon or epoxy rings (some of these informations are taken from [Burnens, 2009]).

The amplification gap formed by the anode strips and the mesh has a height of 128 µm. The drift gap's width corresponds to the distance between mesh and cathode. It is, depending on the detector, 6 to 7 mm wide, enabling the production of an at least sufficient amount of charge from ionization. For later versions, smaller drift gaps are foreseen.

3.3   High Voltage Supply

The mesh is directly soldered to the strip line providing its high voltage (HV). The cathode is connected via a short cable and a screw contact to the conductive path.
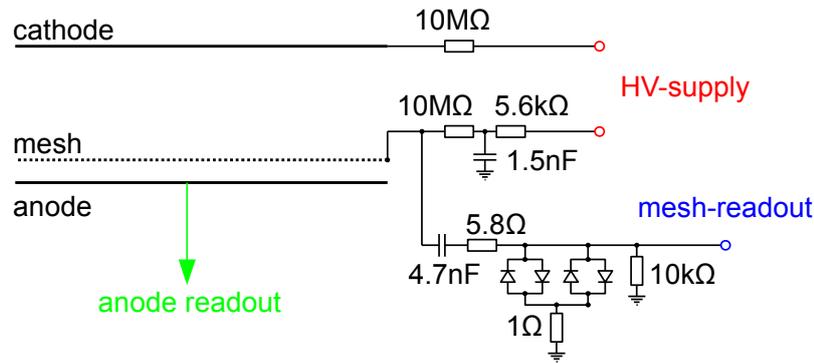

Figure 3.2: Schematic of high voltage provision. Currents flowing between cathode/mesh and HV-supply are limited by 10 MΩ resistors, the mesh high voltage is additionally filtered by a passive low pass. The ions' signal on the mesh can be read out with a charge sensitive preamplifier and could be used for triggering or timing purposes.

Both components are connected via a 10 MΩ resistor to SHV-connectors to limit the current flowing during discharges and to increase the recharge time to a value, where especially the mesh is not able to draw further current out of the source during a discharge. Estimating the mesh's capacitance to ground to be around 550 pF (see sec. 8.3) one gets a recharge time of $\tau = RC = 5.5$ ms.

Assuming a spark frequency of $1\,\mathrm{min}^{-1}$, the efficiency's reduction due to the mesh recharge time is 1% for an event rate of 11 kHz. This is far beyond any cosmic rate, measured with the Micromegas.

Since the high voltage provided by the deployed HV-supplies[2] is not entirely flat but has a high-frequency ripple of some mV and a 50 Hz ripple of around $3\,\mathrm{mV_{P\text{-}P}}$ (according to the HV supply's data sheet [Iseg Spezialelektronik, 2009] the absolute maximum ripple is $5\,\mathrm{mV_{P\text{-}P}}$), it has to be filtered to reduce the noise seen by a preamplifier on the anode or on the mesh. Due to the small distance of the mesh from the anode strips, the overwhelming part of this particular noise on the anode is caused by the high voltage on the mesh. This

---

[2]iseg SHQ 224M

was experimentally confirmed. No improvement is visible when disabling or filtering the high voltage on the cathode. Thus a simple passive low pass filter consisting of a $1.5\,\mathrm{nF}$ capacitor and a $5.6\,\mathrm{k\Omega}$ resistor is installed on the supply-side of the mesh. Since the output voltage of a low pass is (see [Demtröder, 2004, p. 155 ff.])

$$U_{\mathrm{out}} = \frac{1/(i\omega C)}{R + 1/(i\omega C)} U_{\mathrm{in}} \;, \tag{3.1}$$

the characteristic cutoff frequency[3] is $f_{\mathrm{cut}} = 18.9\,\mathrm{kHz}$, sufficient to effectively eliminate the dominant $50\,\mathrm{MHz}$ high-frequency noise. It is large enough to not influence the recharge time of the mesh after a discharge.

It should also be noted, that it was advantageous to insulate the ground contact of both SHV connectors against detector ground, defined by the ground of the electronic readout to avoid ground loops.

3.4 High Voltage Control

The high voltage is remotely controlled and monitored via a RS232 interface. The iseg SHQ power supplies know three basic functions: Read (get actual voltage, current, ramp speed, status ...), Write (set voltage, ramp speed, ...) and Switch (activate voltage change). A C++ program called `isegcontrol.C` is written to control and monitor the high voltage. This macro is executed within the CERN analysis framework ROOT[4]. Communication via the serial port is based on the MARaBOU class TMrbSerialComm, providing functions to open a serial port, set the device parameter and communicate with the iseg SHQ using the character exchange routines `ReadData()` and `WriteData()`.

All communication is ASCII character based, the commands can be found in [Iseg Spezialelektronik, 2009]. To simplify the communication, SHQ specific high level routines are written, taking the serial port address and the high voltage port number as input. Together with a short description they can be found in table A.1 in the appendix. Before execution of `isegcontrol.C` the appropriate libraries have to be loaded by executing the ROOT macro `isegload.C`. The programs are briefly discussed in the appendix A.

Apart from ramping up the high voltage to the desired values and monitoring voltage and drawn current, sparks from the mesh onto the anode strips can be detected by registering the violation of the hardware current limit, which is set to $\approx 6\,\mathrm{\mu A}$ or $\approx 0.6\,\mathrm{\mu A}$, depending on the HV supply's version. A current exceeding is saved to file together with date and time such that a subsequent analysis is possible.

Since each HV supply needs its own RS232 port, USB to RS232 converters are used to control up to 7 devices from a single computer.

3.5 Gas Mixture and Pressure Control System

Control of pressure and gas composition in the detector is achieved by the system shown schematically in fig. 3.3.

The gas flow into the self made gas mixer is controlled by Brooks Thermal Mass Flow Con-

---

[3]$U_{\mathrm{out}} = U_{\mathrm{in}}/\sqrt{2}$ at f_{cut}.
[4]http://root.cern.ch

trollers[5]. The mixed gas is then passed to the detector. Several detectors are connected in a daisy chained manner. An electronically regulated valve[6] in combination with a pressure meter[7] and a PI-controller, stabilizes the pressure in the system at the preset value by controlling the gas flow at the outlet. The whole system is mounted on an aluminum plate. It is about 10 inches high and fits into a 19 inch rack.

Figure 3.3: Schematic of the gas mixture and pressure control system.

A gas flow of around 1 ln/h is used for most measurements presented in this thesis. To prevent oxygen from entering the detector and to reduce the spark probability, the pressure was maintained at around 1013 mbar, which corresponds to slight overpressure in Munich.

---

[5]two Brooks Smart Mass Flow Controller 5850S [Brooks Instrument, 2008a], two SLA58050 [Brooks Instrument, 2008b]

[6]Flow Control Valve Type 248A, MKS Instruments [MKS Instruments, 1997a]

[7]Absolute High Accuracy Pressure Transducer Type 690A, MKS Instruments [MKS Instruments, 1997b]

Chapter 4

Single Preamplifier Readout

4.1 Introduction

General behavior of the detector can be investigated by recording complete signal cycles from a charge sensitive preamplifier with a fast flash analog-to-digital converter (FADC). The setup is displayed in fig. 4.1. Two trigger scintillators with photomultipliers enclose the Micromegas. Unfortunately their sensitive area of $130 \times 90\,\mathrm{mm}^2$ is slightly bigger than the Micromegas'. When determining parameters like the efficiency, this has to be taken into account.

4.2 Setup

The setup is shown schematically in fig. 4.1. The Micromegas' anode is read out by a Canberra 2004 charge sensitive preamplifier [Canberra Industries, Inc., 2007], originally designed to comply with signals of silicon detectors. Since the signals in Micromegas do not show the long ion tail, typical in wire detectors, it is also suited for this application. The preamplifier signal is digitized by the VME[1] CAEN 12 bit 1 GHz flash ADC V1729 [CAEN S.p.A., 2010]. It has an input range of $\pm 0.5\,\mathrm{V}$ and provides 2520 usable sample points. Typical signals show a rise time of 150 ns and can therefore be comfortably recorded in the 2520 ns sampling time. The continuous sampling of the analog signal stops a programmable number of clock cycles after a trigger. Since this number can be smaller than 2520, it is possible to record the full signal rise including the behavior of the preamplifier's baseline before the signal.

Triggers are provided by a coincident signal (20 ns coincidence time) of both scintillators. Splitting the preamplifier's signal between the FADC and an ORTEC 474 timing filter amplifier (TFA) [ORTEC, 2008] allows for enforcing a threefold coincidence between the two triggering scintillators and the Micromegas detector: The discriminated TFA's signal is elongated in a CAEN timer N39B [CAEN S.p.A., 1991] to 300 ns to avoid double triggers. To improve the timing resolution by letting the scintillators define the trigger time, the scintillators' coincident trigger is delayed and elongated to 200 ns.

As the VME flash ADC occasionally crashes upon receiving a second trigger when still being busy with handling the first one, the short NIM[2] trigger pulse coming out of the second coincidence unit is fed into a third CAEN timer. This timer then outputs an infinitely long

---

[1]Versa Module Eurocard-bus.
[2]Nuclear Instrumentation Standard. Logic levels: Logic 0 = 0.0 V, logic 1 = −0.6 V - −1.6 V, both into a 50 Ω load.

Figure 4.1: Trigger and signal circuit used in the flash ADC readout. The light gray shaded modules are NIM modules.

NIM pulse until it is reset by a pulse from a CAEN V977 input-output register in the VME crate [CAEN S.p.A., 2004]. This reset pulse is emitted, CPU controlled, upon completion of the readout cycle. Since the FADC is triggered by the signal's falling edge, further trigger signals during the readout cycle are effectively suppressed.

Communication between the VME modules and the data acquisition computer is handled by a Struck SIS3150USB VME to USB interface[3]. The number of twofold and threefold coincidences is counted by two CAEN N1145 counters [CAEN S.p.a., 2003].

For measurements with a ^{55}Fe-source, the scintillators' trigger circuit can be bypassed. The trigger is then directly derived from the Micromegas' signal (denoted with "alternative trigger" in fig. 4.1).

The three different trigger configurations will be discussed in sec. 6.2.

4.3   Protective Circuit

For signal studies with the FADC readout, all strips or a subsample of strips were shorted and read out by a single charge sensitive preamplifier. When reading out all 360 strips, five shorted ERNI[4] 80-pin connectors are necessary (each covering 72 strips).

Measurements performed by Jeanneau et al. [2000] with similar Micromegas, show that in sparks, induced by heavily ionizing particles or cosmic showers, the mesh can discharge completely onto the anode strips. For a mesh capacity to ground of 550 pF (see sec. 8.3) and a mesh high voltage around -550 V, the amount of charge flowing onto the anode in a discharge is as big as 0.3 μC. Assuming a gas gain of 5000, the amount of charge created in typical MIP signals is with 50 fC more than 6 orders of magnitude smaller. Obviously the readout electronics needs to be protected against discharge currents.
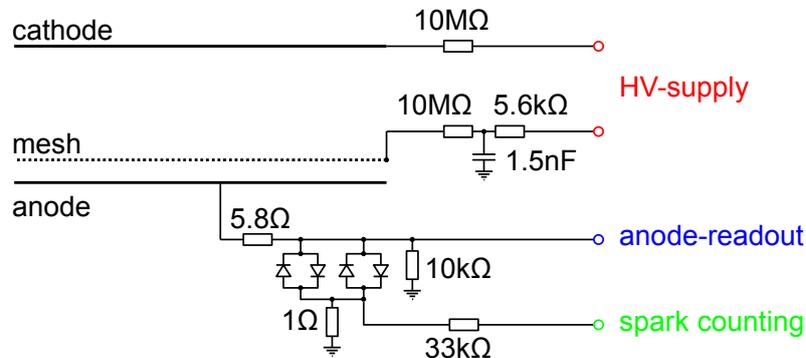

Figure 4.2: Schematic of the readout and protective circuit used with a single preamplifier.

The protective circuit used is shown schematically in fig. 4.2. A 5.8 Ω resistor protects the two BAV99 protection diodes against destructive current; furthermore it is used to match the strip-impedance to the readout. The BAV99, low capacity, fast switching Si-diodes are commonly used in detector protective circuits e.g. in the muon monitored drift tubes of the ATLAS experiment. Both diodes are grounded using a 1 Ω resistor. The voltage across this resistor is attenuated with a 33 kΩ resistor and can be measured. Thus, it is possible to count sparks.

The anode is grounded via a 10 kΩ resistor, which is not affecting the actual pulse height

---

[3]Struck Innovative Systems
[4]ERNI electronics GmbH, http://www.erni.com

but allows the charge to flow off the anode in about 10 µs and, more important, significantly reduces noise on the anode.

4.4   Efficiency Simulation

The experimental efficiency is calculated by comparing the counting rate of coincidences of the scintillators to the counting rate of actual triggers, given to the FADC. These triggers are created, when the two scintillators' coincidence signal coincides with a Micromegas signal. As the two scintillators used for coincident triggering of the Micromegas cover an area slightly bigger than the sensitive area of the detector, a Monte Carlo simulation is used to determine the actual efficiency.

Fig. 4.3 shows the schematic setup and the principle of the simulation. The three detectors are represented by rectangles. For each point on a fine grid on the lower scintillator, a large number of detected muons is simulated. I assume that the two angles θ and ϕ, defining the muons' directions, are distributed like $f(\theta) = \cos^2\theta$ and $g(\varphi) = 1/2\pi$.
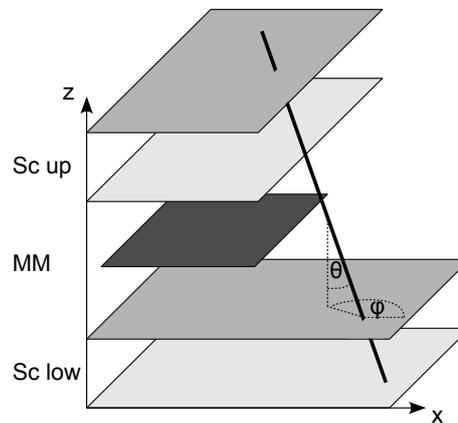

Figure 4.3: Schematic setup used in the simulation.

After conversion to cartesian coordinates via

$$
\begin{aligned}
direc[0] &= \cos(\varphi)\sin(\theta) & (4.1)\\
direc[1] &= \sin(\phi)\sin(\theta) & (4.2)\\
direc[2] &= \cos(\theta)\ , & (4.3)
\end{aligned}
$$

the muon's direction vector $direc$ is normalized with respect to its z-coordinate:

$$
check[i] = direc[i]/direc[2] \qquad (4.4)
$$

i runs from 0 to 2, $check$ is the normalized direction vector. To decide whether or not the muon hit the upper scintillator, $check$ is scaled up so that the endpoint of the direction vector lies in one of the upper scintillator's planes (fig. 4.4).

By checking whether the endpoint lies within the respective rectangle, symbolizing the upper or the lower side of the scintillator, it can be decided, whether the muon also hit the upper scintillator. A hit is counted ("muon hit upper scintillator") and by using the same method it is checked whether the same muon hit the Micromegas (counted as "muon hit micromegas"), too. By comparing the two numbers "muon hit upper scintillator" and "muon hit
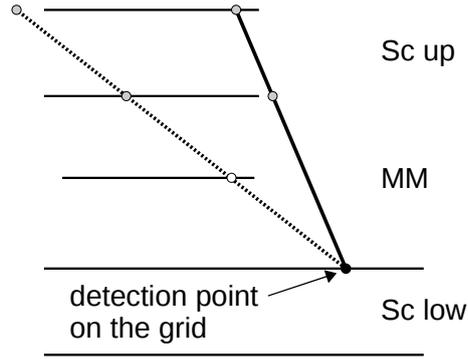
Figure 4.4: Two dimensional schematic view of the simulation method. Starting from the detection point (black), the direction vector's endpoint in both planes of the upper scintillator is calculated (upper and lower side, endpoint in gray).

micromegas" a ratio can be calculated which gives the correction factor f_{geom} for determining the real efficiency.

For the setup with one Micromegas one gets a mean correction factor of 0.881 ± 0.005 by variation of the simulation parameters.

If one assumes a reasonable value for the lower scintillator's muon count rate, it is also possible to estimate the trigger rate of the whole system.

Since this simulation is the starting point for an improved simulation of muon tracks in a three Micromegas detector system, its source code can be found in the appendix B.

4.5 Signal Analysis

The pulses recorded with the flash ADC are analyzed by fitting an inverse Fermi function

$$f(x) = \frac{p0}{e^{\frac{p1-x}{p2}}} + p3 \tag{4.5}$$

to the rising edge (Fig. 4.5). Furthermore, two constant functions are fit to regions before and after the rising edge.

The Fermi fit function depends on four parameters. $p0$ is the amplitude, giving the pulse height of the event. The position of the inflection point $p1$ allows for calculating the event time, which should always be around the same value since, for cosmics, the trigger is provided by fast scintillators. For self-triggering (e.g. for X-rays) the timing should be more or less independent of the individual event, too.

The width or slope of a Fermi function is determined by the third parameter $p2$. By multiplying $p2$ by a correction factor of 4.4, one can calculate the 10% - 90% risetime. And the fourth parameter $p3$ finally gives the baseline value of the registered signal.

All parameters are histogrammed and can thus be analyzed. For coincident triggering by the Micromegas itself and one or more additional scintillators, all recorded events should be "real" events. This does not have to be the case for runs, where the detector triggers itself. Noise and discharges are also registered since one does not want to lose small "real" events by choosing an unreasonable high discriminator threshold.

To effectively distinguish between events and noise, an additional method is used: for a period
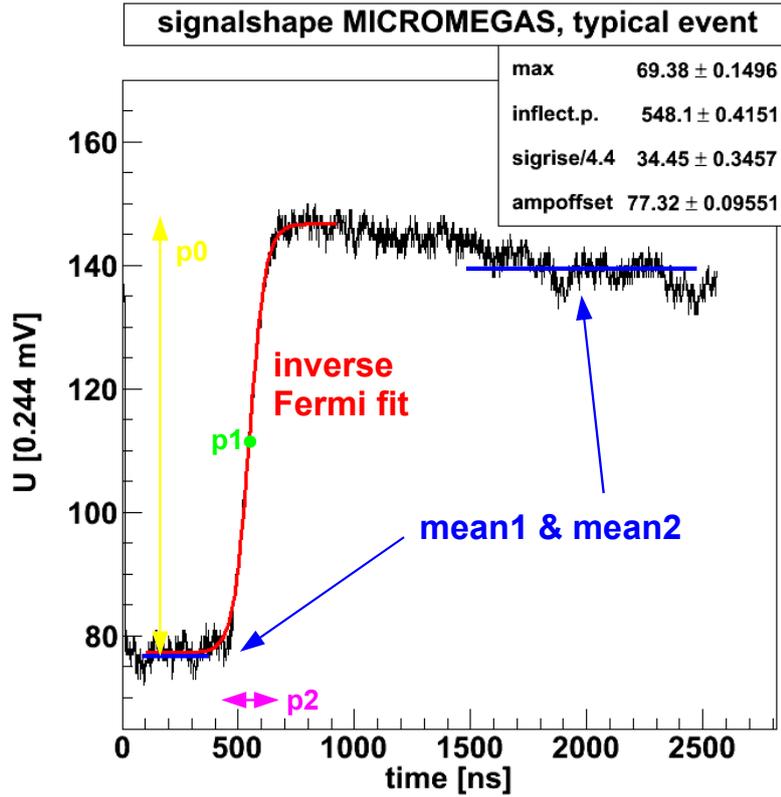
Figure 4.5: Typical charge signal. An inverse Fermifunction is fit to the rising edge (red). For discharge and noise software discrimination an additional method is used: The mean value and the standard deviation of the signal amplitude in two regions is calculated (blue lines). If the difference of the two means is smaller than three times the standard deviation, the event is ignored in the following analysis. The high data point close to the origin are an artifact of the conversion process and have no physical meaning.

of 300 ns clearly before and 1000 ns after the rising edge (blue lines in fig. 4.5), the average values of the data points $mean1$ and $mean2$ and the standard deviations σ_1 and σ_2 are calculated. The fit with the Fermifunction and the subsequent analysis is only performed for signals, where the difference $mean2 - mean1$ is bigger than $3\sigma_{max}$ where $\sigma_{max} = \max(\sigma_1, \sigma_2)$. Another possibility would have been to cut on $mean2 - mean1 > \sqrt{\sigma_1^2 + \sigma_2^2}$. It has been observed though, that the simple method works as desired. Typically around 10%-20% of the registered signals are noise or discharges and thus eliminated by this procedure.

Chapter 5

Gassiplex Based Strip Readout

5.1   Introduction

The electronic strip readout based on preprocessing frontend modules using charge integrating Gassiplex chips is described in the following. The 16 channels Gassiplex chips incorporate an amplification stage, a track & hold circuit and a 16 channel multiplexer [Beusch et al., 1994]. The employed frontend boards were originally designed for the ring imaging cherenkov detector (RICH) in the HADES experiment [Zeitelhack et al., 1999]. Within this RICH, the Cherenkov photons created by relativistic leptons in a gaseous C_4F_{10}-radiator are reflected via a VUV-mirror onto a 500 nm thin CsI-layer. Electrons resulting from photon conversion within this layer are amplified and detected in an asymmetric thin gap multi-wire proportional chamber with cathode pad readout. Since the cathode pads are on ground potential they are directly coupled to the frontend modules, without the need of a coupling capacitor. Induction signals of positive polarity are expected. The frontend modules were thus designed for positive signals and discharges.

A detailed description of the complete electronic readout system can be found in [Böhmer, 1999], an introduction to the relevant part of a stand alone readout system will be given in the next section.

5.2   Components of the Gassiplex Stand Alone Readout System

Frontend modules provide analog charge to voltage conversion, signal preamplification and shaping, digitization by a fast-analog-to-digital converter, digital threshold comparison, multi event buffering by temporary storage of up to 15 full events (15×64 ADC values) and handling of the data transfer to the readout controller (fig. 5.1). They are, in general, capable of asynchronous data acquisition and data transfer. Several frontend modules are operated in a daisy-chained mode and connected via a bus card to the readout controller. Before enabling data acquisition, the readout controller (RC) configures the frontend modules (FE) by writing e.g. threshold and mapping values. During the run it also transmits the trigger received by the detector trigger unit (DTU) to the FEs and controls the readout of the data temporarily stored on the FEs. Busy handling is ultimately done by the DTU which also accepts an external trigger[1]. The frontend modules are not capable of creating an internal trigger nor is it possible to get access to the analog preamplified signal.

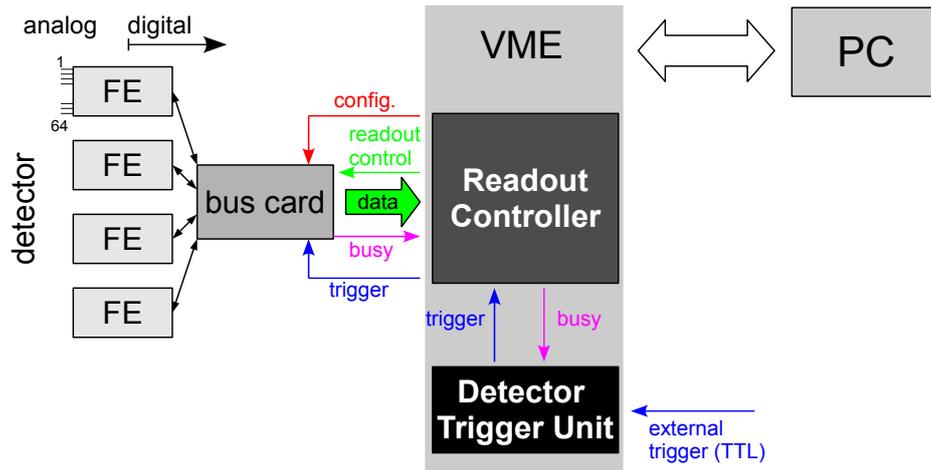---
[1]TTL, active high, rising edge.

Figure 5.1: Main components of the stand alone readout system are: The frontend modules with four Gassiplex chips each, corresponding to 64 channels per frontend, a bus card, connecting four frontend boards, the readout controller and the detector trigger unit. Bus cards for up to 8 FEs are possible. The most important commands exchanged between the different modules are shown schematically.
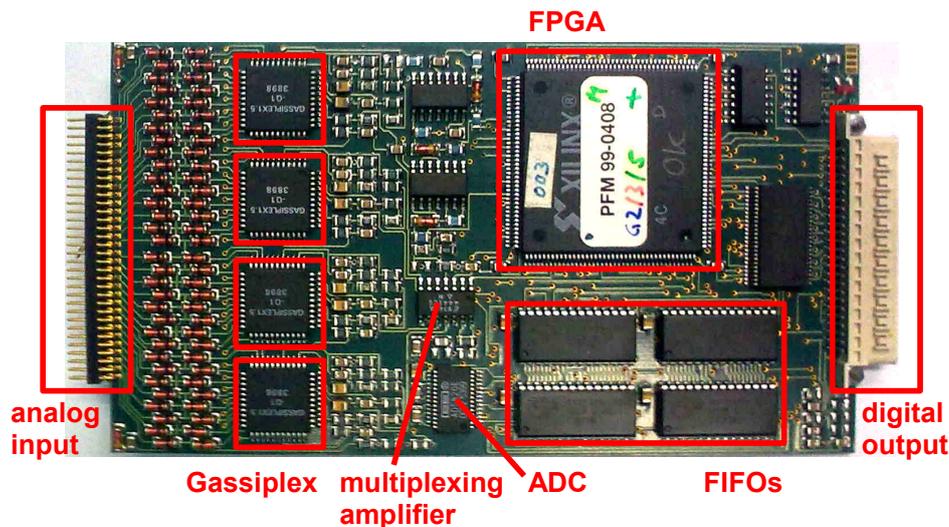
5.2.1   Frontend Modules

Figure 5.2: Preprocessing frontend module. The relevant parts are marked. Its dimensions are $120 \times 65\ mm^2$.

A single HADES preprocessing frontend module (figs. 5.2 and 5.3) covers 64 readout strips. It carries four Gassiplex chips with 16 channels each, containing a charge sensitive preamplifier, a shaper and a track & hold circuit for each channel. The shaper's output is a nearly Gaussian shaped signal with a rise time of 550 ns acting as a delay since no circular buffer is implemented. The 550 ns delay between a particle's passage and the trigger signal is sufficient for several logical operations with other components of the readout system. To avoid noise in the analog signal, the frontend's digital part is more or less silent when waiting for a trigger. For stability reasons the frontend's 33 MHz oscillator is always running. Upon an external trigger, the Gassiplex chips freeze the actual analog value in their track & hold circuit (T/H_TTL in fig. 5.4). If the trigger delay is set to 550 ns, according to the shaper's
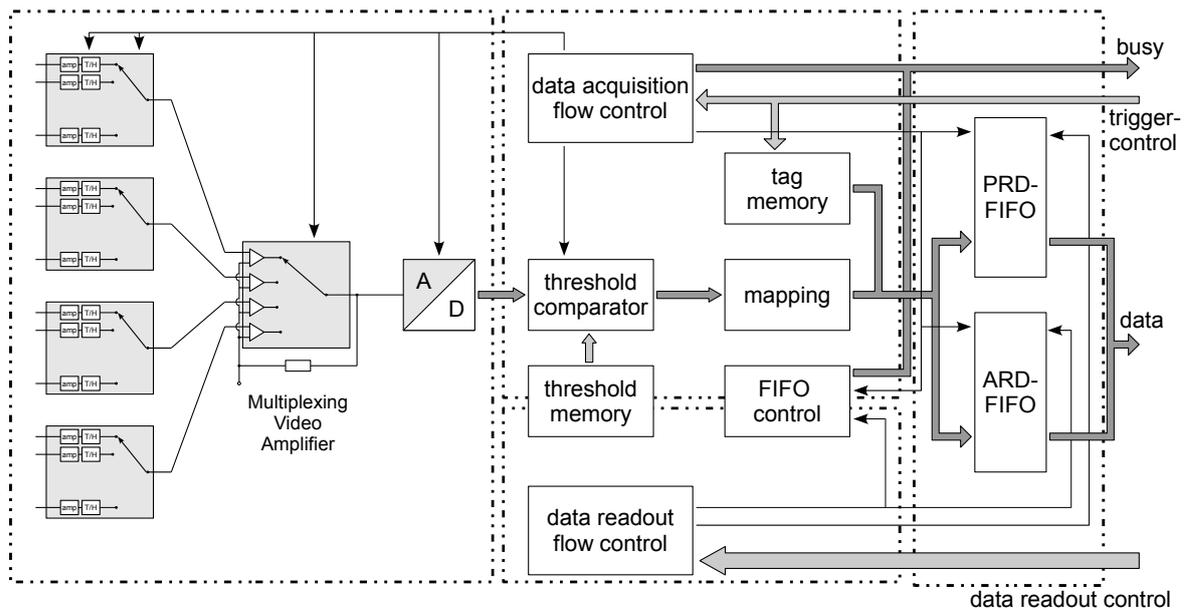
Figure 5.3: Block diagram of a preprocessing frontend module. Four main blocks are distinguishable: The analog signal processing is performed in the left block, the upper block incorporates the logic necessary for data acquisition, the lower one the logic for data readout and the very right block consists of two FIFO memory banks, used for storing data from up to 15 full events (15×64 ADC values). PRD and ARD stand for pattern and analog readout. Taken from [Böhmer, 1999].

rise time, the maximum analog value is held. It is in principle possible to scan the shaper's output by varying the trigger delay.

A fast video multiplexing amplifier EL4441CS [Elantec, 1994] multiplexes the held analog values of four Gassiplex chips to the 20 MHz 10bit sampling ADC ADS820 [Burr-Brown Corporation, 2005]. The digitization of the analog values is followed by the operations described in fig. 5.3. After a digital threshold comparison all data from channels above the channel specific threshold is saved to FIFO banks. Since it is of importance when adapting the frontend module for Micromegas style negative signals, the course of data acquisition in the analog section will be described in detail in sec. 5.3.

5.2.2 Readout Controller

The VME based readout controller enables the communication with the VME CPU and thus also with the PC. It handles the configuration of frontend modules, just as well as data readout and event tagging and mapping. Diagnostic inspection of errors in the readout chain can be performed remotely when no direct access to the frontend modules is possible.

Furthermore, the readout controller provides the interface to the detector trigger unit, transmitting the trigger signal to the frontends when neither the readout controller nor the frontends are busy. The RC's dead time is dominated by the data transfer to the PC and could be considerably reduced by using the digital baseline discrimination on the frontend modules.

5.2.3 Detector Trigger Unit

Since the whole readout system has been designed to operate in a multi-level-trigger system, a second VME unit, called the detector trigger unit was designed to handle the memory

management and event merging with data from other detector components. In a stand alone
system, it basically accepts the external trigger and takes care of busy signals emitted by the
frontends or the readout controller.

5.3   Adaptation of the Frontend Modules

Considering that the frontend modules were originally designed to handle positive signals
and also positive discharges, a general hardware adaptation to fit the Micromegas' negative
electron signals was necessary. After testing a first adaptation of the modules to negative
signals, used to read out the scintillating fiber detector in the HERMES recoil detector [Hoek
et al., 2007], an additional change was performed, as the modules did not perform properly.

5.3.1   Analog Signal Processing on the Frontend Modules

Fig. 5.4 shows the processing of analog signals on the frontend module. Each Gassiplex input
channel is protected by a diode against positive spikes. The diodes end on a common signal
line, which is pulled up to 3.3 V to bring the diodes into a highly non conducting regime, since
the input channels themselves are on negative potential ≤ -1.6 V. Each Gassiplex channel
exhibits a charge sensitive preamplifier and a shaper. The optional deconvolution filter is
switched off. Upon a trigger signal T/H_TTL[2], which is high during the whole hold cycle,
the internal track & hold circuit freezes the shaper's signal. Electronic noise, caused by the
digital part of the electronic, can thus not alter the recorded signal anymore.

With the first pulse of CLK_TTL, which is used to multiplex the 16 channels of each Gassi-
plex, the held analog value of channel 0 appears at the output of all Gassiplex chips. The
multiplexing video amplifier incorporates a non-inverting voltage amplifier for every input
channel and a multiplexing unit, multiplexing the output of the four voltage amplifiers. It
transmits the actual value of each Gassiplex to the analog-to-digital converter. The inverting
inputs of the four operational amplifiers are tied together, resulting in a common feedback
network. The four signals of the four Gassiplex chips are consecutively sampled once by the
ADC, running at around 7.5 MHz.

With the second pulse of CLK_TTL, the Gassiplexes give the analog value of channel 1 to the
multiplexer and so on. Since the amplifier stages in the Gassiplex chips are non-inverting,
negative charge signals on the frontend inputs correspond to negative voltage signals at the
ADC's input. To cope with the ADC's input range of +0.25 V to +4.25 V, some adaptation
is necessary.

The baseline voltage of the Gassiplex chips is, although slightly differing for different channels,
around +150 mV. Typical Micromegas signals cause a pulse height of −500 mV to −1.0 V.
Only one option is imaginable to match these signals to the ADC's input without completely
redesigning the frontend boards: to raise the multiplexing amplifiers output baseline to values
close to the upper limit of the ADC's input range.

An inversion of the multiplexing amplifier's signals by swapping its inverting and non-
inverting inputs, is unfortunately impeded, since the multiplexing amplifier features an in-
ternal common feedback for the inverting inputs. Thus the four inverting inputs are not
individually accessible. Therefore, the voltage on the common inverting input of the mul-
tiplexing amplifier is pulled down to a lower i.e. more negative value $U_{\mathrm{in}-}$. This raises its
output's baseline to a more positive value. By this means a small but positive voltage on
the multiplexing amplifier's input would result in a large positive output, whereas a negative

---

[2]Transistor-transistor logic: Logic 0 = 0.0 V - 0.8 V, logic 1 = 2.2 V - 5.0 V.

input voltage, which should still be larger than U_{in-}, would cause a smaller positive output voltage.
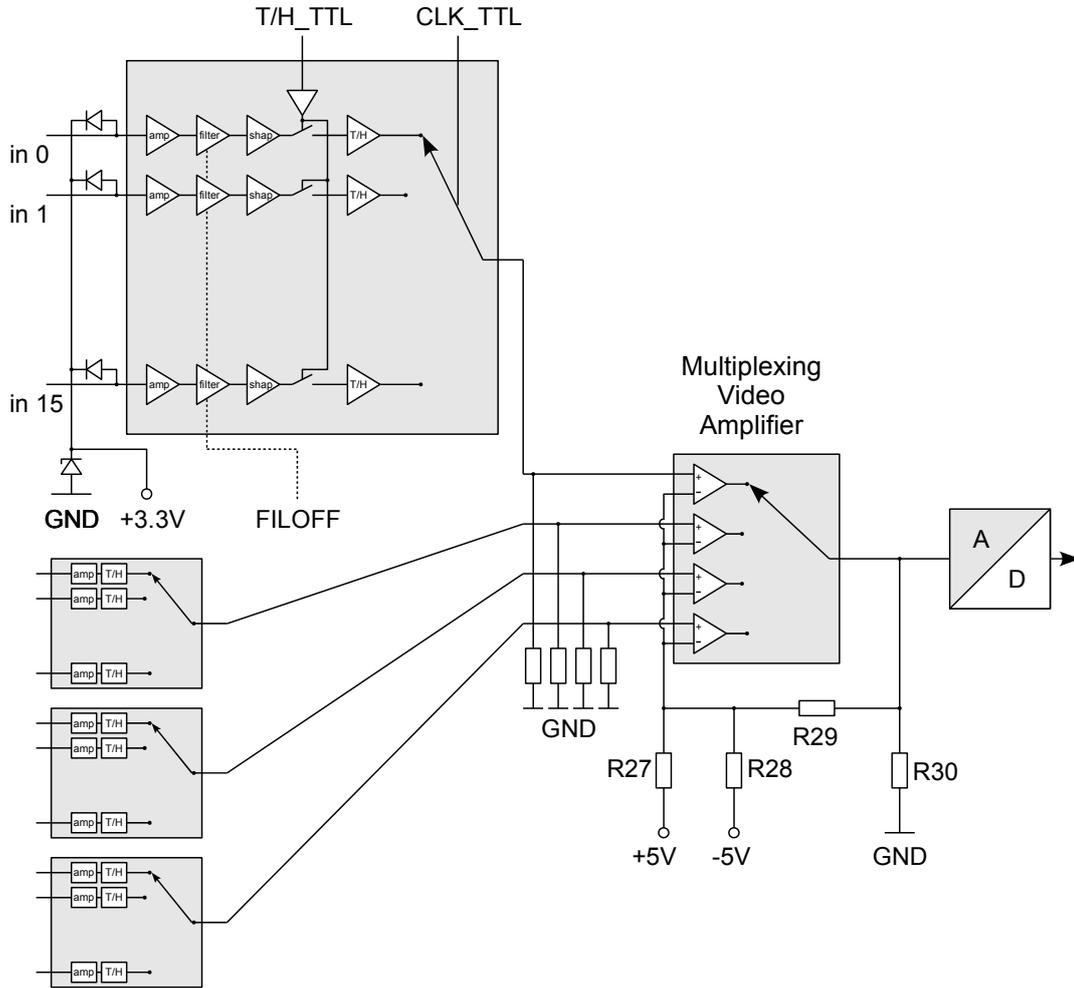

Figure 5.4: Schematic of the analog part of the frontend modules. The abbreviations used are: amp: charge sensitive amplifier; filter: optional deconvolution filter, switched off; shap: shaper; T/H: track&hold circuit; T/H_TTL: TTL pulse, activating the hold in the T/H circuit; CLK_TTL: clock, used to multiplex the 16 Gassiplex channels to the output; A/D: analog-to-digital converter.

5.3.2 The Multiplexing Amplifier's Baseline Value and Gain Factor

As can be seen from fig. 5.4, the working point of the four amplifiers in the video multiplexing amplifier as well as its gain can be adjusted by choosing appropriate values of the four resistors R27, R28, R29 and R30. The working point, i.e. the voltage at the inverting input, determines the lowest input voltage at the non-inverting input, that still causes a positive output signal.

All voltages in the network, including the output voltage, can be calculated by applying Kirchhoff's rules to the network shown in fig. 5.5. The operational amplifier is assumed to be ideal i.e. as soon as it experiences a potential difference at its inputs (+ denoting the non-inverting and − the inverting input) it gives out an infinitely high voltage with the same polarity as the difference $U_{in+} - U_{in-}$. The feedback resistor R29 feeds this output voltage back to the inverting input, thus pulling U_{in-} up until the difference between U_{in+} and U_{in-} vanishes. The whole system is then in equilibrium. These approximations allow for
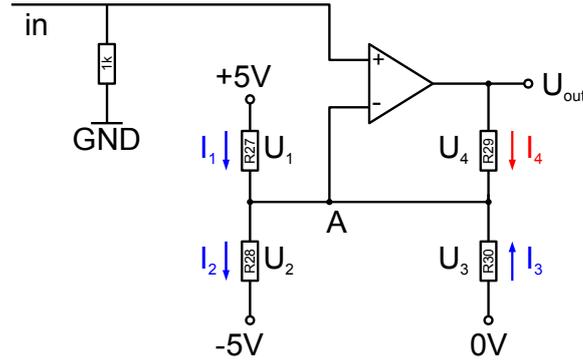
calculating the behavior of the amplifier.

Figure 5.5: Resistor network used to adjust the amplifier's output baseline and amplification.

Following the nomenclature of fig. 5.5 Kirchhoff's voltage law gives

$$U_1 + U_2 - 10\,\text{V} = 0 \tag{5.1}$$
$$U_3 + U_2 - 5\,\text{V} = 0 \tag{5.2}$$
$$U_1 - U_4 - 5\,\text{V} + U_\text{out} = 0 \tag{5.3}$$
$$U_4 - U_3 - U_\text{out} = 0 \ . \tag{5.4}$$
$$\tag{5.5}$$

Currents flowing into the node, named A, are drawn in red whereas those flowing out are drawn in blue. Kirchhoff's current law combined with Ohm's law thus gives

$$\frac{U_3}{R30} + \frac{U_4}{R29} + \frac{U_1}{R27} = \frac{U_2}{R28} \ . \tag{5.6}$$

And finally exploiting the ideal behavior of the amplifier i.e. that in equilibrium $U_\text{in+} = U_\text{in-}$:

$$U_\text{in} = 5\,\text{V} - U_1 \ . \tag{5.7}$$

The output voltage U_out as a function of the input voltage U_in is then

$$U_\text{out} = R29 \left(5\,\text{V} \left(\frac{1}{R28} - \frac{1}{R27} \right) + U_\text{in} \left(\frac{1}{R27} + \frac{1}{R28} + \frac{1}{R29} + \frac{1}{R30} \right) \right) \ . \tag{5.8}$$

Stating that the gain factor of the amplifier is defined by

$$G_U = \frac{U_\text{out1} - U_\text{out2}}{U_\text{in1} - U_\text{in2}} \ , \tag{5.9}$$

where U_in1 and U_in2 denote two different input voltages and U_out1 and U_out2 the corresponding output voltages, one can derive the closed loop gain of the circuit from eq. (5.8):

$$G_U = R29 \left(\frac{1}{R27} + \frac{1}{R28} + \frac{1}{R29} + \frac{1}{R30} \right) \ . \tag{5.10}$$

5.3.3 Adjustment of the Multiplexing Amplifier's Baseline and Gain

The calculated baseline values and gain factors in the three different resistor configurations of HADES [TUM Physik Dep. E12, 2000], HERMES[3] and Micromegas are listed in tab. 5.1.

	HADES original	HERMES	Micromegas
R27 $[\Omega]$	39k	33k	75k
R28 $[\Omega]$	22k	4.5k	3.3k
R29 $[\Omega]$	2.5k	3.3k	1.8k
R30 $[\Omega]$	7.5k	8.2k	33k
baseline [V]	0.47 ± 0.08	3.50 ± 0.11	2.85 ± 0.08
gain factor G_U	1.51	2.24	1.62

Table 5.1: *Calculated baseline values and gain factors in three different resistor configurations. When being idle, the output voltage of the four Gassiplex chips and thus the voltage on the multiplexing amplifier's input is $U_{in,baseline} = 0.15 \pm 0.05$ V.*

The multiplexing amplifier's baseline and gain in the HADES configuration is adjusted to pass positive signals to the ADC, having an input range of $+0.25$ V to $+4.25$ V. Shifting the baseline to high values, as done in the HERMES configuration, enlarges the dynamic range of detectable signals as much as possible. But this has considerable side effects as will be shown in sec.7.1, as the multiplexing amplifier is operated in saturation which causes problems like crosstalk, inefficiency and non-linearity.
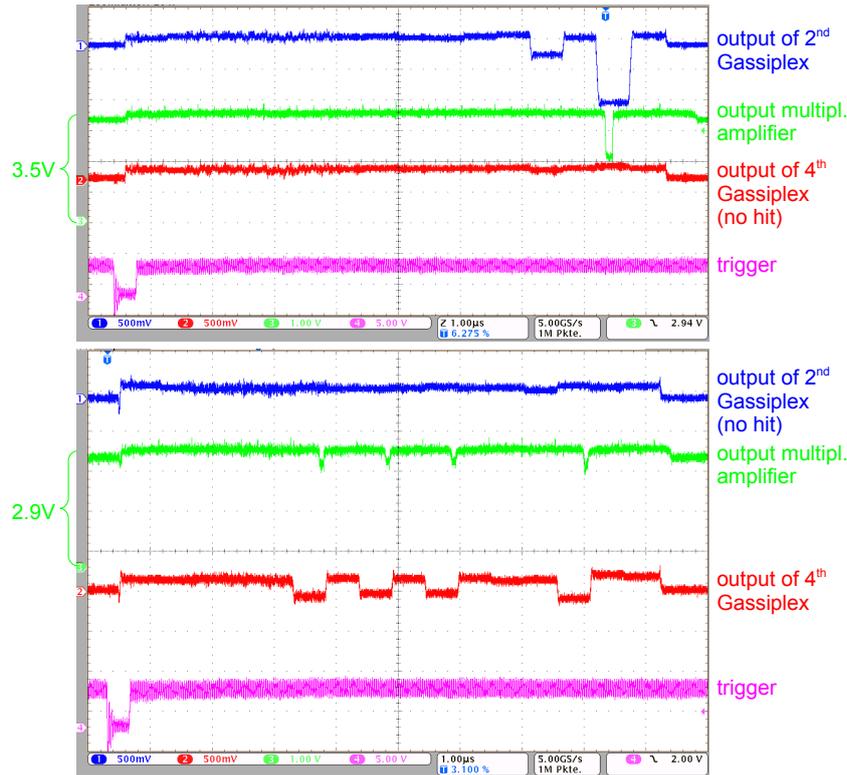

Figure 5.6: *Multiplexing amplifier's output (green) for an input from the second Gassiplex chip (blue) in the HERMES resistor configuration (top) and for an input from the fourth Gassiplex (red) in the Micromegas configuration (bottom). It is clearly visible, that in the latter configuration small signals are passed to the ADC, too. The trigger signal /TRG is drawn in magenta.*

High efficiency, no crosstalk and linearity in signal detection are achieved with the Micromegas

---
[3]Michael Böhmer, TUM Physik Dep. E12, private communication

configuration although the dynamic input range is not completely stretched. Results acquired with the readout running in this particular setup are summarized in chap. 7.

Fig. 5.6 displays the multiplexing amplifier's response to input pulses in the HERMES and in the Micromegas configuration. Obviously small signals are not amplified, but ignored when using the HERMES resistors. This leads on the one hand to low efficiency and on the other hand to a non-linearity in signal amplification. The numbered arrows mark the voltage origin. Comparison of the multiplexing amplifier's baseline with the values computed in tab. 5.1 reveals good agreement.

5.3.4 Protective Circuit with DC Coupling

The major difficulty encountered in Micromegas results from discharges between the mesh and the anode strips. Any readout electronics connected to the strips must thus be protected by a circuit, efficiently diverting discharges. The frontend modules themselves are only designed to sustain positive spikes.

The Gassiplex chips are capable of being directly coupled to the readout structure. The pad readout in the HADES experiment was realized this way. In a first try, the Micromegas' strips were directly connected to the frontend inputs.

As the Gassiplex' input channels are on negative potential, the simple Canberra 2004 protective circuit incorporating two double BAV99-diodes and several resistors described in sec. 4.3 is not applicable. The diodes would be conducting all the time and thus driving the Gassiplex chips into saturation and also diverting good signals directly to ground. By not grounding the diodes directly, but by using a cascade of up to eight Si-diodes, each of which starts to become conducting at around 0.4 V, this problem can be avoided[4]. The circuit is shown schematically in fig. 5.7. A similar effect could have been achieved by using Zener-diodes, but the BAV99 were chosen for their fast switching time, low capacitance and high current sustainability.
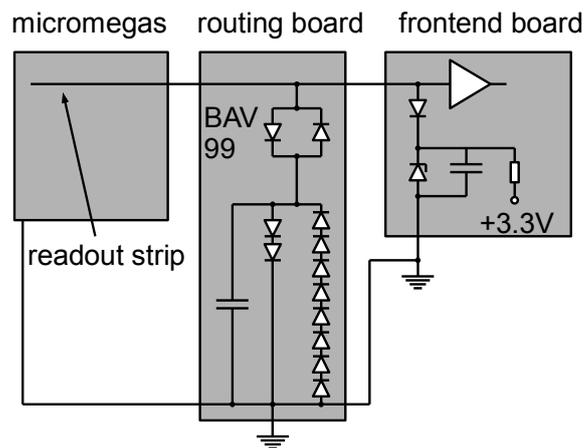

Figure 5.7: Protective circuit on the routing board, which incorporates one diode cascade for each polarity. The end of the diodes on the frontend modules is pulled up to +3.3 V by design of the frontend modules.

All channels are secured by double diodes, ending on a common signal line which is then grounded by the diode cascade.

---

[4]The nominal conduction threshold is 0.6 V.

5.3.5 Protective Circuit and AC Coupling

In the direct coupling configuration described above, the Gassiplex readout crashes after approximately three to four sparks, depending on the detector voltages. In addition, the signal's baseline sometimes moves to higher values after sparks; shifts of up to 200 ADC channels have been observed. The underlying mechanism is yet unknown, the problem though is expected to be caused by the high currents, flowing into the Gassiplex inputs in a discharge. Both the crashes and the baseline shifts were observed directly after a discharge. To considerably reduce these currents, that may exceed peak values of several ten amperes, two modifications were implemented: the protective circuit was reduced to one BAV99 diode per channel by capacitive coupling of readout strips to Gassiplex inputs. A better diversion of discharges is expected, since the series resistance of the diode cascade, being on the order of $5\,\Omega$ per diode in a conductive regime, can be avoided. Additionally, the threshold voltage for conduction is lowered from around $5.5\,\mathrm{V}$ to $0.6\,\mathrm{V}$. The second modification is a series $1\,\mathrm{k}\Omega$ resistor in the signal line, forming a current divider with the conducting diode and substantially reducing the current seen by the readout electronic in a discharge. Since the Gassiplex is charge sensitive, the effect of this resistor on the pulse height is expected to be lower than 10%.

The used circuit is shown schematically in fig. 5.8 for one readout strip.
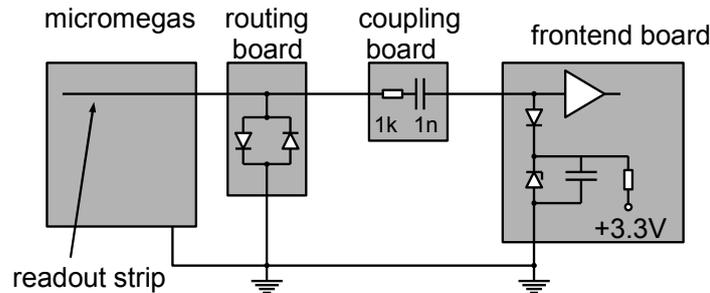

Figure 5.8: Schematic of the protective circuit and the capacitive coupling circuit for one strip. The diodes of all strips end on the routing board, which is grounded through the electronic readout.

5.4 Setup

5.4.1 Physical Setup for two Micromegas

The setup can be seen in the half-schematic of fig. 5.9. Two Micromegas are mounted on a support frame of $1000\,\mathrm{mm}$ height, composed of $30 \times 30\,\mathrm{mm}^2$ aluminum profiles, able to carry up to eight detectors. An additional shelf is built in, carrying one of the two trigger scintillators. To maximize the trigger rate, they are positioned as closely to the Micromegas as possible. The readout strips of both Micromegas are in parallel and point in z-direction to be able to reconstruct tracks in the two perpendicular dimensions x and y. High voltage slow control is realized in the same manner as described in sec. 3.4, the data acquisition computer is also responsible of controlling the iseg SHQ high voltage supplies via a RS232 interface.

Low voltage, necessary for frontend operation, is provided by a NIM module. To be able to balance fast fluctuations in the low voltages, caused by the beginning of readout cycles and by sparks within the detector, $2200\,\mu\mathrm{F}$ capacitors are installed on the low voltage distribution card and additional $220\,\mu\mathrm{F}$ capacitors on each bus card. It has been experimentally confirmed, that they are essential for stable operation. The detectors are connected in a serial mode to

the gas system described in sec. 3.5, the upper one being closer to the outlet valve to allow intruding air to be pushed out by the heavier detector gas.
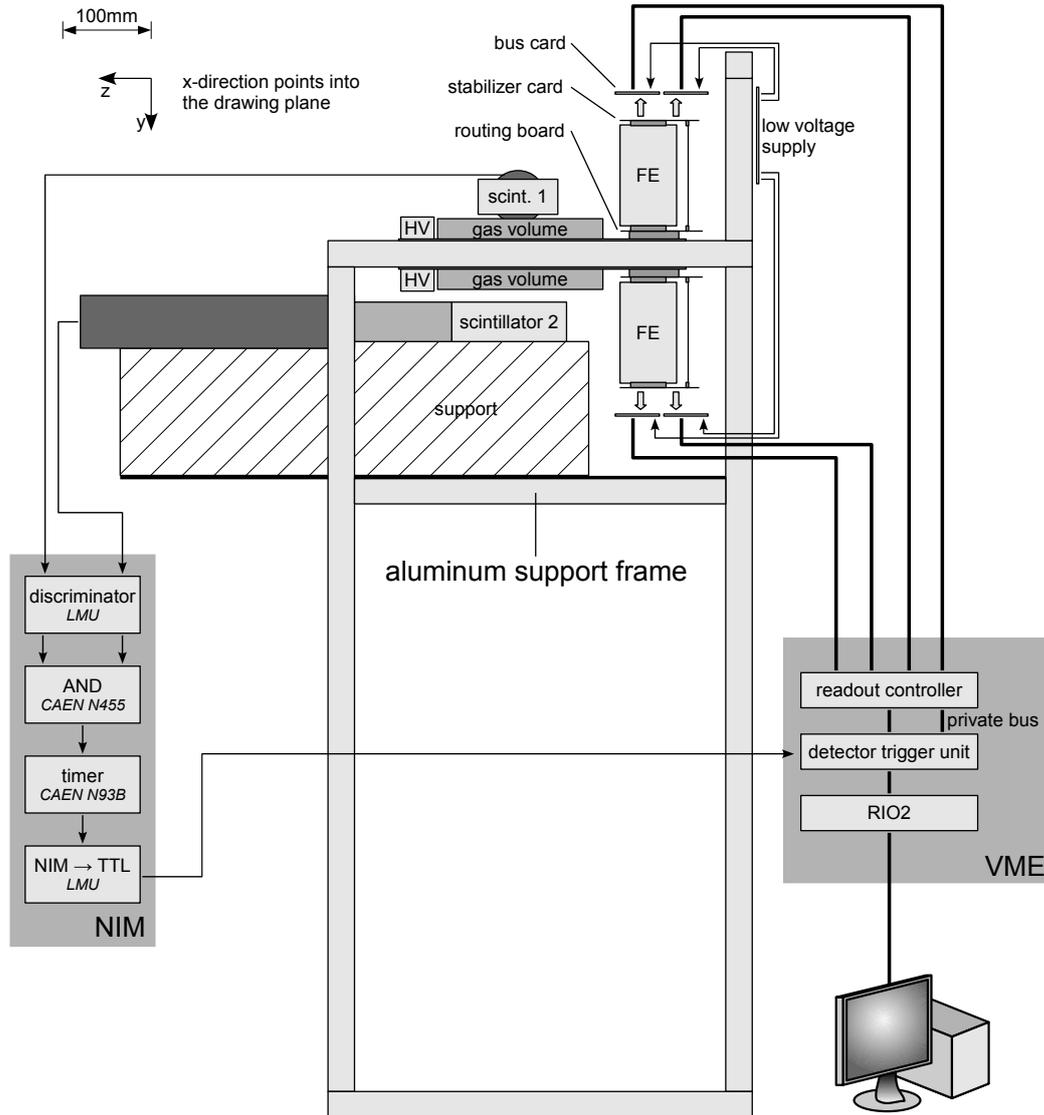

Figure 5.9: Setup and readout chain for coincident strip readout of two Micromegas. Both Micromegas are mounted on a stable aluminum frame to guarantee a parallel alignment of strips. The strips point into z-direction. The setup is drawn to scale whereas the electronic readout is pictured schematically. High voltage slow control is not drawn, although the data acquisition computer is also responsible of it. This setup allows for reconstructing tracks in the x-y-plane.

5.4.2   Setup for three Micromegas

Fig. 5.10 shows the changes in the setup for reading out three Micromegas. The lower scintillator was shifted down, reducing the trigger rate for cosmics quite considerably by a factor of 5. For low voltage supply of the frontend modules, the under dimensioned NIM low voltage module was replaced by a large 19 inch 10 A low voltage supply, as well capable of monitoring the four low voltages on the distribution board. The output voltages are stabilized, independent of the load and the cable length, to $\pm5.0\,\mathrm{V}$ and $\pm3.3\,\mathrm{V}$.
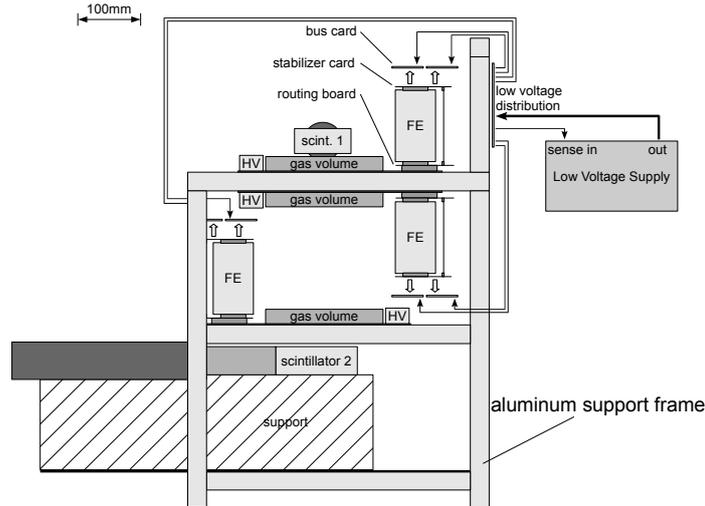
Figure 5.10: Setup for three Micromegas.

5.4.3 Trigger Circuit

A schematic of the trigger circuit is included in fig. 5.9. Both photomultipliers are running at $U_{PM} = -1.8\,\text{kV}$, a discriminator threshold of $U_{disc} = -30\,\text{mV}$ results in single detector count rates of $f_{sc1} = (9.0 \pm 0.3)\,\text{Hz}$ and $f_{sc2} = (4.3 \pm 0.2)\,\text{Hz}$ respectively. The errors result from an assumed normal distribution of muon hits. A coincidence time of 10 ns ensures the safe detection of muons, crossing both scintillators. Finally, the overall trigger rate is $(0.67 \pm 0.03)\,\text{Hz}$ for the two Micromegas setup and $(0.14 \pm 0.02)\,\text{Hz}$ in the three Micromegas setup.

In order to adjust the time between particle passage through the gas detectors and trigger to 550 ns, the end marker NIM-pulse of a CAEN timer is converted to TTL and fed to the DTU. Since the actual trigger signal `/TRG` is running on the VME private bus, an unused VME connector can be misused to access this signal and accurately measure the delay, caused by the timer, without having to consider the internal processing time of level converter and DTU. The point in time of the muon's passage is assumed to coincide with the falling edge of both scintillators' pulses.

5.4.4 Additional Grounding to Counteract Discharges

As already mentioned in sec. 5.3.5, an early readout setup crashed after a couple of discharges. This was traced back to the fact, that discharges lead to a collapse of the low voltages on the frontend modules. These are supplied with $\pm 5.0\,\text{V}$ and $\pm 3.3\,\text{V}$. Discharges are drained over the detector ground, which is defined by the frontend module's ground to avoid ground loops. As the ground potential is shifted during a discharge, the FPGA's low voltages are considerably altered. The FPGA[5], installed on each frontend, is responsible of handling the data acquisition and transfer.

The FPGA is able to cope with the relatively short and small breakdowns shown in fig. 5.11. Larger and longer drops though, are not tolerated and provoke unpredictable behavior, leading to a constant BUSY signal, indicating a major problem and deactivating readout. To stabilize the detector ground, an additional grounding cable was connected to the detector housing, routed to the VME crate incorporating the readout electronic. Since an unfiltered

---

[5]field-programmable gate array

connection leads to an increase of noise on the readout channels by a factor of three, the cable was wound around a ferrite core several times. Placing the core as close as possible to the detector effectively canceled this particular noise.

The bus cards used, need to carry four frontend modules each to work properly. Two bus cards are necessary to read out the whole detector. Since six modules are sufficient to read out 360 strips, two dummy modules are utilized. Ground pads of both dummy frontends were also connected to the detector housing. A third ground connection from the detector housing to both backplanes and to the VME crate was installed, although this does not seem to be essential.
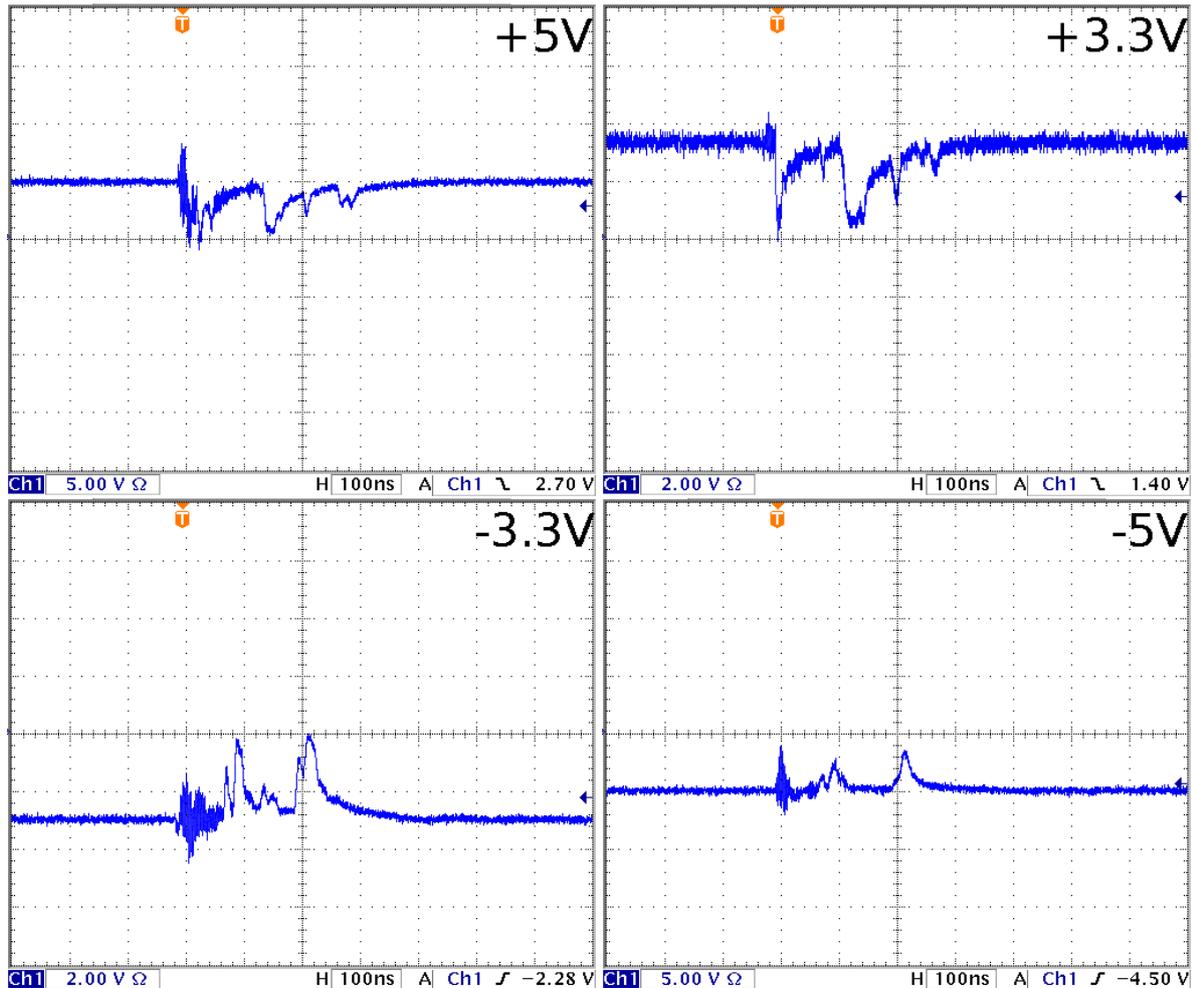

Figure 5.11: Four frontend supply voltages, tapped on the backplane with a differential voltage probe.

After taking these actions, the electronic readout runs stably for several days. In this time several hundred discharges have been counted.

5.5 Signal Analysis

The ADC value recorded for each channel corresponds to the signal's pulse height. Together with an event header and mapping information, like the readout controller's number, the port on the RC, the frontend's number and the channel, the ADC values, recorded in an event, are written to a binary file. The event header, consisting of four 32 bit data words, is followed

by one 32 bit data word per channel, containing the ADC and address information for each channel. A digital threshold comparison on the frontend modules is possible, such that only information about channels with $adcVal <$ threshold is written to file. This feature is not yet used, might be useful though when recording signals at higher rates, to improve readout speed and reduce data size.
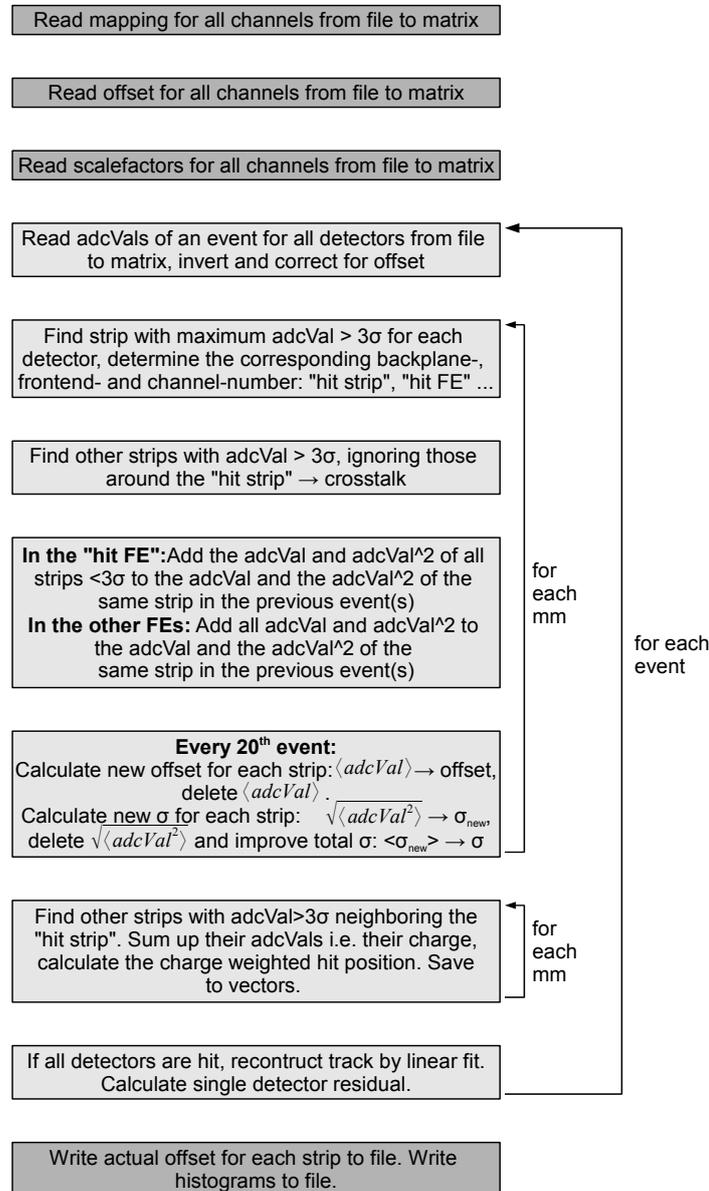

Figure 5.12: Flow chart of the analysis program used in the Gassiplex readout. The dark gray shaded boxes correspond to activity performed only once, the light gray shaded rectangles are repeatedly done functions, running through all events or through all detectors. The program searches for hit strips, strips that are not hit are used for dynamical offset correction. Tracks are reconstructed by straight line fits to the determined hit positions.

The first 7 lines of a raw data file, converted to ASCII format are shown below. For an improved readability, the information contained in the channel data word is extracted. The channel number `c` and the ADC value `adc` are displayed as integers:

```
SubEvtSize 0x00000c10, SubEvtDec 0x00020001, subEvtId 0x00000064, subEvtTag 0x00000100
*p: 0x00100274 dpr: 0x00 s: 0x00 r: 0x00 p: 0x02 m: 0x00 c: 0 adc: 628
```

```
*p: 0x00000259 dpr: 0x00 s: 0x00 r: 0x00 p: 0x00 m: 0x00 c: 0 adc: 601
*p: 0x00190262 dpr: 0x00 s: 0x00 r: 0x00 p: 0x03 m: 0x01 c: 0 adc: 610
*p: 0x00104285 dpr: 0x00 s: 0x00 r: 0x00 p: 0x02 m: 0x00 c: 16 adc: 645
*p: 0x00090276 dpr: 0x00 s: 0x00 r: 0x00 p: 0x01 m: 0x01 c: 0 adc: 630
*p: 0x0000427d dpr: 0x00 s: 0x00 r: 0x00 p: 0x00 m: 0x00 c: 16 adc: 637
```

`SubEvtSize` gives the size of the event i.e. the number of read out channels, `SubEvtDec` contains information about the data format, `subEvtId` is the readout controller's id, the last two digits of `subEvtTag` are the trigger tag `0x00` and the third to last digit the trigger source `0x1`. The other digits contain error informations; in this event, no errors were detected. Since a 10 bit analog-to-digital converter is used on the frontends, ADC values between 1 and 1024 are possible. That the baseline of the channels resides at values around 630 is due to the fact, that the dynamic range of the ADC is not completely usable in a negative signal configuration (see sec. 5.3.3). An analysis program `ana3.c` has been written, which reads the raw data file and handles the desired analysis. The flow chart fig. 5.12 gives a summary of the essentials of this program.

As already stated, the baseline ADC value is around 630 ADC channels. Signals are negative and correspond thus to ADC values < 630. In the analysis, the ADC values are corrected for offset and inverted such that the baseline resides at 0 and signals correspond to ADC values > 0. In the following discussion, the corrected and inverted values are denoted by the term $adcVal$.

Some explanatory comments on different blocks:

- The offset of each channel is dynamically recalculated every 20th event since the offset values drift. The offset drift is a known feature of the frontend modules and is probably due to temperature effects in the analog amplifiers. Typically, the offset values are corrected by values in the range of ± 0.3 ADC channels after an initial correction to the tabulated values, read from each detector's offset file. Of the 16 strips around the one with the largest ADC value, only those with $adcVal < 3\sigma$ are considered, when calculating the new offsets. The other 343 strips are considered, if their ADC value is smaller than 400 ADC channels. This large value is chosen to avoid an underestimation of the single strip standard deviation (see next paragraph). This method works fine, as long as more than 20 different strips detect hits regularly. Furthermore a trigger rate $> 0.5\,\mathrm{Hz}$ is necessary for a stable recalibration.

- A strip is considered as hit, when the ADC value of its signal is three times larger than its standard deviation. The standard deviation is calculated with the same conditions as the offset. Unlike the latter though, it improves during an analysis: An actual σ_{act} is recalculated with every 20th event. It is then added, correctly weighted, to the total standard deviation $\sigma = (n-1)/n \cdot \sigma + 1/n \cdot \sigma_{\mathrm{act}}$, where $n = \#_{\mathrm{event}}/20$ is the recalibration cycle's number.

- The hit in a detector is found by first determining the strip with the largest read out ADC value. The 16 neighboring strips are searched for ADC values bigger than 2σ. These values are then added, forming a measure of the total charge in an event. A charge weighted hit-position, usually being located between strips is also calculated in order to achieve spatial resolution better than the strip pitch of 250 µm .

- Since the amplification of the Gassiplex chips as well as the amplification of the multiplexing amplifier might differ from frontend to frontend or even from channel to channel, it is possible to scale each channel's ADC value separately by multiplying it with a real number. In all operations within the program, where the actual pulse height is important, the scaled values are used. In the course of this thesis, this feature was not

yet used, since one needs a sufficient amount of hits on each channel, to reliably determine the single channel amplification. Differing amplification factors might impact the spatial as well as the energy resolution. The difference in the amplification though, if there is any, is not expected to affect the spatial and the energy resolution, since the Micromegas itself only has an intrinsic energy resolution of around 25%, as will be shown in sec. 6.5.

- Tracks are reconstructed by fitting a straight line to the charge weighted hit-positions in the detectors, using the ROOT class TMinuit[6], as long as all Micromegas involved have registered a hit. The single detector spatial resolution is then computed by comparing the prediction, given by the straight line fit, to the registered hit in the respective detector. Of course, this method does not allow for extracting unbiased resolutions, since the hit-position in a certain detector is also included in the fit. Nevertheless, it should provide a good estimate of the spatial resolution (see sec. 7.6) and also allows for aligning the whole system internally (sec. 7.5).

If the fit quality is not within the expected range, one additional hit is searched in each detector, excluding the 40 strips around the first found hit. If additional hits, complying with the same quality conditions as the original hit, have been identified, the line fit is repeated for all possible permutations. The hit-positions of the permutation that is fit best, determined by the smallest χ^2, are considered for the following spatial analysis.

---

[6]http://root.cern.ch/root/html526/TMinuit.html

Chapter 6

General Performance

In this chapter, the Micromegas' general performance will be discussed. The results presented in the following are based on measurements with the single preamplifier readout, introduced in chap. 4. The behavior with respect to spatial readout will be discussed in chap. 7. Since the formation of signals in Micromegas deserves to be treated at full length, an own chapter is devoted to this (chap. 8).

6.1 Electron Transparency of the Mesh

It has been shown by Giomataris et al. [1996], that the transmission of electrons through a micro mesh depends on the ratio of the electric fields to both sides of the mesh $\xi = E_{high}/E_{low}$. The maximum transmission is more or less independent of the optical transparency. This behavior can be understood as follows: electrons drifting in the low field region towards the mesh are following the electric field lines. They can obviously not be transferred through the micro holes, if the field lines end on the mesh, as is the case for a low ratio ξ. Then again, for a high ratio ξ, the electric field lines in the low field region are influenced by the high electric field on the mesh's other side in such a way that they pass through the holes, allowing the electrons to reach the high field side.

A calculation of the electric fields reveals a transmission of 100% for a ratio $\xi = 20$. The measured electron transmission on the other hand, reaches 100% for a field ratio of 60, measured with an electroformed mesh with $8\,\mu m$ thick "wires" and $25\,\mu m$ pitch [Giomataris et al., 1996]. As the transmission is no experimentally accessible quantity in the present case, a ^{55}Fe source was used to investigate the pulse height's behavior as a function of the ratio ξ (see chap. 2 for the ^{55}Fe source).

A typical spectrum is shown in fig. 6.1. The K_α and K_β peaks cannot be resolved, the escape peak though is clearly visible. To the very left of the spectrum, the contribution of muons is also visible.

As the K_α line at $5.895\,keV$ produces the dominant peak and can be fit with a single Gaussian giving the pulse height and the standard deviation of $5.9\,keV$ X-rays in the detector, it can be used to study the Micromegas pulse height behavior under alteration of various parameters. The error, introduced by neglecting the K_β contribution to the dominant peak, is around 1% and thus neglible.

The pulse height of $5.9\,keV$ X-rays as a function of the ratio $\xi = E_{amp}/E_{drift}$ is given in fig. 6.2 for three different mixtures of Ar:CO$_2$. Starting at low ratios, the pulse height's increase for an increasing value of ξ is clearly visible. There seems to be a certain gas dependent
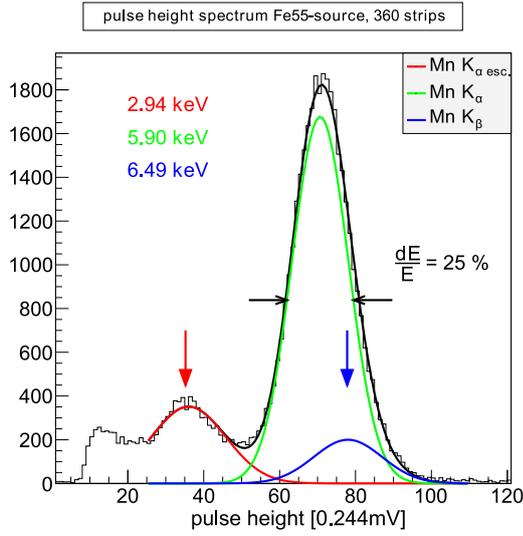
Figure 6.1: Typical ^{55}Fe pulse height spectrum for single plane readout with Ar:CO$_2$ 80:20. The colored arrows on top of the K_α escape peak and the K_β peak correspond to the expected values, obtained from linearly scaling the measured pulse height at $5.9\,keV$ to $2.94\,keV$ and $6.49\,keV$ respectively. A good agreement is visible. The energy resolution at FWHM of the K_α peak is around 25% in this run.

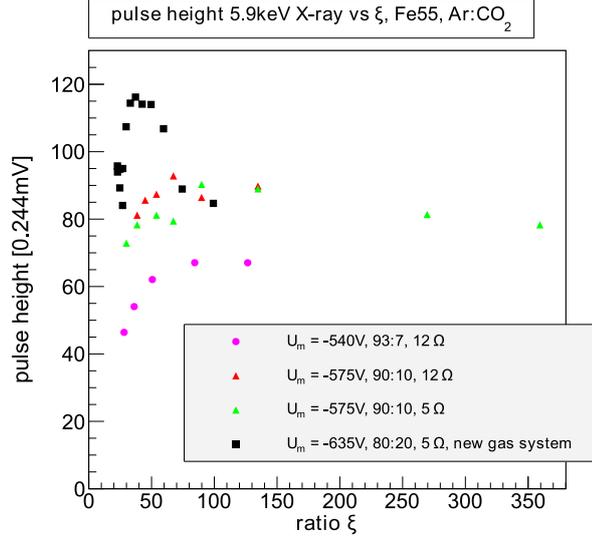*Figure 6.2: Pulse height of $5.9\,keV$ X-rays as a function of the ratio $\xi = E_{amp}/E_{drift}$.*

value of ξ though, where the pulse height is maximal. For higher ratios, it decreases again. Espargilière et al. [2009] observed a similar behavior and suggested an attachment of electrons to electronegative impurities in the detector gas. As some cross sections for attachment peak at low energy values (e.g. at $0.1\,eV$ for O$_2$ [Magboltz, 2010]), a decrease in the drift field could lead to a higher attachment probability. Another natural explanation is the recombination of electrons and ions, if the separating electric field is not high enough. Thus it is tried to achieve maximum pulse height at minimum drift field.

6.2   Efficiency

The efficiency is a particle or radiation specific quantity, defined by the ratio of the number of particles the detector actually detected and the total number of particles that went through the detector's sensitive area and should have been detected. Plastic scintillators combined with photomultipliers are well suited for determining the latter quantity since they can easily be produced in various sizes and are furthermore highly efficient for muons, onto which I will concentrate in the following section.

The setup which allows for determining the Micromegas' efficiency has been introduced in sec. 4.2 and is shown in a simplified version in fig. 6.3. The Micromegas' charge signal is converted and amplified by a charge sensitive preamplifier (Canberra 2004) and given to a fast analog-to-digital converter. This FADC can be triggered in three different ways: In the twofold coincidence cosmic muons are seen by the two scintillators in coincidence (blue, 2fold coinc.). In the threefold coincidence (green, 3fold coinc.) the Micromegas' signal is required to coincide with both scintillators' signal. For tests with e.g. a ^{55}Fe-source the Micromegas
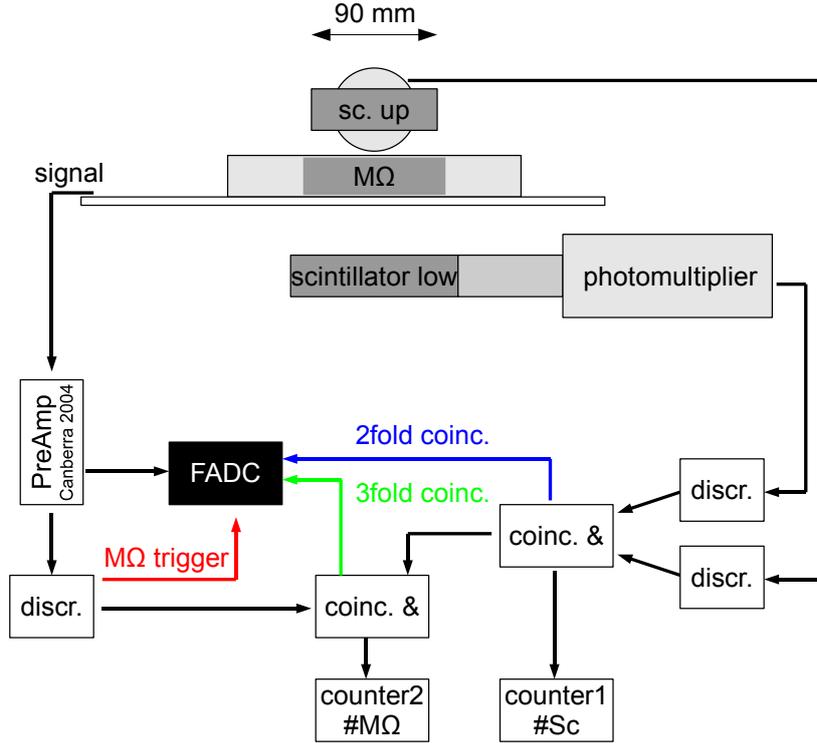
by itself can trigger the FADC (red, MΩ trigger).

Figure 6.3: Schematic and simplified view of the experimental setup. The efficiency can be calculated by comparing the two numbers #MΩ, which gives the number of threefold coincidences and #Sc, representing the number of scintillators' coincidences.

By comparing how many events the Micromegas saw, to how many it should have seen, an efficiency can be calculated:

$$\varepsilon = \frac{\#\text{M}\Omega}{\#\text{Sc} \cdot \text{f}_{\text{geom}}} \ , \tag{6.1}$$

where #MΩ is the number of threefold, #Sc is the number of twofold coincidences and f_{geom} is a correction factor accounting for the fact, that the scintillators cover an area slightly bigger than the active area of the Micromegas. For the calculation of this factor see sec. 4.4.

Typical cosmic pulse height spectra for all gas mixtures used are shown in fig. 6.4. As expected, an asymmetric, Landau like distribution is observed, since the Micromegas classifies as a thin detector (see sec. 2.1). It should be noted, that the energy spectrum is as expected to be wider than the Landau distribution and furthermore it begins at the origin. The energy distribution's width depends on four effects: the asymmetric energy loss, due to production of delta electrons, the momentum distribution of cosmic muons, the angular distribution of muon tracks in the detector and the Micromegas' energy resolution. The latter will be extensively treated in sec. 6.5.

A comparison of the measured most probable energy loss and the expectation is possible. The pulse height of 5.9 keV X-rays in Ar:CO$_2$ 80:20, at $E_{\text{amp}} = 49.6$ kV/cm, $E_{\text{drift}} = 2.06$ kV/cm and $p = 1013$ mbar is $ph_{5.9\text{keV}} = 27.8 \pm 2.8$ mV. This gives a conversion factor between deposited energy and pulse height of 4.71 ± 0.47 mV/keV. The cosmic pulse height distribution of run 234, shown in fig. 6.4, is acquired at the same gas and electric field parameters. The most probable energy loss corresponds to a pulse height of $ph_{\text{mpv}} = 4.8 \pm 0.1$ mV and thus
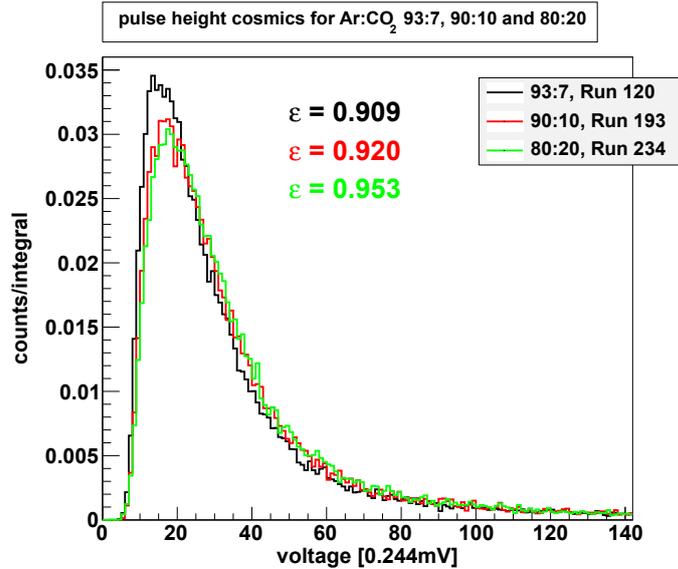
Figure 6.4: Pulse height spectra for cosmics, measured with three different mixtures of Ar:CO$_2$. The integral of each dataset is scaled to 1.

to an energy loss of $E_{\mathrm{mpv}} = 1.02 \pm 0.12\,\mathrm{keV}$. This is in agreement with the most probable energy loss of $3\,\mathrm{GeV}$ muons in $6\,\mathrm{mm}$ Ar:CO$_2$ 80:20 of $E = (1.0 \pm 0.1)\,\mathrm{keV}$, calculated with a GEANT4 simulation and shown in fig. 2.3. Following the values, given in tab. 2.1, the mean energy loss of a minimum ionizing particle in the $6\,\mathrm{mm}$ drift space of a Micromegas, running with an Ar:CO$_2$ 80:20 mixture at NTP is $E_{\mathrm{mean}} = 1.62\,\mathrm{keV}$. This value lies well in the expected range, since the mean energy loss is expected to be somewhat bigger, than the most probable.

The efficiency's increase with an increasing fraction of carbon dioxide is due to the possibility of achieving higher pulse heights as more quencher is added. Stable operation is possible at higher amplification field, since discharges are effectively suppressed. Evidence for this statement is given in sec. 6.4. With respect to efficiency, Ar:CO$_2$ 80:20 shows advantages over the other mixtures.

The Micromegas' efficiency ε to minimum ionizing particles as a function of the electric field in the drift region is shown in fig. 6.5 for three different gas mixtures of Ar:CO$_2$ and various amplification fields. For all gas mixtures it shows a distinct behavior: starting at small values of E_{drift}, ε rises to a certain maximum value, which is reached for drift fields around $500\,\mathrm{V/cm}$ for Ar:CO$_2$ 93:7, $700\,\mathrm{V/cm}$ for 90:10 and $1300\,\mathrm{V/cm}$ for 80:20. Going to higher values of the drift field causes a decrease of ε.

By having a look at the pulse height of the signal of $5.9\,\mathrm{keV}$ X-rays from a ^{55}Fe-source (fig. 6.6) one can understand this typical behavior of ε. The pulse height seems to be limited by two effects as already discussed in sec. 6.1: the voltage in the drift area has to be big enough to ensure a safe collection of as much charge from ionization as possible. On the other hand, the mesh's transparency for electrons depends on the ratio of the electric fields in the drift and in the amplification gap $E_{\mathrm{amp}}/E_{\mathrm{drift}}$.

For a decreasing ratio of amplification field to drift field i.e. an increasing drift field, an increasing number of field lines coming from the cathode end on the mesh. Electrons from ionization following these field lines thus cannot reach the amplification gap. Both effects balance each other at the drift fields given above, causing a maximum in the pulse height and also in the efficiency. It should be stressed, that the amplification field is limited by
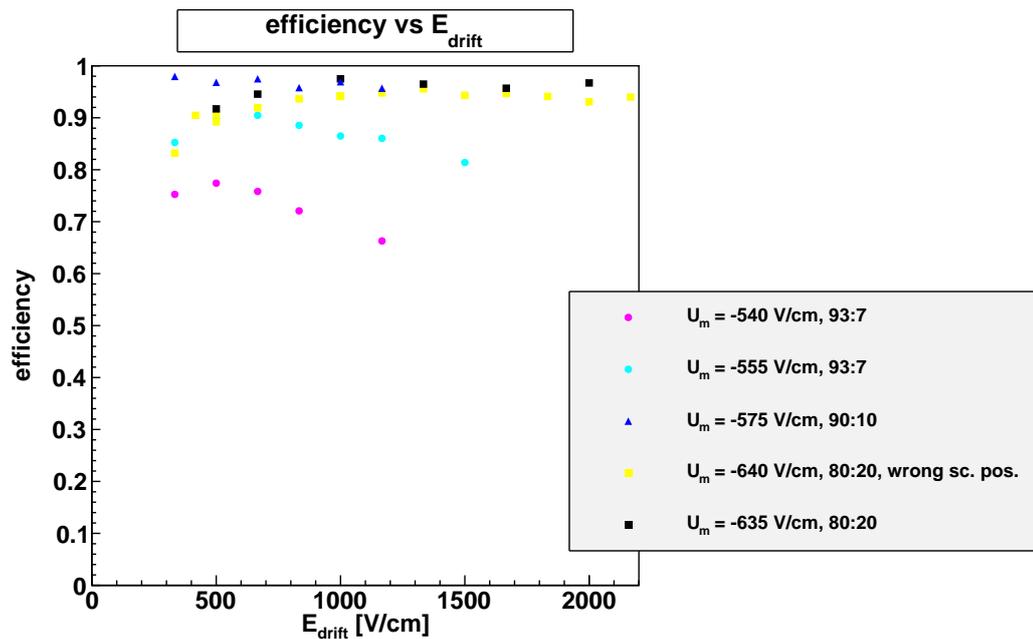
break-through.

Figure 6.5: *Efficiency to MIPs as a function of the drift field E_{drift} for three different gas mixture of Ar:CO$_2$ namely 93:7, 90:10 and 80:20 and various amplification fields. The data have been acquired with the single preamplifier readout.*
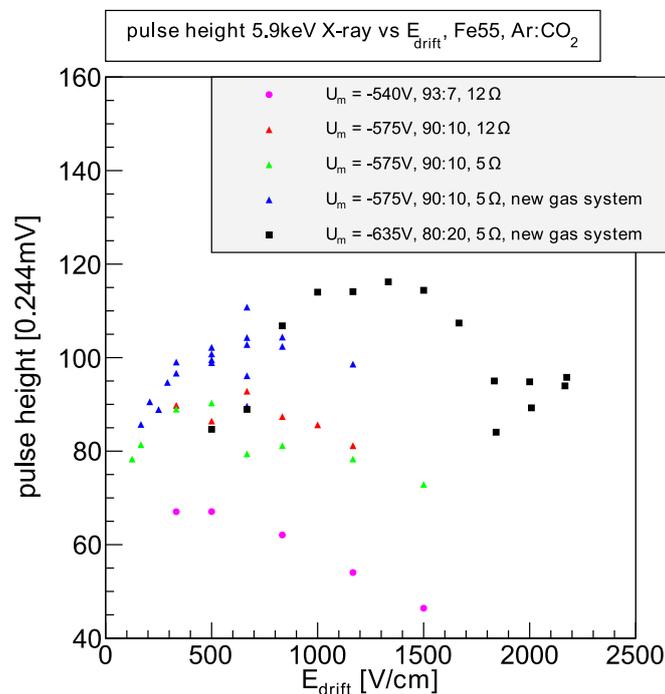

Figure 6.6: *Pulse height of ^{55}Fe's 5.9 keV line for gas mixtures of Ar:CO$_2$ 93:7, 90:10 and 80:20 as a function of E_{drift}.*

The pulse height of muon signals is obviously the limiting factor for the Micromegas' efficiency. Muons causing signals with an amplitude below the discriminator threshold are not detected.

The efficiency for minimum ionizing particles decreases with decreasing electron transparency

because as the signals become smaller more and more signals vanish in the noise baseline.

Since the creation of primary charge[1] in ionization is a statistical process following the poisson statistic, the theoretical efficiency [Sauli, 1977] of a perfect detector is

$$\varepsilon = 1 - e^{-n_p[\mathrm{cm}^{-1}] \cdot x[\mathrm{cm}]} \; , \tag{6.2}$$

where n_p is the number of electron-ion pairs per centimeter produced in primary ionization and x is the length of a particles track in the detector. For Argon $n_p = 25\,\mathrm{cm}^{-1}$ [K. Nakamura et al. (Particle Data Group), 2010]. The drift gaps in the Micromegas have been chosen to be rather large to avoid this issue. The theoretical efficiency for a perfect Micromegas with drift gap of $2\,\mathrm{mm}$ is $\varepsilon = 0.993$, in comparison to $\varepsilon = 1 - 3.1 \cdot 10^{-7}$ for a $6\,\mathrm{mm}$ drift gap.

The experimental efficiency for cosmics reaches up to 98% in the single preamplifier setup. This is about the expected value, since the 1440 pillars, supporting the mesh and covering around 1.1% of the sensitive area, are expected to limit the efficiency.

6.3 Gas Amplification

A ^{55}Fe source is used to experimentally determine the gas gain at various parameter points. The spectra and the derivation of the pulse height have been discussed in sec. 6.1. To cancel temperature effects and to put the discussion on a firm statistical basis, the pulse height at various amplification fields and various experimental conditions is extracted from 30 different measurements with an average of 7.5k events each. A mean pulse height $\overline{ph}$ is calculated from the correctly weighted pulse heights measured with 5, 10 and 18 readout strips, connected together. Since the amount of charge, measured with a charge sensitive preamplifier, is a function of the number of read out strips and is furthermore always smaller than the total amount of charge created, the measured pulse heights ph_5, ph_{10} and ph_{18}, being directly proportional to the measured charges, need to be scaled up by a factor, extracted from tab. 8.3. A detailed explanation of the pulse height dependence on the number of readout strips can be found in chap. 8. As the Canberra 2004 preamplifier has a known charge to voltage conversion factor of $1\,\mathrm{V/pC}$ [Canberra Industries, Inc., 2007], the amount of charge created can be derived directly from the mean pulse height:

$$Q_{\mathrm{total}}(E_{\mathrm{amp}}) = \frac{1}{3}\left(\frac{ph_5(E_{\mathrm{amp}})}{0.88} + \frac{ph_{10}(E_{\mathrm{amp}})}{0.85} + \frac{ph_{18}(E_{\mathrm{amp}})}{0.81}\right) \cdot \frac{\mathrm{pC}}{\mathrm{V}} \; . \tag{6.3}$$

The error $\Delta Q_{\mathrm{total}}(E_{\mathrm{amp}})$ is derived from the squared sum of the standard deviations in the different strip configurations σ_5, σ_{10} and σ_{18}:

$$\Delta Q_{\mathrm{total}}(E_{\mathrm{amp}}) = \sqrt{\left(\frac{\sigma_5(E_{\mathrm{amp}})}{3 \cdot 0.88}\right)^2 + \left(\frac{\sigma_{10}(E_{\mathrm{amp}})}{3 \cdot 0.85}\right)^2 + \left(\frac{\sigma_{18}(E_{\mathrm{amp}})}{3 \cdot 0.81}\right)^2} \cdot \frac{\mathrm{pC}}{\mathrm{V}} \; . \tag{6.4}$$

Eq. (2.5) gives for a deposited energy of $5.9\,\mathrm{keV}$ in an $Ar{:}CO_2$ 80:20 mixture at NTP an average number of 224 electron-ion pairs, corresponding to a charge of $0.03576\,\mathrm{fC}$. The experimental gain is thus

$$G_{\mathrm{exp}}(E_{\mathrm{amp}}) = \frac{Q_{\mathrm{total}}(E_{\mathrm{amp}})}{0.03576\,\mathrm{fC}} \; . \tag{6.5}$$

---

[1]Here primary and secondary ionization is distinguished.

Assuming a constant electric field in the amplification region, thus completely neglecting the mesh wires, the theoretical gain factor can be derived directly from eq. (2.9):

$$G_{\text{th}} = e^{\alpha x} \, , \tag{6.6}$$

where α is the first Townsend coefficient, calculated with MAGBOLTZ and x is the dimension of the gas amplification region. A comparison of the theoretical and experimental gain factors as a function of the electric field can be found in fig. 6.7.
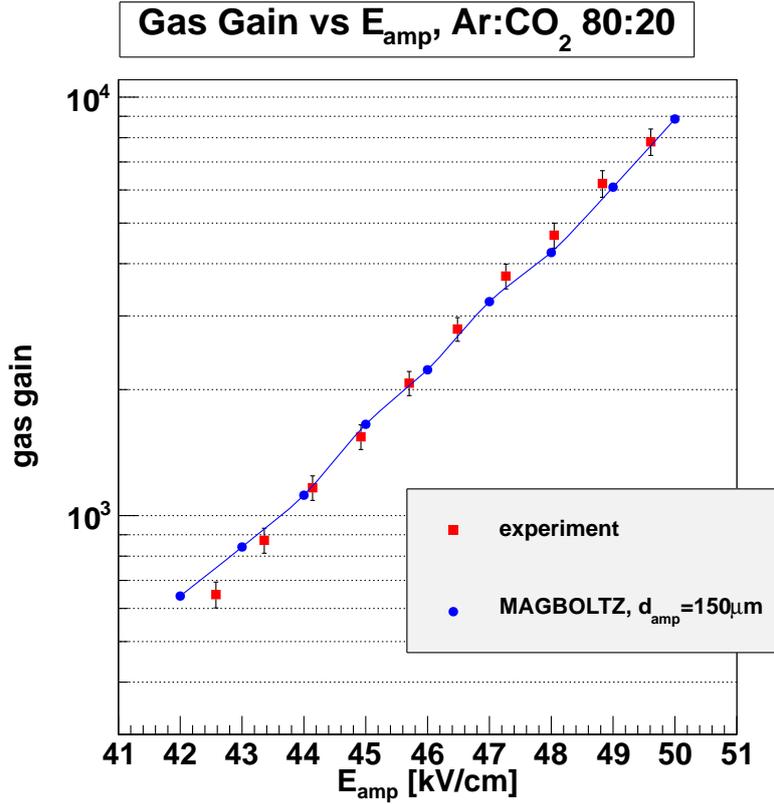

Figure 6.7: Theoretical and experimental gas gain factors in Ar:CO$_2$ 80:20 at NTP as a function of the electric field in the amplification gap E_{amp}.

To match the expected values to the measured, it has to be assumed, that the amplification region is $x = 150\,\mu\text{m}$ wide, in contrast to the $128\,\mu\text{m}$ amplification gap, actually realized. This is at least plausible, since the wires have completely been neglected in the derivation of the theoretical gain. It is expected though, that the electric field in close proximity to the wires with a diameter of only $18\,\mu\text{m}$, is considerably larger than in the assumed homogeneous case. The gas gain in the mesh region should thus be bigger than assumed, legitimating the amplification region's larger width. On the other hand, the preamplifier's gain factor is not verified, thus the aging of capacitors in the amplifier might have an influence on the measured pulse height, too.

Nevertheless, a good agreement between measured and expected gas gains is visible. This discussion reveals, that the gas amplification occurs throughout the whole amplification gap, and not just in the stronger fields in the wire region. This will have an influence on the discussion of signal formation in Micromegas (chap. 8).

6.4   Sparking

6.4.1   The Problem

The major difficulty encountered in Micromegas results from sparking. The sources of the sparks, observed in the lab, are either single heavily ionizing particles, particle showers, produced in the atmosphere or in the concrete ceiling [Zibell, 2010, p. 20 ff.], or internal discharges, caused by high electric fields in the proximity of single mesh wires. Sparks become manifest in a (complete) discharge of the mesh onto the anode strips. Discharges or current trips of the cathode have not been observed. The issues of necessary readout electronic protection have been discussed in secs. 4.3, 5.3.4 and 5.3.5. In this section, the spark rate as a function of various parameters like the gas mixture and pressure and the electric field in the amplification gap, is discussed.

It is important to note, that the following discussion will be of a more qualitative manner. Because of the various sources of sparks, none of which can be directly controlled, and also because of the neglected influence of temperature and gas mixture stability, the spark frequency f_{spark} shows quite considerable fluctuations. Great care was taken, to only compare runs, where the ambient conditions were at least quite similar. Despite of these difficulties, the major trends are clearly visible.

Other groups are working on reducing the spark's impact and temporal duration by using resistive readout strips or resistive layers an top of normally conducting readout structures [Alexopoulos et al., 2010a; Schade and Kaminski, 2010]. Resistive layers are unfortunately charged up during high rate measurements such that a temporal pulse height variation occurs.

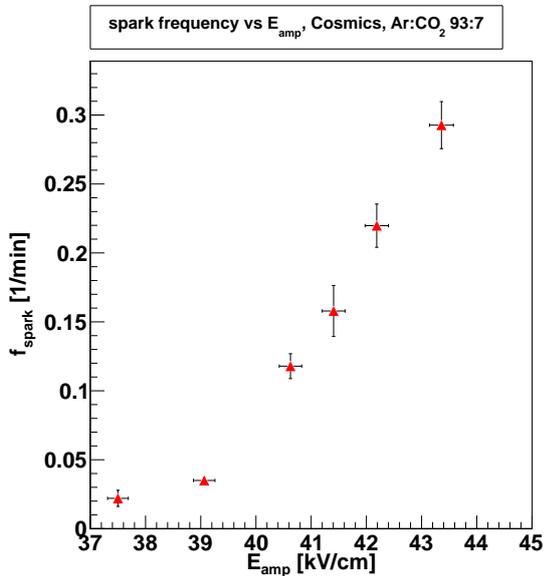### 6.4.2   Different Gas Mixtures

Figure 6.8: Spark frequency as a function of the electric field between mesh and anode for cosmic runs with $Ar:CO_2$ 93:7.
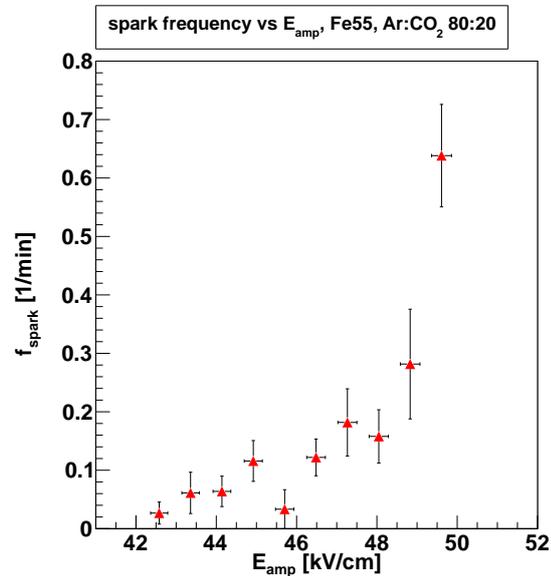
Figure 6.9: Spark frequency with $Ar:CO_2$ 80:20 under irradiation by soft X-rays from a ^{55}Fe source.

As an increased fraction of CO_2 quencher gas should suppress sparks, $Ar:CO_2$ 90:10 and 80:20 mixtures have been investigated, in addition to the standard ATLAS muon spectrometer mixture of 93:7. The higher the fraction of carbon dioxide, the lower the first Townsend

coefficient. The gas gain decreases accordingly as can be seen in fig. 2.7. To achieve the same gas gain with Ar:CO_2 80:20 as with 93:7, the electric field has to be around $5\,kV/cm$ higher. The spark frequency as a function of the electric field in the amplification region between mesh and anode is shown in figs. 6.8 and 6.9 for two different gas mixtures and measurements with cosmics and soft X-rays. They state the almost trivial observation, that the spark frequency rises with rising electric field.
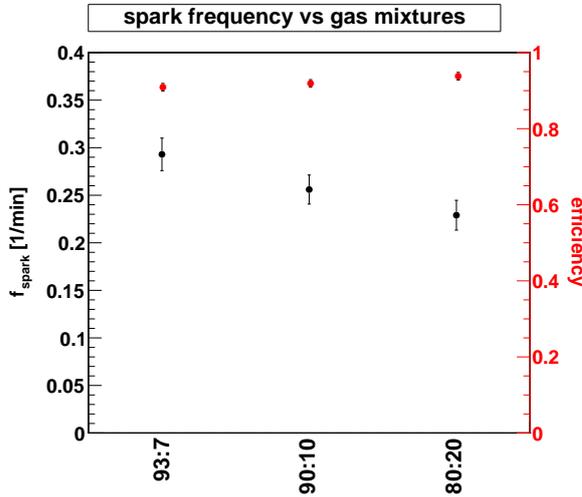

Figure 6.10: Spark frequency for three different mixtures of Ar:CO_2 at NTP in cosmic runs. The efficiency measured in each run is superimposed.
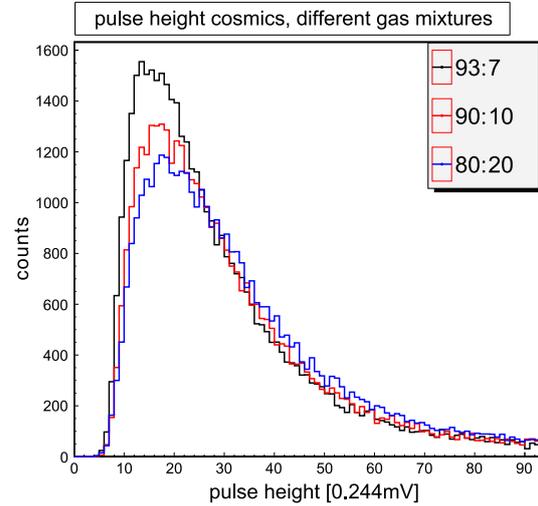

Figure 6.11: Pulse height spectrum for three different mixtures of Ar:CO_2 at NTP in cosmic runs. The spectra are taken from the same three runs as the data shown in fig. 6.10.

It is thus not obvious a priori, that a mixture with a higher fraction of quenching gas performs better with respect to spark frequency. The efficiency to cosmics offers a fixpoint when comparing measurements with different gas and electric field parameters. In fig. 6.10 the spark frequency as a function of the gas mixture for cosmic runs is shown. These three measurements have been chosen for the similarity of the measured efficiencies.

As the fraction of carbon dioxide increases, the spark frequency decreases. The efficiency on the other hand increases, too, since the amplification field and thus the mean pulse height can be higher. The three runs' pulse height spectra are shown in fig. 6.11. The slight increase of the mean pulse height is visible. At the relatively high electric fields needed, to achieve the desired efficiencies for single plane readout with a single preamplifier, Ar:CO_2 80:20 shows advantages over 90:10 and 93:7.

A little disadvantage of an 80:20 mixture is due to the fact, that, in order to achieve the same efficiency, the voltage difference between mesh and anode has to be greater. The energy, stored in the mesh-anode capacitor is proportional to the voltage squared

$$W = \frac{C}{2}U^2 \ . \tag{6.7}$$

Since the mesh discharges completely in a spark, the readout electronics is exposed to a larger amount of energy, when using 80:20 rather than 93:7. Whether this affects the long term stability in a negative way, has to be examined carefully.

6.4.3   Elevated Gas Pressure

Another possibility to reduce the spark frequency, is to operate the detector at a higher pressure. More charge should be produced from ionization, while the gas gain at the same field values is slightly lower. This should selectively enlarge the pulse height of cosmics while decreasing the pulse height for X-rays, presumably at least partly responsible of triggering sparks.
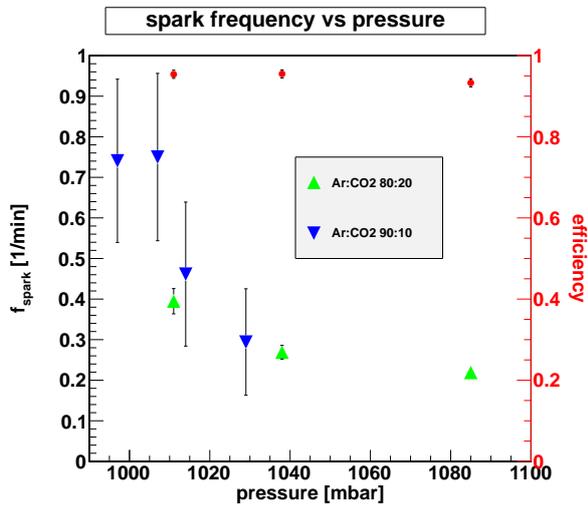

Figure 6.12: Spark frequency for different pressures and mixtures of $Ar:CO_2$ at room temperature in cosmic runs. The efficiency measured in each run is superimposed.
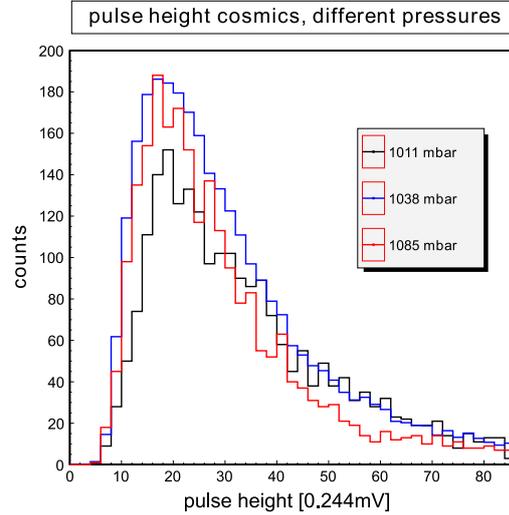
Figure 6.13: Pulse height spectra for the three $Ar:CO_2$ 80:20 cosmic runs, shown in fig. 6.12, measured at different pressures.

As expected, the frequency of sparks decreases with elevated pressure (fig. 6.12). The efficiency is at a maximum for a pressure of $p = 1038$ mbar, although this result is not significant, since the difference between $\varepsilon_{1011\,\mathrm{mbar}}$ and $\varepsilon_{1038\,\mathrm{mbar}}$ is smaller than the respective error of each value. An elevated pressure is however not favorable since the muons' mean pulse height decreases with increasing pressure as can be seen in fig. 6.13. This is due to the reduction of the gas gain, since the first Townsend coefficients decrease with increasing pressure. Thus the Micromegas should be operated at a pressure around 1013 mbar, yielding the best compromise between spark frequency, high efficiency and relatively high pulse height.

6.5   Energy Resolution

A gas detector's energy resolution is limited by the statistical nature of ionization and, to a smaller extent, gas amplification. A third and in principle avoidable contribution Δ_o comes from parameter inhomogeneities such as gas composition, pressure and temperature fluctuation, spatial inhomogeneities within the detector or fluctuations in the readout electronics. For an ideal detector $\Delta_o = 0$. Δ_o could of course be absorbed into the other terms, since e.g. gas parameter variations affect ionization and gas amplification.

The mean energy, measured after a repeated deposition of a fixed amount of energy in the detector, depends on the mean number of electron-ion pairs produced by ionization $\overline{n}$, the mean gas gain $\overline{G}$ and a mean conversion factor $\overline{f_{\mathrm{conv}}}$, linking the number of charges to an energy value:

$$E = \overline{n} \cdot \overline{G} \cdot \overline{f_{\text{conv}}} \ . \tag{6.8}$$

This factor $\overline{f_{\text{conv}}}$ also contains information about the fraction of electrons from ionization, reaching the amplification region.

Applying Gaussian error propagation, the energy resolution σ_E/E is thus simply the quadratic sum of the three contribution's relative errors. For m Poisson distributed measurements, the relative error is $\sigma_m/\overline{m} = 1/\sqrt{m}$. Due to energy conservation, ionization is not a truly statistical process such that its true contribution to the energy resolution is by a factor $\sqrt{F}$ smaller than the solely statistical one, where F is the so called Fano factor [Grupen and Shwartz, 2008]. A mono energetic line in an energy spectrum is thus always smeared to a Gaussian, classified by the mean E and the standard deviation σ_E:

$$\frac{\sigma_E}{E} = \sqrt{\frac{F}{\overline{n}} + \left(\frac{\sigma_{\overline{G}}}{\overline{G}}\right)^2 + (\Delta_o)^2} \ . \tag{6.9}$$

where σ_G is the gas gain's standard deviation[2].

The gas dependent Fano factor is $F = 0.23 \pm 0.05$ for argon [Hashiba et al., 1984]. Usually the energy resolution is specified as full width half maximum value (FWHM) over mean

$$\frac{\Delta E_{\text{FWHM}}}{E} = 2\sqrt{\ln 4}\frac{\sigma_E}{E} \approx 2.355\frac{\sigma_E}{E} \ . \tag{6.10}$$

For an ideal Micromegas i.e. assuming solely statistical variations, the irreducible FWHM energy resolution for $5.9\,\text{keV}$ X-rays at a gas gain of $\overline{G} = 7800$ in an Ar:CO_2 80:20 mixture at NTP is then

$$\left.\frac{\Delta E_{\text{FWHM}}}{E}\right|_{\text{ideal}} = 2.355\sqrt{\frac{0.23}{224} + \frac{1}{7800}} = 8.0\% \ . \tag{6.11}$$

A typical ^{55}Fe pulse height spectrum is shown in fig. 6.1. The experimental energy resolution is determined by fitting the common $\text{Mn}_{K\alpha}+\text{Mn}_{K\beta}$ line with a Gaussian, extracting its mean and standard deviation and calculating the FWHM energy resolution using eq. (6.10). The standard deviation is assumed to be equal to the $5.9\,\text{keV}$ line's. Ignoring the $\text{Mn}_{K\beta}$'s contribution results in an over estimation of the energy resolution by about 1%. This is acceptable, as the fit of the peak with two Gaussians is avoided, which would be a source of error, too.

The $5.9\,\text{keV}$ line's energy resolution as a function of the drift field for three different mixtures of Ar:CO_2 is shown in fig. 6.14. Optimum resolutions of 23% are achieved, which is quite satisfactory and in agreement with measurements in bulk Micromegas, reported by other groups (figs. 6.15 and 6.16).

The difference between the theoretical energy resolution of 0.08 and the minimum value of e.g. 0.24 for Ar:CO_2 80:20 at $E_{\text{drift}} = 1200\,\text{V/cm}$ is probably due to an inhomogeneity in the gas amplification. A relative error of $\sigma_G/\overline{G} = 9.7\%$ would, together with the assumption, that additionally only statistical errors are present, account for the observed energy resolution:

---

[2]It should be noted, that some authors use a different notation. Charles and Cooke [1968] e.g. specify the energy resolution as $\frac{\sigma_E}{E} = \sqrt{\frac{F}{\overline{n}} + \frac{1}{\overline{n}}\left(\frac{\sigma_G}{G}\right)^2 + (\Delta_o)^2}$, where σ_G is the single avalanche standard deviation, that can have very large values. In eq. (6.9) $\sigma_{\overline{G}}$ denotes the mean gas gain's standard deviation.
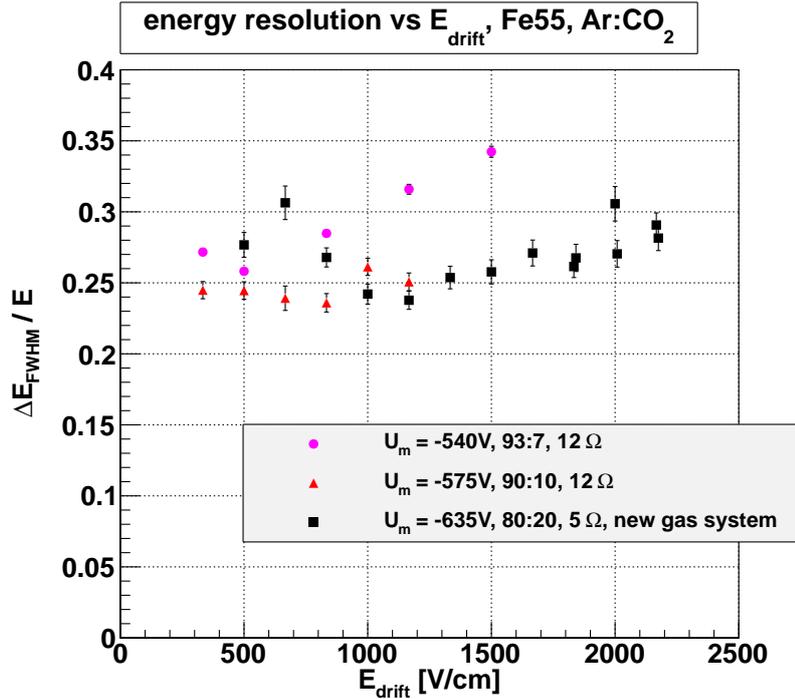
Figure 6.14: Energy resolution of the manganese 5.9 keV line as a function of the electric field in the drift region between cathode and mesh for three different mixtures of Ar:CO$_2$.

$$\frac{\Delta E_{\mathrm{FWHM}}}{E} = 0.24 = 2.355\sqrt{\frac{0.23}{224} + 0.097^2} \ . \tag{6.12}$$

A gain error is expected since a woven mesh, consisting of $18\,\mu m$ thick wires with $45\,\mu m$ pitch, is used. The electric field close to the wires, where, as has been shown in sec. 6.3, a considerable amount of charge is produced, is thus expected to be quite inhomogeneous. The energy resolution of Micromegas with electro formed meshes, exhibiting a much smaller thickness, is considerably smaller. Giomataris et al. [1996], using a $3\,\mu m$ thick mesh, reported an energy resolution of 14% FWHM. Micromegas produced in the micro bulk technology, achieve energy resolutions of 11% with a $5\,\mu m$ thick mesh [Dafni et al., 2009].

The energy resolution shows a typical behavior for all gas mixtures under variation of the drift field: Starting at low field values, the resolution decreases to a value of 0.23 to 0.24 with increasing drift field. A further increase of the drift field is accompanied by a reincrease of the resolution. This behavior can be understood, when comparing the drift fields E_{drift}, corresponding to minimum energy resolution ($E_{\mathrm{drift}} = 500\,\mathrm{V/cm}$, $800\,\mathrm{V/cm}$ and $1200\,\mathrm{V/cm}$ for 93:7, 90:10 and 80:20 respectively), to the drift fields, corresponding to maximum pulse height in fig. 6.6. It was already mentioned in sec. 6.1 that the pulse height is maximal, when the mesh's electron transparency is close to 1.0 and the attachment to electro negative impurities is low. If the drift field is too low, charge from ionization is lost due to attachment and recombination. For high drift fields, charges can not reach the amplification region, since they are caught by the mesh. Both effects influence the number of electrons, reaching the gas amplification region.

Again, looking at Ar:CO$_2$ 80:20, the pulse height decreases by 20%, when the drift field increases from $E_{\mathrm{drift}} = 1200\,\mathrm{V/cm}$ to $2200\,\mathrm{V/cm}$ (fig. 6.6). It is safe to assume, that the number of electrons reaching the amplification region, decreases by 20%, too, from 224 to 179. The energy resolution, on the other hand increases from 0.24 to 0.285 ± 0.015.
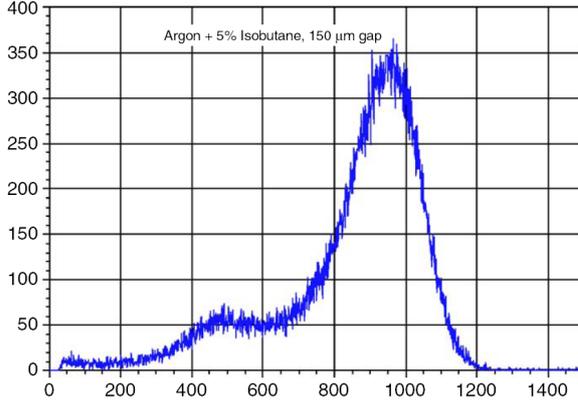
Figure 6.15: ^{55}Fe spectrum, measured in a bulk Micromegas with 150 μm amplification gap, taken from [Giomataris et al., 2006]. $\Delta E_{FWHM}/E = 0.25 \pm 0.1$, determined at the dominant 5.9 keV line.
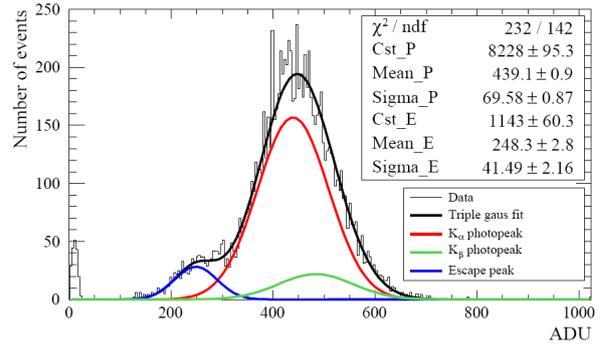
Figure 6.16: ^{55}Fe spectrum, measured in a bulk Micromegas with 128 μm amplification gap, taken from [Espargilière et al., 2009]. $\Delta E_{FWHM}/E = 0.37 \pm 0.1$, calculated from the displayed K_α line's standard deviation and mean.

The decrease of the mesh's electron transparency t, defined as

$$t = \frac{n_{\text{ion}} - n_{\text{lost}}}{n_{\text{ion}}} \; , \tag{6.13}$$

where $n_{\text{ion}} = 224$ is the number of electrons, created in ionization and $n_{\text{lost}} = 224 - 179 = 45$ is the number of electrons, lost due to low transparency, can only account for a portion of the energy resolution's increase. Applying Gaussian error propagation to eq. (6.13) and assuming poisson statistics i.e. $\Delta(n_{\text{ion}} - n_{\text{lost}}) = \sqrt{n_{\text{ion}} - n_{\text{lost}}}$ and $\Delta(n_{\text{lost}}) = \sqrt{n_{\text{lost}}}$, the transparency's relative error is

$$\frac{\Delta t}{t} = \sqrt{\frac{t(1-t)}{n_{\text{ion}}}} \cdot \frac{1}{t} \; . \tag{6.14}$$

Introducing this as an additional summand to eq. (6.9):

$$\frac{\Delta E_{\text{FWHM}}}{E} = 2.355 \sqrt{\frac{0.23}{224} + 0.097^2 + \frac{0.8 \cdot 0.2}{224} \cdot \frac{1}{0.8^2}} = 0.253 \; . \tag{6.15}$$

It is furthermore plausible to assume, that the electron transparency might show local inhomogeneities in the same manner as the gas gain, due to inhomogeneities of the electric field in the mesh region (sec. 6.3). This is not considered in eq. (6.14). Additionally, an increase of the voltage on the cathode may lead to an increase of the noise on the mesh and on the anode strips, due to the cathode's voltage's residual ripple. These two additional contributions might explain the discrepancy between the expected energy resolution of 0.253 and the measured of (0.285 ± 0.015).

This more qualitative estimation, makes the energy resolution's behavior as a function of the drift field at least plausible.

Fig. 6.17 displays the energy resolution as a function of the amplification field E_{amp} between mesh and anode. $\Delta E/E$ decreases, starting at lower field values, with increasing amplification field. After passing a minimum, it increases again. The initial decrease is due to a growth of the gas gain and thus a reduction of its relative error. As the amplification field increases, the
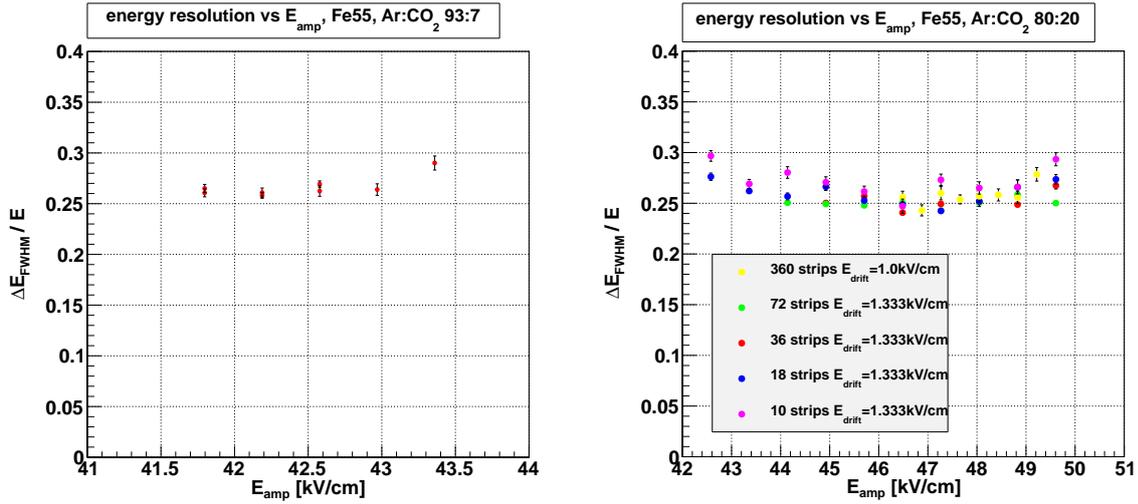
Figure 6.17: Energy resolution as a function of the amplification field E_{amp} for $Ar:CO_2$ 93:7(left) and 80:20(right). In the right graph, several data points acquired when reading out different groups of strips, are superimposed. It should be noted, that the energy resolution remains unaffected by the increase of the pulse height by a factor of 5 between measurements with 360 and 10 strips.

electron transparency decreases and the noise on the anode increases, causing the additional error, described above. This error seems to outweigh the rising gas gain's positive influence at high E_{amp} values.

Chapter 7

Strip Readout Performance

The results acquired with the Gassiplex based strip readout are presented in this chapter. Except for those discussed in sec. 7.1, all measurements were performed with frontend modules in the Micromegas resistor configuration (see sec. 5.3.3 for explanation). As soon as more than one Micromegas is involved, the frontend boards were capacitively coupled to the strips.

7.1 Frontend Board Performance in HERMES configuration

A first negative signal version of the Gassiplex frontend modules, denoted with HERMES configuration of resistors in sec. 5.3.3, was tested. The results and problems encountered are summarized in this section. It will be shown in the following sections, that this configuration is not suitable for readout of Micromegas, since the multiplexing amplifier on the frontend boards (sec. 5.3.1) is operated in saturation. The solution to this issue has already been discussed in the section about frontend adaptation (sec. 5.3).

7.1.1 Efficiency for Muons

The efficiency with respect to muons with HERMES type frontend boards has been determined in the physical setup described in sec. 4.2. The readout electronics was the Gassiplex HERMES configuration described in sec. 5.4. As a consequence, the geometrical correction factor of 0.881, accounting for the fact, that the trigger scintillators cover an area, larger than the Micromegas sensitive area (see sec. 4.4), remains valid. Unlike before, the uncorrected efficiency $\varepsilon_{\mathrm{uncor}}$ is deduced directly from the data. The number of strips hit in an event, is histogrammed (fig. 7.1).

This quantity also gives an idea of the cluster size. To calculate $\varepsilon_{\mathrm{uncor}}$, the number of events, in which the Micromegas registered hits on one or more strips, is divided by the total number of events. The real efficiency is then

$$\varepsilon = \frac{\mathrm{entries}_{\mathrm{bins}>0}}{\mathrm{entries}_{\mathrm{bins}\geq0} \cdot f_{\mathrm{geom}}} \ . \tag{7.1}$$

Efficiencies measured at two different amplification fields are displayed in fig. 7.2. Although the values grow for higher amplification field, they do not reach the expected range > 0.95. The strong fluctuations, observed in the efficiency at higher amplification field, suggest a considerable non-linearity in the signal amplification on the frontend board, assuming as before, that the efficiency is limited by pulse height.
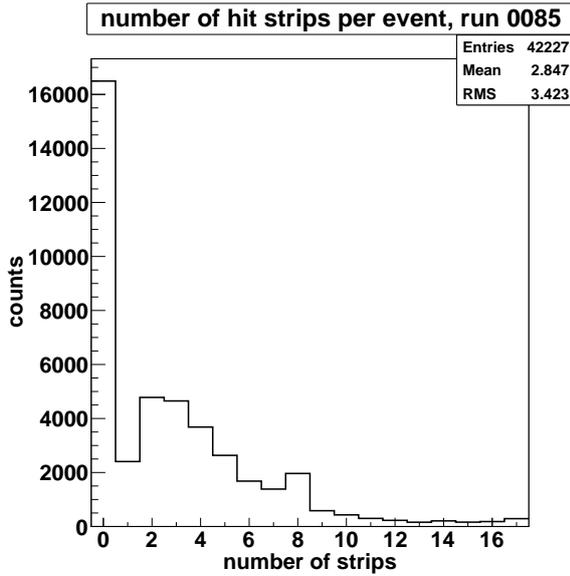
Figure 7.1: Number of strips hit per event, cosmics, read out with frontend boards in HERMES configuration.
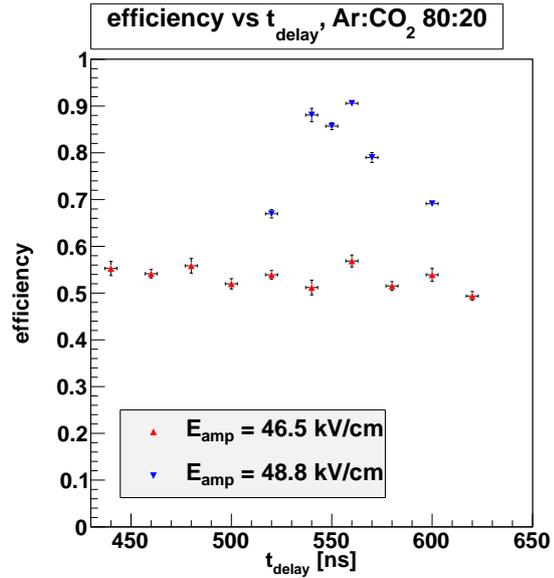

Figure 7.2: Efficiency to cosmics as a function of the time between particle passage and trigger signal t_{delay} for two different amplification fields.

That non-linearity is indeed observed in the pulse height spectra, discussed in the following section.

7.1.2 Pulse Height Spectrum

A pulse height spectrum for cosmics, measured with frontend modules in the HERMES configuration is displayed in fig. 7.3. As already discussed in sec. 2.1 and shown in fig. 6.4, a Landau like distribution is expected. The pulse height corresponds to the total charge in an event as described in sec. 5.5.

The cosmic spectrum, resulting from 42227 triggers, shows a large peak at small amplitudes and a smaller but wider peak centered around a pulse height of 350 ADC channels. To be able to exclude, that the peak at small values is due to an insufficient discrimination of background and noise, a background measurement at the same gas and electric field parameters was conducted. The readout was triggered 10000 times by a random trigger source, resulting in 38 fake events. After appropriate scaling, the readout acquired 160 fake events per 42227 triggers. This value is definitely too small to account for the observed peak.

It is likely to assume, that the bulk of recorded events are indeed muon signals, although the pulse height is massively distorted. As the multiplexing amplifiers on all frontend boards are operated in saturation, the observed behavior is understandable. Very large signals with a total charge larger than 400 ADC channels are probably measured correctly. In the intermediate range, between 10 and 400 ADC channels though, the multiplexing amplifiers show an extremely non-linear behavior.

Pulse height spectra, acquired with the correctly adapted Gassiplex readout and frontend modules in the Micromegas configuration are displayed in fig.7.12 and show the expected asymmetric Landau like distribution at high efficiency.
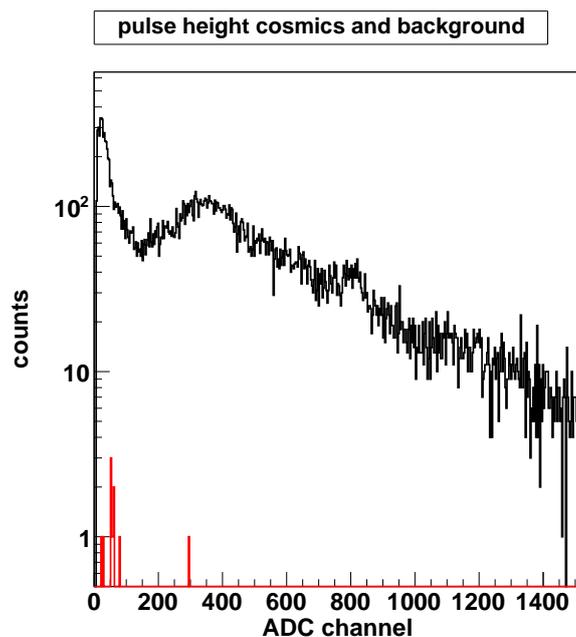
Figure 7.3: Pulse height spectrum for cosmics, triggered by two coincident scintillators (black) and a spectrum acquired with a random trigger (red). The cosmic spectrum is formed by 25733 events, resulting from 42227 triggers with a trigger rate of ≈ 0.6 Hz. The background spectrum was acquired with 10000 random triggers at a count rate of ≈ 1 Hz and resulted in 38 "events".

7.1.3 Channel Crosstalk

A considerable crosstalk is observed when studying the Micromegas, read out by Gassiplex frontends in the HERMES configuration[1] (fig. 7.4).
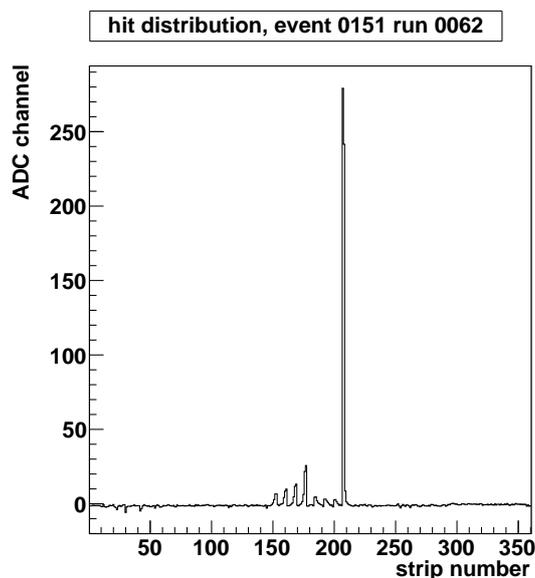

Figure 7.4: ADC value on each strip in an ^{55}Fe event. A crosstalk within the FE incorporating the hit strips is clearly visible. The apparent periodicity visible in this plot is, due to the routing of the channels, more or less accidental.

---

[1]tab. 5.1 on p. 33.

There seems to be a periodicity between the strips with elevated amplitude but there is no physical explanation for a crosstalk, as observed, within the detector. The picture starts to become clear, when looking at the charge, seen by each frontend channel i.e. looking at the unmapped frontend output (fig. 7.5).
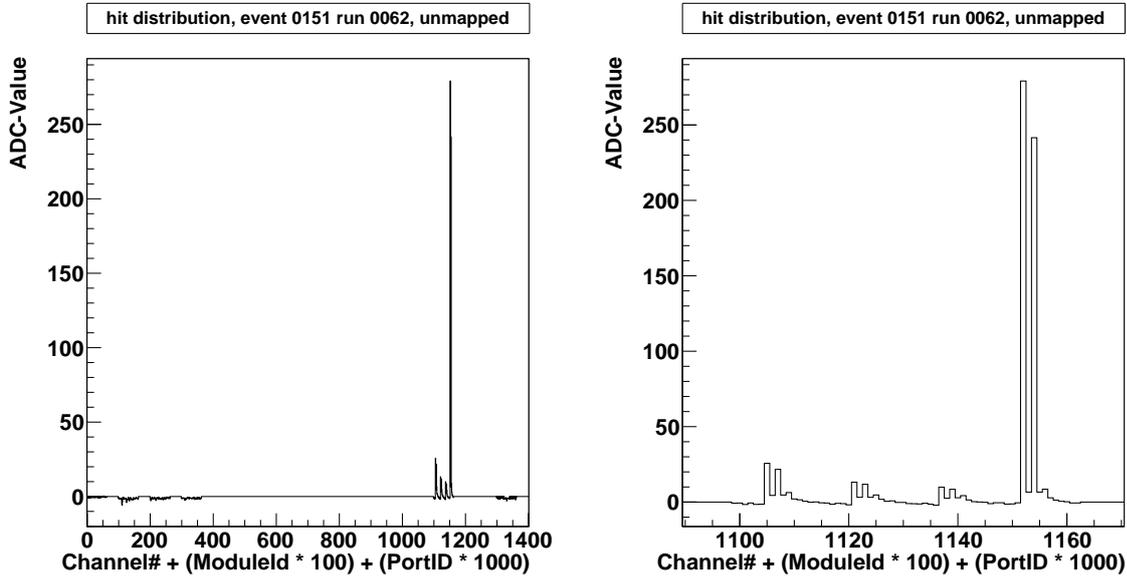

Figure 7.5: ADC value corresponding to the charge seen by each input channel. A distinct ≈ 16 fold periodicity is now visible.

A distinct 4 fold periodicity is visible, with ≈ 16 channel spacing, which points at a crosstalk on the frontend since the Gassiplex chips have 16 channels each. It will be shown that crosstalk is created within the multiplexed input video amplifier EL4141. Tab. 7.1 gives the temporal order, in which the frontend channels are "read" by the multiplexing amplifier and then digitized. Two naming conventions must not be confused: each Gassiplex' channel is denoted with a channel number 0 to 15. The frontend channels though, are numbered from 0 to 63. The mapping is given in tab. 7.1. In the following, I will always stick to the latter naming convention.

When detecting a hit on channel n, it is advantageous to check, which channels, excluding the channels corresponding to the 8 neighboring strips of the hit strip, also detect a hit. As already stated in sec. 5.5, a strip has been hit, when its ADC value is bigger than 3σ. Fig. 7.6 displays the additionally "hit" channels for real hits on two different channels, namely channel 18 of frontend 1 and channel 41 of frontend 4 in a run with $\approx 40k$ muon triggers.

When channel 18 is hit, the channels 34, 50, 3, 19, 35 and 51 often have a significantly increased ADC value, too. A glance at the temporal order (tab. 7.1), in which the frontend channels are multiplexed, reveals the strong correlation: those six to ten channels, that are fed through the multiplexing amplifier after a channel with elevated ADC value show, quite likely, also an elevated value. The same holds for the displayed channel 41 of frontend 4.

This internal crosstalk can be caused by two different effects: First, the video amplifier itself gives rise to an irreducible influence of signals at the unselected inputs onto the output. Upon the ith falling edge of CLK_TTL after the trigger, the four Gassiplex chips feed the amplified signal from channel $i - 1$ to their output[2]. The Gassiplex output signals remain at their value for a whole clock cycle of CLK_TTL while the video amplifier multiplexes them into the ADC. The feedthrough attenuation from unselected inputs to the output is about

---

[2]Gassiplex channels from 0 to 15.

−60 dB [Elantec, 1994] so should be negligible in the present case. Furthermore, this would not explain the strong temporal correlation between channels with elevated ADC value.

Gassiplex	Gassiplex channel #	frontend channel #
1	0	0
2	0	16
3	0	32
4	0	48
1	1	1
	...	
2	2	18
3	2	34
4	2	50
1	3	3
2	3	19
3	3	35
	...	
3	9	41
4	9	57
1	10	10
2	10	26
3	10	42
4	10	58
	...	
1	15	15
2	15	31
3	15	47
4	15	63

Table 7.1: *Temporal sequence of channels in the multiplexing amplifier [Böhmer, 1999]. Only the ones necessary for this discussion are displayed.*
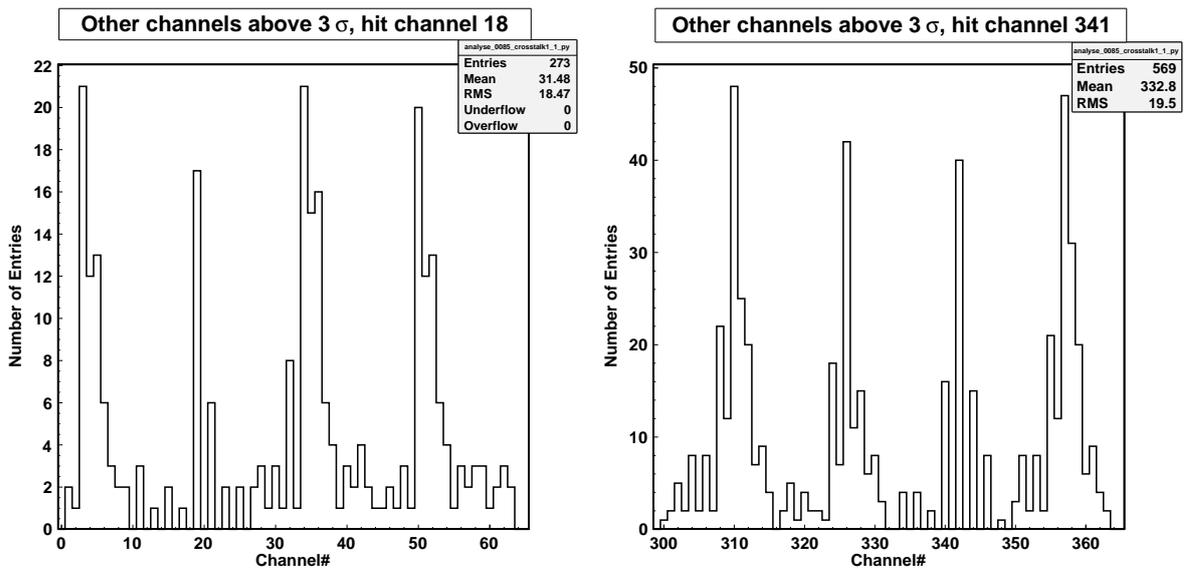

Figure 7.6: *The histograms show, which other strips also detected a "hit", when a real hit was seen on channel 18 on frontend module 1 or 41 on frontend 4.*

Actually the problems arise from the fact, that the multiplexing amplifier operates in saturation in the HERMES configuration (see sec. 5.3.3). A strong signal can pull the baseline to lower values and out of saturation, but as soon as this high pulse at the input is gone, the amplifier baseline drifts back up. This relatively slow transient behavior can be seen on the following channels as an elevated ADC value. It is necessary to mention that the baseline of the multiplexing amplifier is at a high value around 2.5 V to 3.3 V, signals have lower values. In the subsequent software analysis, the baseline is drawn to zero and signals are inverted, which results in the shown representation of an event (fig. 7.4).

In the following, measurements acquired with frontend modules in the Micromegas configuration are discussed. It will be shown, that the crosstalk is gone (sec. 7.3), high efficiency of up to 99% can be achieved and that the pulse height spectra exhibit the expected shape (sec. 7.4).

7.2   Hit Distribution in two Micromegas

In measurements with cosmic muons in the setup with two Micromegas (sec. 5.4.1), some 100k events were acquired. The Gassiplex frontend modules in the Micromegas configuration were capacitively coupled to the strips and additional grounding was used to divert discharges more quickly to ground. Stable operation over several days was possible, not a single crash was observed.
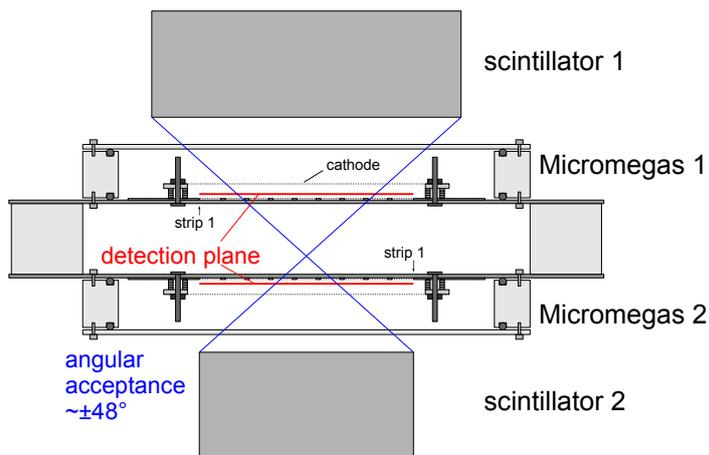

Figure 7.7: Lateral cut through the setup with two Micromegas. The virtual position of the strips, denoted with detection plane, is extracted from measurements with three Micromegas. Tracks with a maximum angle of around 48° to the vertical axis are accepted. The position of strip 1 is indicated for both detectors.

In the analysis, the hits in each detector are determined, by first finding the strip with the largest ADC value bigger than 3σ and then calculating the charge weighted hit-position by including the surrounding strips. Interesting informations about the angular distribution of cosmics and about the Micromegas' homogeneity can be gathered by histogramming the number of events in which certain strips are found to be the one with maximum ADC value.

To be able to compare this hit distribution on strips to the expectation, the Monte Carlo simulation, described in sec. 4.4, originally intended for determining the geometric correction factor for efficiency measurement, was modified. Apart from including a second Micromegas and adjusting the geometric dimensions, several minor changes were performed. The hit-positions of muons in the lower scintillator, which are the start points of the simulation, are

now randomly and uniformly distributed. Tracks of muons with an angular distribution of $f(\theta) \propto \cos^2(\theta)$ and $g(\varphi) = $ const. are simulated. If the muons hit both scintillators and both Micromegas, the track information, as inclination and intersections in sensitive planes of all detectors is histogrammed.

Fig. 7.7 shows a cut through the setup, looking from the readout side to the high voltage side. The position of strip 1 is indicated for both detectors. The angular acceptance, limited by the scintillators' dimensions, is indicated by two blue lines. Since the drift gap is 6 mm wide, non-perpendicular tracks would not be reconstructed correctly, if the strip position, assumed in the analysis, would coincide with the real strips' position. A virtual strip position is extracted from measurements with three Micromegas. The detection plane is shifted towards the cathode and situated almost halfway between mesh and cathode. The shift is not expected to show any dependence on track inclination.
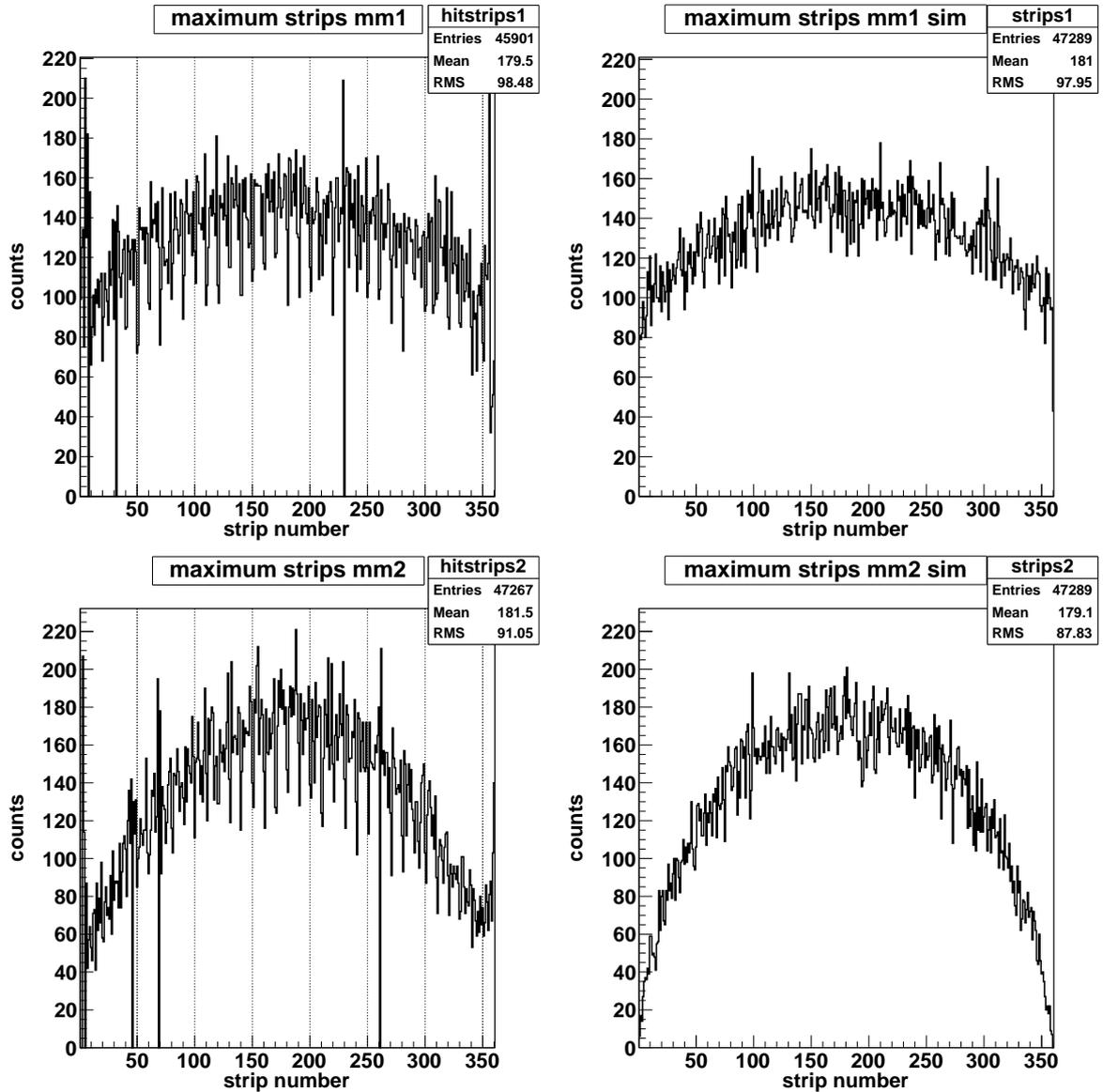

Figure 7.8: Hits per strip, for both Micromegas. The shown hit-positions, other than in the following discussion, are not the usual charge weighted hit-positions, but are defined by the strip with maximum pulse height. The shape of the measured distributions (left) and the simulated ones (right) are quite similar. The regular dips every 10 strips in the measured hit distributions are due to the mesh-supporting pillars, covering up to 13.2% of each tenth strip.

A comparison between data and simulation of the distribution of maximum ADC value over strips is shown in fig. 7.8 for both Micromegas. A good agreement is visible. Three dead channels are visible in Micromegas one and 6 in Micromegas two respectively. This has not yet been investigated, most likely it is due to bad solder contacts on the routing board.

An interesting feature are the periodic dips in both spectra, where the number of counts is about 25% smaller than the mean value on the surrounding strips. They occur on every tenth strip and are caused by the mesh supporting pillars. These are arranged in a periodic manner every 2.5 mm and thus every tenth strip is covered by 40 pillars, since the strip pitch is 250 µm. In the worst case 13.2% of these strips' area is covered by insensitive material. The pillars affect a region, considerably larger than their diameter of 300 µm, since the effect can be usually seen on two neighboring strips. It should be investigated, if this negative effect can be reduced in a detector with a thinner mesh but wider spaced pillars, without any loss in energy resolution.

7.3 Crosstalk

Massive crosstalk, a major problem of the HERMES type frontends (see fig. 7.4), is no longer present in the Micromegas configuration. Typical muon events as in fig. 7.9 show no crosstalk.
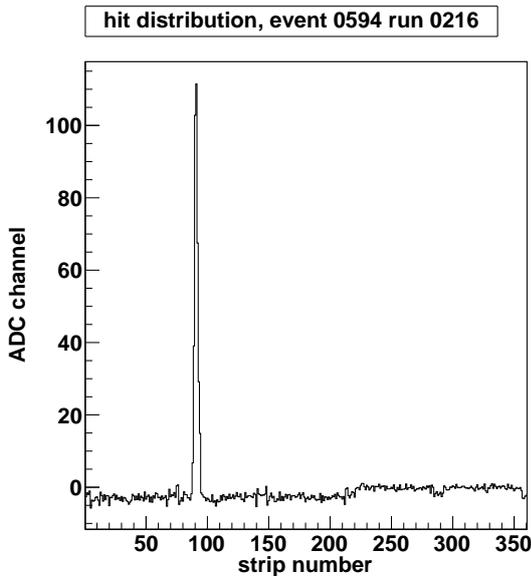

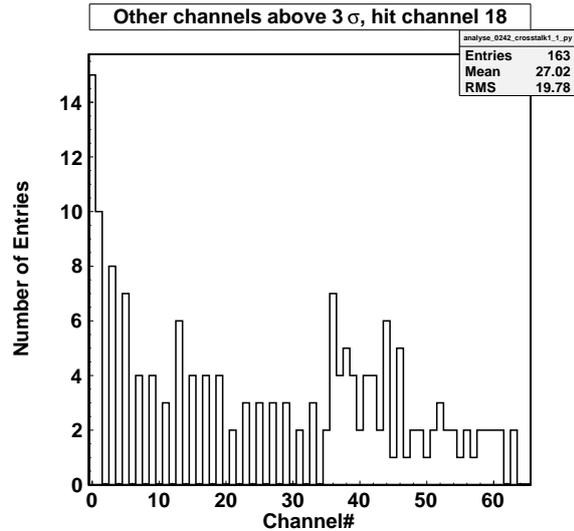Figure 7.9: Typical cosmic event in Micromegas one. No crosstalk is visible.

Figure 7.10: Other strips with ADC value $> 3\sigma$ when a real hit on channel 18 is detected. Only uncorrelated additional hits are visible.

Similar to fig. 7.6, additional elevated strips outside the expected strip region are shown for a run with $45k$ triggers in fig. 7.10. Although some uncorrelated elevation of strips is visible, the elevated strip's amplitude is in general very small. As will be shown in sec. 7.6 some additional real hits are expected, leading to the observed behavior.

7.4 Efficiency

The efficiency for muons is derived directly from the data, as described in sec. 7.1.1. Dividing the number of events with a registered hit by the total number of events times a geometrical

correction factor gives the real efficiency according to eq. (7.1). Since the efficiencies described below are derived from the setup with two Micromegas (see sec. 5.4.1), new geometrical correction factors have to be calculated for both detectors. This is achieved by modifying the Monte Carlo simulation, treated in sec. 4.4. By variation of geometric dimensions, mean factors are calculated: $f_{geom,mm2} = 0.878$ and $f_{geom,mm1} = 0.867$. Their error is expected to be smaller than 0.5%.

The efficiency for muons is displayed in fig. 7.11 for both detectors, running with Ar:CO$_2$ 93:7 at NTP, as a function of the amplification field between mesh and anode.
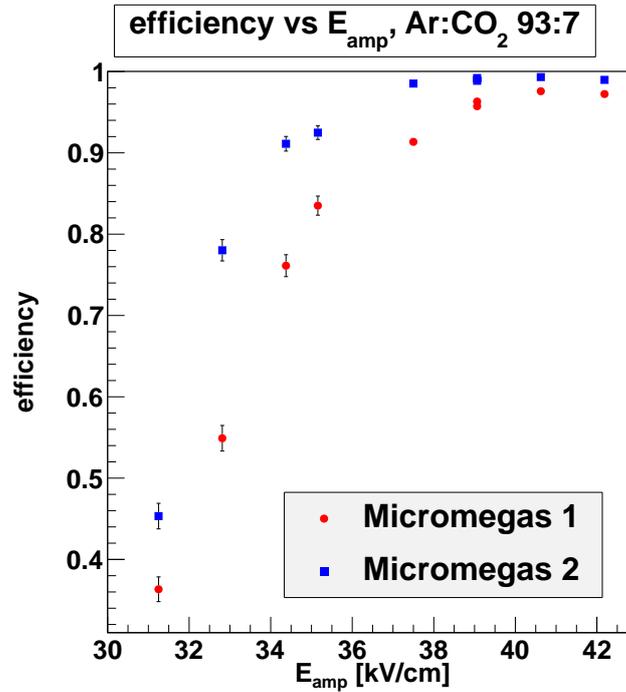

Figure 7.11: *Efficiency with respect to cosmics for two Micromegas as a function of the amplification field E_{amp}. The data points below $E_{amp} < 36\,kV/cm$ correspond to measurements with direct coupling of strips and frontend modules. In this configuration, no long term stable operation is possible. The values above $E_{amp} > 36\,kV/cm$ were acquired with capacitively coupled readout electronics.*

The data points below $E_{amp} < 36\,\mathrm{kV/cm}$ are just added for completeness. There, the Gassiplex readout was not capacitively coupled to the strips, so that no stable operation was possible. With capacitively coupled readout electronics, Micromegas two and Micromegas one reach $\varepsilon > 0.98$ and $\varepsilon > 0.97$ respectively, for amplification fields $E_{amp} = 41.5\,\mathrm{kV/cm}$. Using the single preamplifier readout, the highest efficiency measured with Ar:CO$_2$ 93:7 was $\varepsilon = 0.90$ for $E_{amp} = 43.4\,\mathrm{kV/cm}$. The reason for the considerably better performance with the Gassiplex readout is twofold: first, the charge signals are intrinsically higher, since the readout structure's capacity is smaller by a factor of 360 (see chap. 8 for explanation). Second, the Gassiplex charge-to-voltage conversion factor is with $10.3\,\mathrm{V/pC}$ [Beusch et al., 1994], larger by a factor of 10 than the Canberra 2004 preamplifier's, used in single plane readout. Since the noise, picked up by a single strip, is much smaller compared to single plane readout with 360 connected strip, the use of a preamplifier with such a high gain factor is possible.

The pulse height in Micromegas one is always by about 26% smaller than in Micromegas two as can be seen in fig. 7.12. This leads to a slightly smaller efficiency in Micromegas one and is partly determined by the larger 7 mm drift gap of Micromegas two, as compared to 6 mm. Since the charge, produced in ionization, scales linearly with the drift gap and
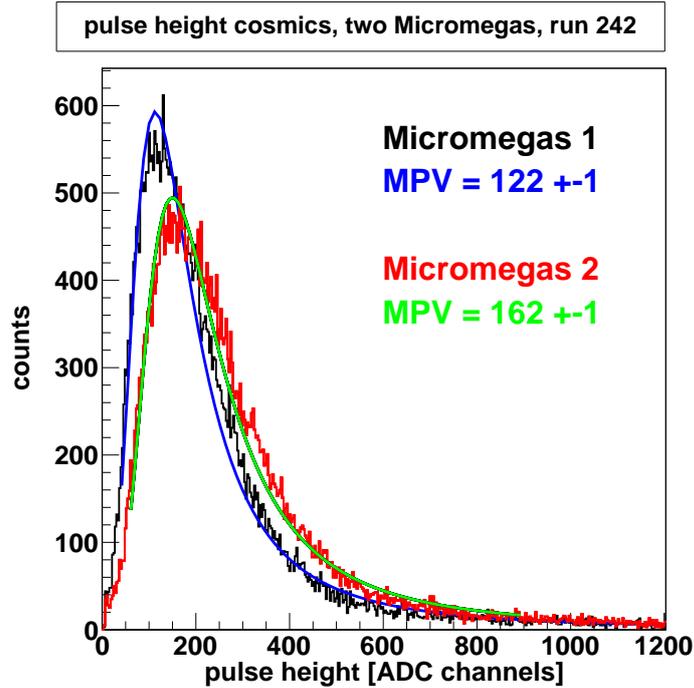
Figure 7.12: Pulse height spectra for a cosmics run with two Micromegas. The most probable pulse height, derived from a Landau fit, is displayed.

the observed pulse height is directly proportional to this charge, only a difference of 14% would be expected. There are two further possibilities for the observed deviation: First, the gas passes with 1 ln/h through the detectors. Since they are connected in a serial manner, the gas in Micromegas two will contain less impurities since it is the first in the chain. As they are operated with ≈ 30 mbar over pressure though, no massive contamination with air and especially oxygen is expected. Second, the amplification gaps might slightly differ. A deviation of around 5 µm would account for the observed difference. As already discussed in sec. 6.2, the pulse height spectra exhibit the expected asymmetric shape, that is Landau like, but not a true Landau distribution (see also sec. 2.1).

7.5   Alignment of three Micromegas

The setup with three Micromegas, introduced in sec. 5.4.2, can be used to determine the single detector spatial resolution and to align the detectors. As already described in sec. 5.5, tracks are reconstructed by fitting a line to the three hit-positions in three detectors. They are expressed in millimeters on the x-axis. Fig. 7.13 clarifies the track reconstruction process. A line is fit to the primary hits in all detectors (dash-dotted line). A $\chi^2 > 10$ is assumed to identify a fit with insufficient quality, enabling a search for alternative hits in all detectors. If alternative hits on strips, excluding the 40 around the primary hit, are found, a second line is fit to all possible permutations. If the alternative track's (continuous line) χ^2 is smaller than the original track's, the alternative is considered for the subsequent analysis.

Residuals Δx between the predicted hit (blue circle) and the measured hit (black or yellow circle) are calculated for each detector:

$$\Delta x = x_{\mathrm{pred}} - x_{\mathrm{meas}} \; . \tag{7.2}$$

When fitting a line to the unweighted data points, the larger distance of Micromegas three to the others results in an extremely small residual in this detectors at the cost of enlarging the residual in Micromegas one and two. To prevents this, a fit is performed with weighted hit positions using the ROOT class TGraphErrors[3], in order to get similar residuals in all detectors.
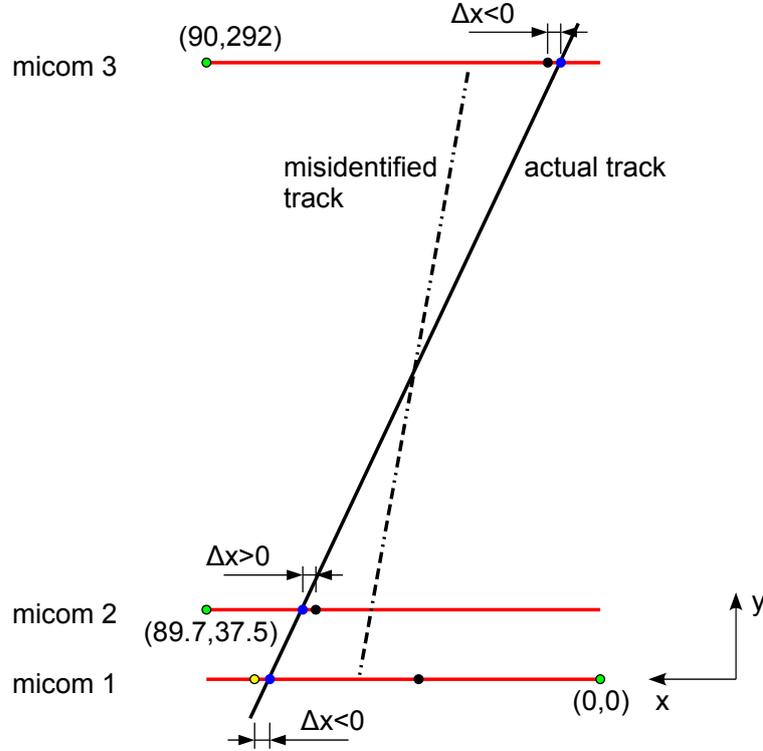

Figure 7.13: *Track reconstruction in three Micromegas. The red lines are the detection planes. The position of strip 1 is marked with a green circle, defining the relative alignment. Micromegas one's strip 1 defines the origin of the two dimensional coordinate system. The y distances are not drawn to scale. The black circles represent the primary hits, taken for the first fit of the dash-dotted line. The yellow point represents the alternative hit in Micromegas one. The fit including this point (black solid line) shows a strongly reduced χ^2. The real track's intersection points with the detection planes are marked with blue circles. Residuals Δx are given by the difference of the predicted (blue circle) and the measured hit (black/yellow circle). The angle enclosed by a track and the y-axis defines the track inclination as tracking is purely two dimensional.*

A track's inclination ϑ is defined by the angle enclosed by the track and the y-axis

$$\vartheta = \arctan\left(\frac{\mathrm{d}x}{\mathrm{d}y}\right) \ , \tag{7.3}$$

where $\mathrm{d}y/\mathrm{d}x$ is the track's slope, derived from the fit. Thus positive as well as negative inclinations are possible. It should be noted, that ϑ describes the inclination in the two dimensional coordinate system (x, y). If the projection of a real track onto the strip plane is parallel to the strips, the track is measured as perpendicular, even though it may be inclined. This has to be taken into account, when investigating the measured track inclination. I will come back to this in sec. 7.7.

---

[3]http://root.cern.ch/root/html526/TGraphErrors.html

Mutual detector alignment can be achieved by examining the residual as a function of the track inclination. A shift in one detector influences the residual in all detectors. A shift is defined as the difference between the assumed position in the analysis algorithm and the true position. Fig. 7.14 demonstrates the underlying idea. The assumed position of Micromegas two is shifted in negative x- and positive y-direction.
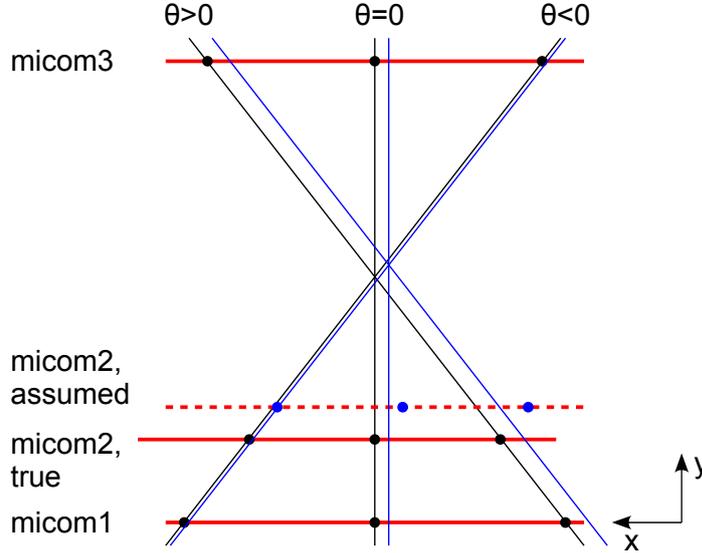

Figure 7.14: Effect of a shift of the assumed position of Micromegas two in positive y- and in negative x-direction. The detectors' true sensitive planes are represented by thick red lines, the dashed red line corresponds to Micromegas two's shifted plane. True hit positions and tracks are marked by black circles and lines, respectively. The tracks, reconstructed on the basis of Micromegas two's wrong position are represented by blue lines. The blue circles indicate the shifted hit-positions in Micromegas two.

The effects on the residual depend on the track's inclination and can thus be used to identify the shift. The resulting residual's dependency on the inclination is shown in the following tab. 7.2.

	$\vartheta < 0$	$\vartheta = 0$	$\vartheta > 0$
Micromegas one	$\Delta x \lesssim 0$	$\Delta x < 0$	$\Delta x \ll 0$
Micromegas two	$\Delta x \gtrsim 0$	$\Delta x > 0$	$\Delta x \gg 0$
Micromegas three	$\Delta x \lesssim 0$	$\Delta x < 0$	$\Delta x \ll 0$

Table 7.2: Correlation between residuals and inclination, caused by the shift of Micromegas two, described in fig. 7.14. The binary relations are meant to describe trends, they are not to be understood in a strict mathematical way.

Other shifts can be analyzed in the same manner. Usually, more than one shift is present. To correctly align the detectors, a few iterations of corrections are necessary.

In fig. 7.15 the residual as a function of the inclination is displayed for a shift of $(-0.5\,\text{mm}, 1.0\,\text{mm})$ of Micromegas two. The discussed effects are clearly visible, such that, even with the low statistic acquired in the lab, alignment at the level of several micrometers is possible. For correctly aligned detectors, these distributions are flat and centered around $\Delta x = 0$.
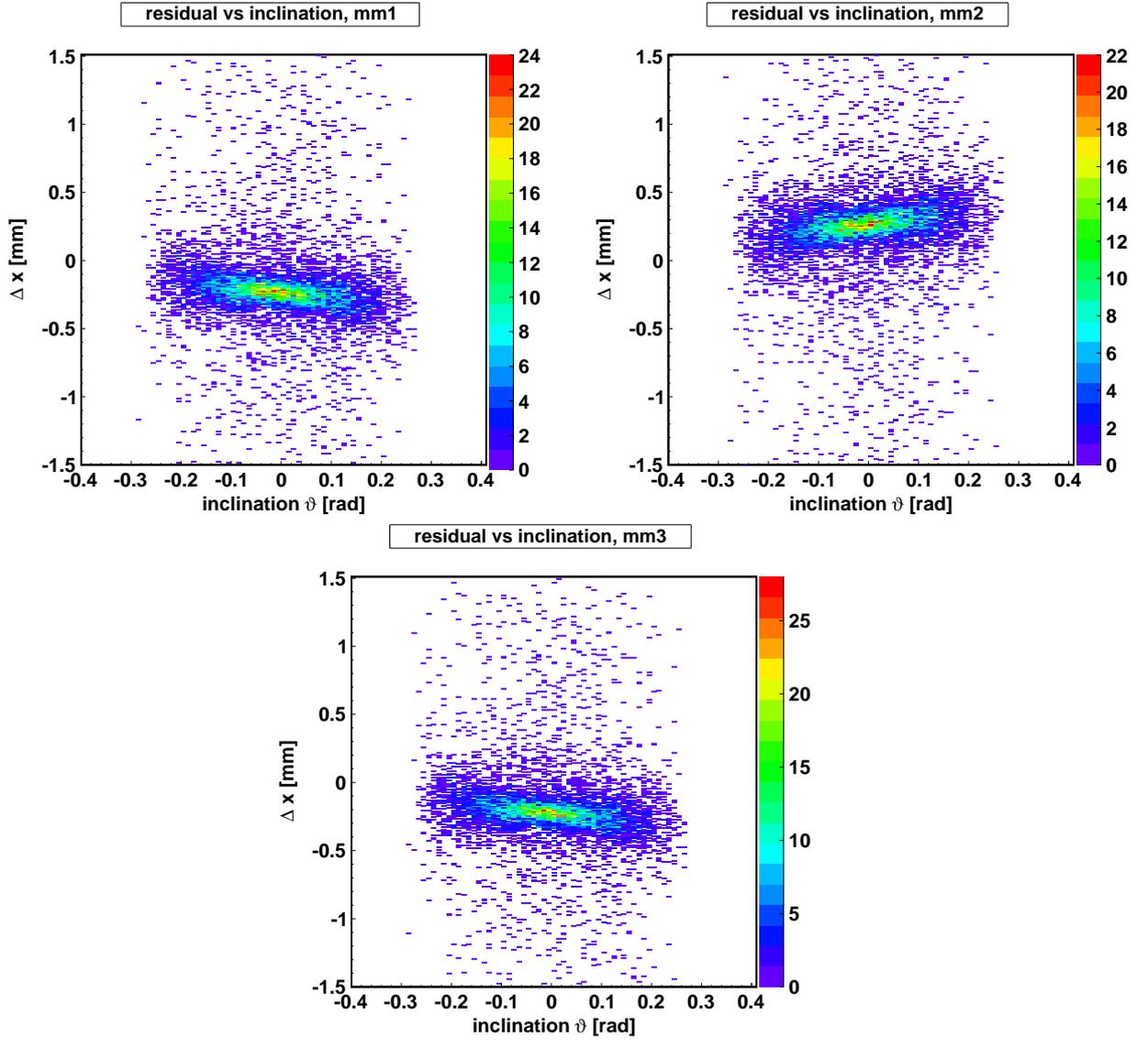
Figure 7.15: Residual $\Delta x = x_{pred} - x_{meas}$ in all three detectors as a function of the track inclination ϑ. The displayed situation results from a shift $(x = -0.5\,mm, y = 1.0\,mm)$ of Micromegas two's assumed position compared to the true position.

7.6   Spatial Resolution

The method of residual calculation, described in the previous section, can also be used to determine the single detector spatial resolution. Single detector residuals are accessible by projecting the two dimensional histograms, describing the residual Δx as a function of the inclination ϑ, onto the y-axis. A sharp peak at $\Delta x = 0$ (fig. 7.16) is fit with a sum of two Gaussians with different standard deviation $\sigma_1 < \sigma_2$:

$$f(x) = f_1(x) + f_2(x) = a_1 e^{-0.5\left(\frac{x-\mu_1}{\sigma_1}\right)^2} + a_2 e^{-0.5\left(\frac{x-\mu_2}{\sigma_2}\right)^2} . \tag{7.4}$$

a_1 and a_2 are the amplitudes of both Gaussians. The mean values of both Gaussians should coincide $\mu_1 = \mu_2$. The production of delta electrons, resulting in a badly defined muon hit-position, is, among others, a physical explanation for the occurrence of events with a

larger residual, forming the second Gaussian. As long as $\int f_1(x)\mathrm{d}x > \int f_2(x)\mathrm{d}x$, this ansatz is legitimate and no distorting effect on the measured spatial resolution is expected. The spatial resolution of the detector, limited by multiple scattering, is given by σ_1.
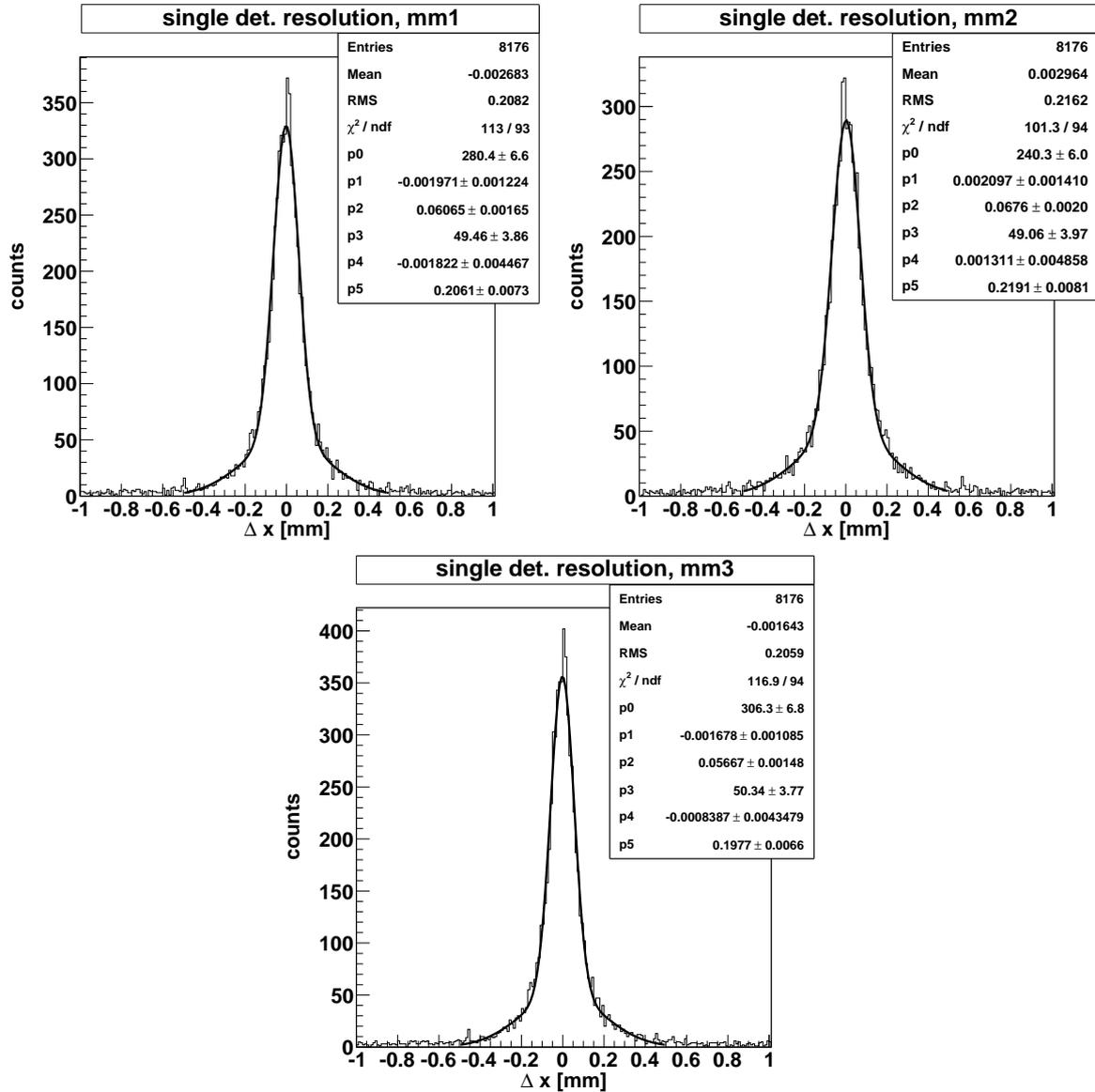

Figure 7.16: Single detector residuals in all three Micromegas, determined from 8176 muon tracks. All possible track inclinations are considered.

Fig. 7.16 shows the single detector residuals for three Micromegas. Apart from the sharp peak, events with considerably larger residual of up to 10 mm are measured. They result from completely misidentified tracks, either due to an imperfect analysis algorithm or due to scattering in the detector's aluminum lid. As already described in sec. 5.5, the algorithm searches for one alternative hit in each detector, if the fit's $\chi^2 > 10$. The 40 strips around the primary hit are excluded in this search. Since the strip with the largest ADC value among the 320 alternative strips, defines coarsely the alternative hit position, misidentification of alternative hits is possible. A future refinement of the analysis algorithm, searching without constraints for several alternative hits, might considerably reduce the number of misidentified tracks. A hardening of the cosmic muon spectrum by including a lead or iron absorber between Micromegas three and the lower scintillator would reduce the multiple scattering considerably (see eq. (7.6)).

Nevertheless, an estimation of the spatial resolution is possible. The single detector residuals were fit with the function, described in eq. (7.4), in an interval $\Delta x \in [-0.5, 0.5]$. 84% of the tracks have residuals within this interval. 89% lie in the interval $[-1.0, 1.0]$. After setting correct start values, no constraints were put on the fit parameters. Spatial resolutions of $\sigma_{mm1} = (61 \pm 2)\,\mu m$, $\sigma_{mm2} = (68 \pm 2)\,\mu m$ and $\sigma_{mm3} = (57 \pm 2)\,\mu m$ are observed. The difference between the values is insignificant, since the weights in the track fit were chosen appropriately, to receive similar resolution in all detectors. A mean resolution of $(62 \pm 6)\,\mu m$ can thus be assumed.

Since a Gaussian's integral is given by

$$\int_{-\infty}^{\infty} a e^{-0.5\left(\frac{x-\mu}{\sigma}\right)^2} \mathrm{d}x = a\sigma\sqrt{2\pi} \ , \tag{7.5}$$

and $\int f_1(x)\mathrm{d}x = 42.6 > 25.6 = \int f_2(x)\mathrm{d}x$, the two Gaussians fit is justified. The spatial resolution shown is limited by several effects: Multiple scattering, production of δ-electrons, diffusion of electrons in the drift gap and inhomogeneities, resulting from non-perpendicular tracks. Quite interesting is the fact that Mlynek [2006] observed the same relation $\sigma_2/\sigma_1 = 3$, when fitting the residuals in monitored drift tubes.

In the following, the contribution of two effects will be treated in detail.

Charged particles like muons, traversing a material of thickness x are deflected under small angles, due to multiple Coulomb interactions with the material's atoms [K. Nakamura et al. (Particle Data Group), 2010]. The projected deflection angle distribution is in our case nearly Gaussian shaped with a width of

$$\theta_0 = \frac{13.6\,\mathrm{MeV}}{\beta^2 \gamma m c^2} z \sqrt{\frac{x}{X_0}} \left(1 + 0.038 \ln \frac{x}{X_0}\right) \ . \tag{7.6}$$

β, γ, m and z are the incident particle's velocity, Lorentz factor, mass and charge number. x is the width and X_0 the radiation length of the absorber material. Measurable multiple scattering can occur in the meshes and in the detector PCBs of Micromegas one and two and in the aluminum lids of Micromegas two and three. Because of the geometry and the large distance of the third Micromegas, the major contribution to the spatial resolution is given by scattering in Micromegas two's 2 mm thick aluminum lid. Assuming MIP like low energy muons with $\beta^2\gamma \approx 4$ and furthermore $m_\mu c^2 = 106\,\mathrm{MeV}$, $X_{0,\mathrm{Al}} = 24.01\,\mathrm{g/cm^2}$ and $\rho_{\mathrm{Al}} = 2.699\,\mathrm{g/cm^3}$, the angle distribution's width is

$$\theta_0 = \frac{13.6\,\mathrm{MeV}}{4 \cdot 106\,\mathrm{MeV}} \sqrt{\frac{0.540}{24.01}} \left(1 + 0.038 \ln \frac{0.540}{24.01}\right) = 4.117 \cdot 10^{-3} \ . \tag{7.7}$$

This leads to an uncertainty of

$$\Delta x_{rms} = \frac{1}{\sqrt{3}} 230\,\mathrm{mm} \cdot \theta_0 \approx 547\,\mu m \tag{7.8}$$

in the hit-position, measured in Micromegas three. Since the resolution is determined by fitting a line to all three points, an error in just one experimental hit will pose an error on the others, too. To determine its influence on the single detector resolutions in three Micromegas, a Monte Carlo simulation was used. Straight muon tracks in the three Micromegas system are simulated. The muon's position in the third Micromegas is then shifted by a randomly drawn error, following a Gauss distribution with standard deviation $\sigma = 547\,\mu m$. A line

fit is performed on the correctly weighted hit-positions and the residuals are calculated in the same manner as described above. Since no other errors are present, this allows for determining the multiple scattering's influence all by itself. By simulating 10000 muon tracks, one gets Gaussian shaped residual distributions for all Micromegas with standard deviations of $\sigma_{mm1} = 32\,\mu m$, $\sigma_{mm2} = 37\,\mu m$ and $\sigma_{mm3} = 30\,\mu m$, thus $\overline{\sigma_{mscat}} \approx 33\,\mu m$.

Cum grano salis, these results indicate, that multiple scattering of cosmic muons with $\beta^2\gamma \approx 4$ is adulterating the observed spatial resolution[4] by about $10\,\mu m$. Jeanneau et al. [2000] observed a resolution of $\sigma = 50 \pm 1.3\,\mu m$ in wedge shaped Micromegas with a strip width of $100\,\mu m$ and a pitch 210-250 μm in a $100\,GeV/c$ muon beam.

In particle beams with higher momentum, the resolution is expected to become notedly better. When using Micromegas in a tracking system for cosmic muons, as intended for neutron irradiation tests of muon monitored drift tubes, the aluminum lids should be replaced by Mylar or Kapton foil, to diminish the multiple scattering.
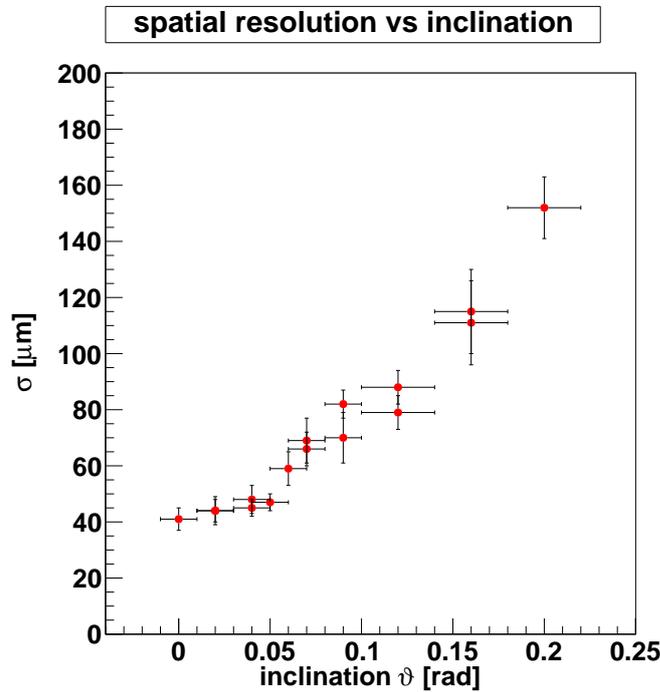

Figure 7.17: Spatial resolution as a function of the track inclination ϑ for Micromegas one.

For the investigation of the spatial resolution's dependence on the track inclination, data from Micromegas one are taken, since its total resolution is close to the average resolution. The spatial resolution for perpendicular tracks, i.e. tracks with $\vartheta = 0$, is on the order of $\sigma_{mm1,\vartheta=0} = (41 \pm 4)\,\mu m$ (fig. 7.17). For inclined tracks, the value increases to $\sigma_{mm1,\vartheta=0.2} = (152 \pm 11)\,\mu m$. This is most likely due to the fact, that the produced charge disperses on an increasing number of strips with increasing inclination, as can be seen in fig. 7.18. The number of strips hit in an event depends on the inclination ϑ and on the width w of the charge distribution, caused by diffusion and processes in gas amplification

$$\#strips = \sqrt{\left(\frac{d_{drift}}{0.25\,mm}\tan|\vartheta|\right)^2 + w^2}\,, \tag{7.9}$$

with $w \approx 3.9$ strips. It can be seen quite clearly from fig. 7.18 that the number of hit strips

---

[4]$\sigma_{true} = \sqrt{62^2 - 33^2}\,\mu m = 52\,\mu m$

does not increase as strongly with the inclination as expected. This is caused by two effects: First, the muons do not create a homogeneous line of charge in the drift gap but several clusters of charge, eventually leading to a smaller number of hit strips. Second, when the charge distributes inhomogeneously on several strips, the total amount of charge on some strips is too small to lead to a clearly detectable signal. These signals vanish in the noise.
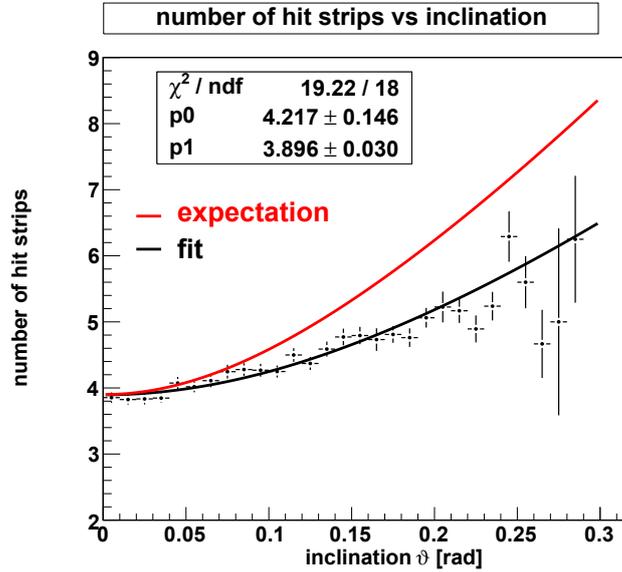

Figure 7.18: Number of strips, hit in an event, as a function of the inclination ϑ for Micromegas one.

Both effects have a strong influence on the reconstructed hit position, causing the observed increase of the spatial resolution for inclined tracks. A smaller drift gap might have a positive influence on the resolution of inclined tracks. An increased amplification field might also reduce the resolution's degradation under inclined tracks. This needs to be further investigated.

Diffusion as well as the spatial resolution with different gas mixtures and electric field parameters has not yet been investigated.

Nevertheless, it could be shown, that the Micromegas strip readout runs stably with an efficiency above 97% and track reconstruction with a single detector resolution of $(62 \pm 6)\,\mu m$ is possible. Thus the Micromegas can provide an external track reference for tests of muon monitored drift tubes.

7.7 Inclination Spectra of Muon Tracks

The distribution of muon tracks' inclination, measured with the three Micromegas setup, is determined by the angular distribution of cosmics and the setup's geometrical acceptance. To be able to compare the measurements with the expectation, the Monte Carlo simulation, described in sec. 7.2 was adapted to fit the present setup. It should be noted, that in the present setup, where all readout strips point in z-direction, the measured inclination ϑ is the projection of the real inclination onto the x-y-plane. The inclination ϑ, measured for about 8000 tracks, is shown in fig. 7.19 (black). No quality criterion, except for at least one detected hit in each Micromegas, is imposed.

The expected distribution for about 3000 straight tracks in an ideal detector is drawn in red. The shapes of the measured (black) and the expected (red) distribution differ, unaffected by
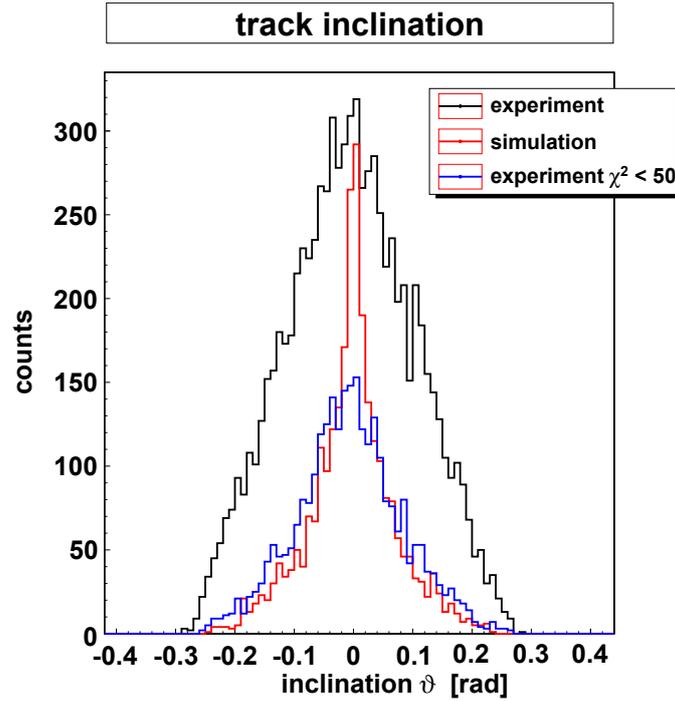
Figure 7.19: Inclination of cosmic muon tracks. The black curve corresponds to 8000 tracks, the blue curve corresponds to 3000 tracks with a cut on multiple scattering, the red curve is the expectation for about 3000 tracks.

the different number of tracks in each sample. Obviously, a smaller number of perpendicular tracks, i.e. tracks with $\vartheta = 0$ seems to be measured. If inclined tracks, appearing as perpendicular, due to the projection onto the x-y-plane, could not be detected, this would be visible in the efficiency. The efficiency is close to 1.0 though, thus a different explanation must be found.

It has already been stated in the previous sections, that a considerable amount of soft, i.e. low energetic muons is detected. Those muons can be scattered under quite large angles, resulting in a distortion of the inclination spectrum. One can reduce the number of massively scattered muons in the sample, by imposing a cut on the fit quality, given by the fit's χ^2. When only considering tracks with $\chi^2 < 50$, which is not a very tight condition, the number of tracks reduces to about 3000 (blue histogram in fig. 7.19). The expected and measured distributions' shapes are now similar, although still too few perpendicular tracks are detected. Nevertheless, the agreement is acceptable, considering that the simulation ignores the setup's possible internal rotation and the finite spatial resolution. A complete software reduction of multiple scattering is impossible. An internal rotation would not necessarily be visible in the single detector residuals.

It can be safely assumed, that in a high energetic particle beam, the multiple scattering's influence will decrease substantially. To cleanly measure the angular distribution of cosmics, the spectrum should be hardened. This can be achieved by including a lead absorber of several ten centimeter thickness between Micromegas three and the lower scintillator. Alternatively cherenkov detectors could be used as triggers. Since the condition for occurence of cherenkov radiation in a medium with refractive index n is $\beta > 1/n$, fast particles can be selected by choosing an appropriate radiator.

Chapter 8

Signal Formation in Micromegas

8.1   The Basics of Signal Formation

As the Micromegas is a parallel plate gas detector, the drift of electrons and ions gives rise to the observed signals. When taking a closer view though, the process is quite complex as pulse height and form depend on the gas properties, the electric fields in drift and in amplification gap and also on the capacities within the detector. The latter point is the one causing the complexity but also giving insight, how to increase pulse height.

In this section, the general concept of signal formation will be introduced. In the following sections several facets will be investigated and their influence on the pulse form and height will be worked out.

The expected pulse form can be analytically calculated. Assuming that the process of gas amplification is fast compared to the ion drift, giving rise to the pulse's temporal behavior, the duration of electron drift and gas amplification in the amplification region can be completely neglected.
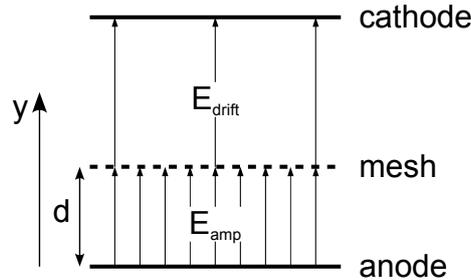

Figure 8.1: Schematic view of the detector. The distance mesh-anode of $128\,\mu m$ is denoted with d. The distance cathode-mesh of 6-7 mm is irrelevant in the following discussion.

At first, the situation at $t = 0$ will be described. Let n electrons enter the amplification gap (see fig. 8.1) with width d, making gas amplification in the strong, homogeneous field. The electron charge as a function of the distance y is

$$Q_{e^-}(y) = -ene^{\alpha(d-y)} \ , \tag{8.1}$$

where α is the first Townsend coefficient. The positive ion charge on the other hand is

$$Q_i(y) = ene^{\alpha(d-y)} - ne \ , \tag{8.2}$$

giving rise to an ion charge density in planes with thickness $\mathrm{d}y$, parallel to the anode and the mesh

$$\rho_i(y) = -\frac{\mathrm{d}Q_i}{\mathrm{d}y} = \alpha e n e^{\alpha(d-y)} \ . \tag{8.3}$$

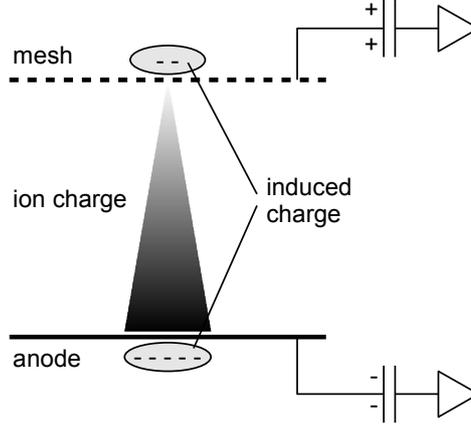The status at $t = 0$ is now as follows and can be seen in fig. 8.2.

Figure 8.2: Situation at $t = 0$ after completed gas amplification. Electrons on the mesh are attracted by the ion cloud. Since the mesh was neutral before and no charge from gas amplification has reached the mesh yet, a positive charge is observed by a preamplifier on the mesh. The case is different on the anode, since the electrons from gas amplification have reached it. A large fraction of them is trapped, still, the rest can already be detected.

The total electron charge of $q_e = Q_{e^-}(0) = ene^{\alpha d}$ resides on the anode, the positive ions are distributed in the amplification gap according to eq. (8.3). The ion charge on the mesh q_i is zero at $t = 0$. The ions induce negative charge q_{mi} on the mesh. In the same manner, a portion of the electron charge from gas amplification, residing on the anode, is attracted by the ion cloud and thus trapped. The amount of electron charge trapped, is equivalent to the amount of negative charge q_{ai}, that the ion cloud would induce on the anode, if it were neutral. The amount of observable charge, i.e. the charge that can flow off the anode q_a or the mesh q_m, is given by

$$q_a = \underbrace{q_e}_{<0} - \underbrace{q_{ai}}_{<0} < 0 \tag{8.4}$$

for the anode and

$$q_m = \underbrace{q_i}_{>0} - \underbrace{q_{mi}}_{<0} > 0 \tag{8.5}$$

for the mesh, respectively. Although the complete electron charge has reached the anode, a large fraction of q_{ai}/q_e can not flow off, since it is bound by the positive ions in the amplification region. The induced negative charge on the mesh q_{mi} leads to a positive observable charge on the mesh.

The ion charge density as a function of position and time can be calculated, by assuming, that the ions drift with a constant drift velocity v in the electric amplification field

$$\rho_i(y,t) = \alpha e n e^{\alpha(d-y+vt)} \qquad \rho_i(y,t) = 0 \text{ for } y < vt \ . \tag{8.6}$$

The charge induced on the anode and the mesh can be calculated using the method of images (see fig. 8.3 for illustration). A positive point charge between two grounded plates induces a negative surface charge on each plane. The resulting electric field, potential and the surface charge itself can be calculated by adding a negative point charge on the far side of each plate. The negative point charge on the far side of the left plate, induces again a positive point charge on the right plate's adverted side and vice versa. The problem is solved by an infinite number of point charges on either side. The charge distribution on either plate can be numerically calculated, using about 5000 image charges.
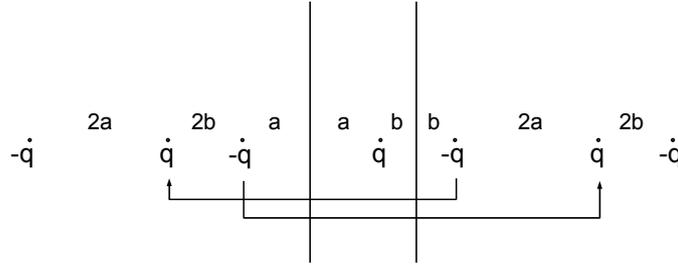

Figure 8.3: Method of images for a point charge q between two grounded plates.

Since electrodynamics is a linear theory, the superposition principle is applicable and the generalization to an arbitrary charge distribution is straight forward. In the following discussion, one result of the image charge analysis is used. The total amount of charge, induced on the anode and the mesh by a point charge q at position y distributes according to the respective distances:

$$q_{ai} = -q\frac{d-y}{d} \tag{8.7}$$

and

$$q_{mi} = -q\frac{y}{d} = -q - q_{ai} . \tag{8.8}$$

For the charge distribution ρ_i one gets for the induced charge on the anode

$$q_{ai}(t) = -\int_{vt}^{d}(\frac{d-y}{d})\rho_i(y,t)\mathrm{d}y = -\alpha e n e^{\alpha d}\int_{vt}^{d}(1-\frac{y}{d})e^{\alpha(vt-y)}\mathrm{d}y \tag{8.9}$$

$$= -ene^{\alpha d}\left(1 - \frac{vt}{d} - \frac{1}{\alpha d} + \frac{1}{\alpha d}e^{\alpha(vt-d)}\right) \tag{8.10}$$

and for the induced charge on the mesh

$$q_{mi}(t) = -\int_{vt}^{d}\rho_i(y,t)\mathrm{d}y - q_{ai}(t) = -\alpha e n e^{\alpha d}\int_{vt}^{d}e^{\alpha(vt-y)}\mathrm{d}y - q_{ai}(t) \tag{8.11}$$

$$= -ene^{\alpha d}\left(1 - e^{\alpha(vt-d)}\right) - q_{ai}(t) . \tag{8.12}$$

The amount of electron charge on the anode is constant in time

$$q_e = -ene^{\alpha d} =: -q_0 . \tag{8.13}$$

The ion charge on the mesh can be calculated by

$$q_i = q_0 - ne - \int_{vt}^{d}\rho_i(y,t)\mathrm{d}y = ne\left(e^{\alpha vt} - 1\right) . \tag{8.14}$$

Now using eqs. (8.4) and (8.5), the temporal behavior of the charges on the anode and the mesh can be calculated. Comparable results are stated by Mathieson and Smith [1988] for a parallel plate avalanche counter.
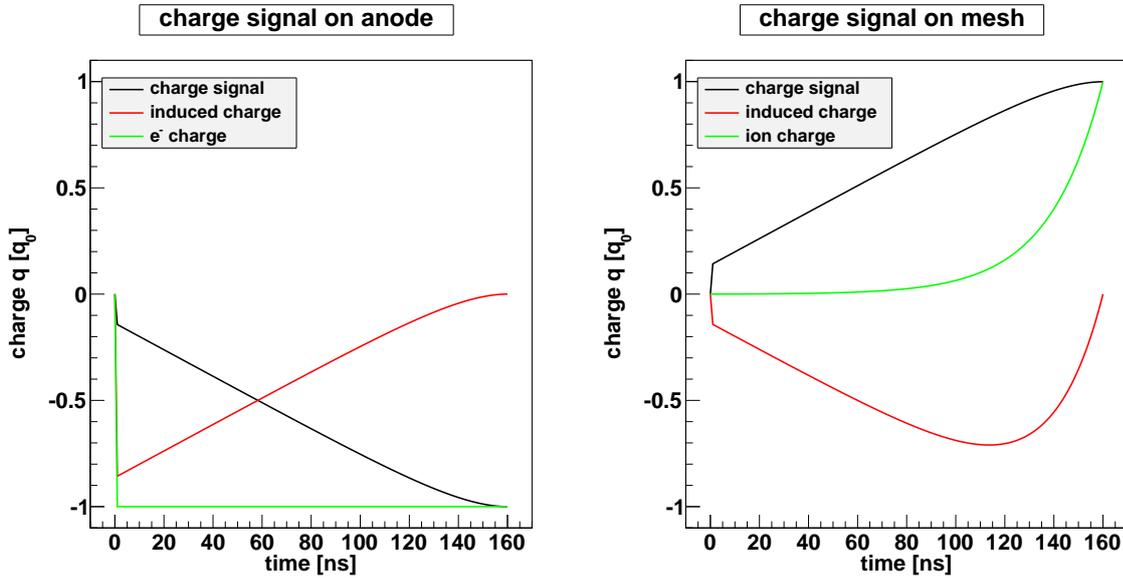

Figure 8.4: Observable charge signals on the anode and the mesh (black) as well as the induced charges (red) and the contribution of the charge from gas amplification (green). Assumed is an ion mobility $\mu^+ = 1.6\ cm^2/Vs$, an electric field of $50\ kV/cm$ (see sec. 2.2) and an amplification gap of $d = 128\ \mu m$.

Fig. 8.4 shows the temporal behavior of the observable charges on the anode and mesh, as well as the induced charges and the charges, originating from gas amplification. The anode charge signal has a very steep decline, caused by the fraction of electrons, that are able to leave the anode right away. This fraction is about 14%. The signal's slow component is dominated by the ion drift to the mesh. The signal's fall time from 10% to 90% of the final value is $t_f = 127\ ns$.
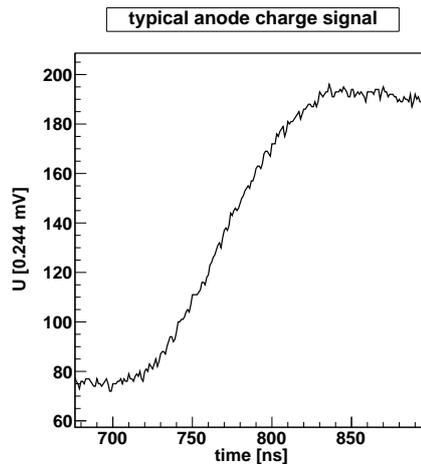

Figure 8.5: Typical anode charge signal.

A typical charge signal, acquired with a Micromegas with single preamplifier readout under irradiation by a ^{55}Fe source, can be seen in fig. 8.5. The preamplifier inverts the negative charge signal, resulting in a measurable positive voltage signal. It should be noted, that

the rise time of about 100 ns is similar to the expectation. A steep initial rise due to the prompt electron component is not observed. This can be understood by comparing the expected current signal with the measured. Both current signals were obtained by numerically differentiating the respective charge signals. Again, the measured signal corresponds to a current of negative electrons, although it is positive due to the preamplifier's inversion.
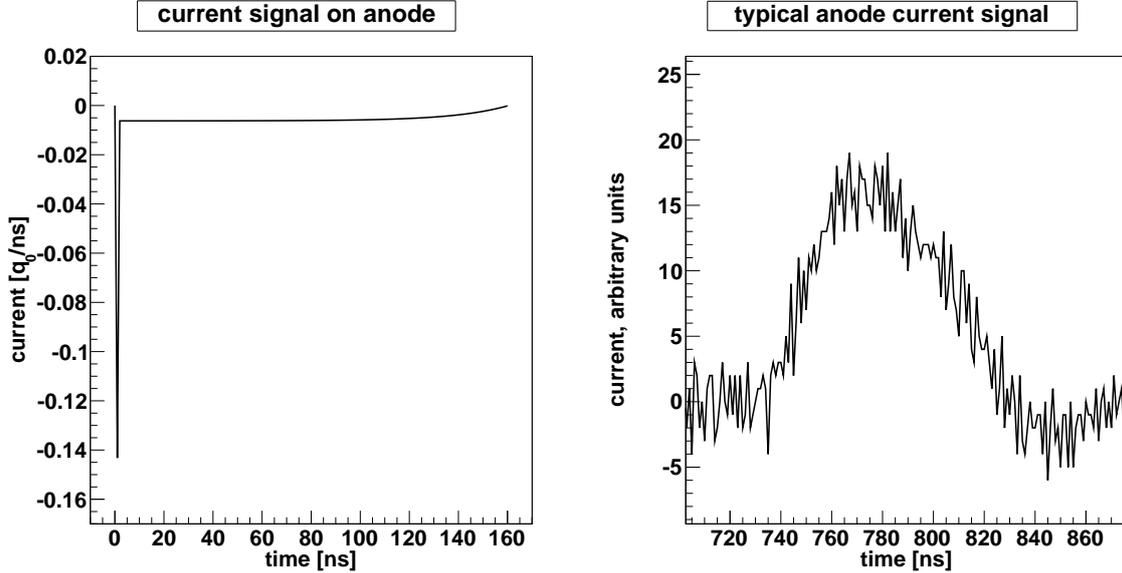

Figure 8.6: Expected (right) and measured (left) current signal.

The measured current signal is asymmetric, with a fast rise time of about 25 ns and a slower fall time around 50 ns. The very short prompt electron pulse can not be resolved due to the preamplifier's internal rise time and the detector capacitance and inductance. Measurements with a relatively fast current sensitive preamplifier revealed a similar current pulse as derived from the charge sensitive preamplifier. At the moment, the development of a current sensitive preamplifier with rise time below 0.1 ns in the LMU electronics workshop is ongoing. It should be capable of resolving the electron component, if the influence of the detector impedance can be neglected. This needs to be investigated. The calculated current pulse though as well as the dependence of the signal's length on the drift gap d is in agreement with observations by other groups (see e.g. [Charpak et al., 2002; Bay et al., 2002]).

The rise time of muon signals as a function of the field in the drift region between mesh and cathode for different gases, as well as comparisons to simulated MAGBOLTZ data can be found in sec. 8.5. In the following, the pulse height's dependence on different readout strip configurations will be discussed.

8.2 Pulse Height Dependence on the Readout Structure

Fig. 8.7 is the compilation of several measurements with ^{55}Fe in the single preamplifier configuration and shows the pulse height of 5.9 keV X-rays under variation of the amplification field for different groups of readout strips. During these measurements a certain number of neighboring strips were shorted and read out via the usual protective circuit with the Canberra 2004 charge sensitive preamplifier. The other strips were also short-circuit and connected to ground using a 1 kΩ resistor.

Two essential features can be extracted from fig. 8.7: First, the pulse height rises as expected with increasing amplification field. This has already been treated in sec. 6.3. Second, the

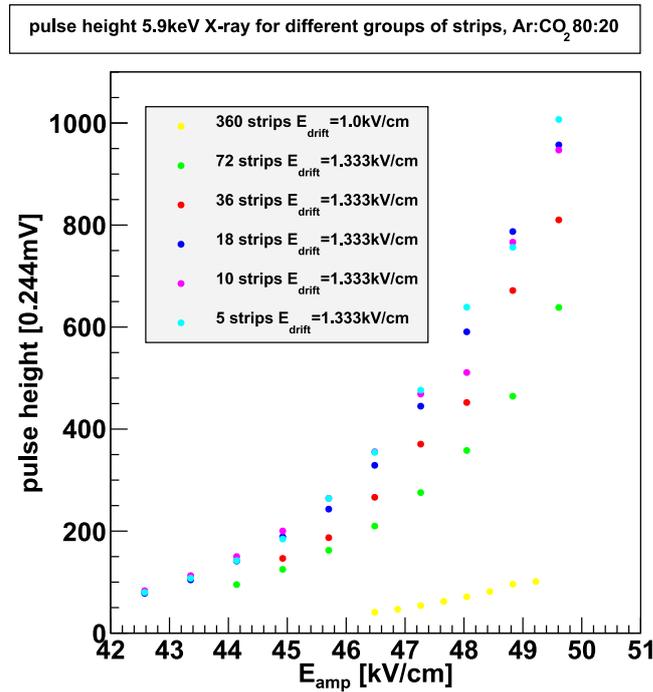pulse height rises for a decreasing number of shorted and readout strips.

Figure 8.7: Pulse height of 5.9 keV X-rays for different groups of readout strips as a function of the field in the amplification gap.

The rise in pulse height with decreasing number of readout strips is a somewhat unexpected feature and deserves further investigation. It might be due to the distribution of charge Q_0 between the detector capacitance and the coupling capacitor in the preamplifier (see fig. 8.8).
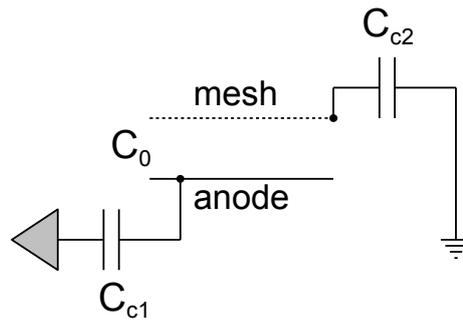

Figure 8.8: Simplified picture of the capacities involved in signal formation. The resistances in the signal line, the ones grounding the anode and the resistor connecting the mesh to the HV-supply are ignored. In the same manner the capacitance that the anode should have to the grounded backplane of the supportive PCB is neglected.

It seems plausible to assume, that the amount of charge Q_{c1} reaching the coupling capacitor C_{c1} in the preamplifier and thus being converted into a recordable voltage signal depends on the ratio of the detector capacitance C_0 to the capacitance of C_{c1}. Charge from the anode will flow into C_{c1} until the voltages on these two capacitors, given by $U = Q/C$, are equal. Thus

$$U_{\text{out}} \propto Q_{c1} = \frac{Q_0}{1 + C_0/C_{c1}} \ , \tag{8.15}$$

where Q_0 is the total charge, produced in gas amplification.

Testing this assumption with the geometric capacitances for the 360 strip and the 72 strip configuration of $C_0^{360} = 696\,\text{pF}$ and $C_0^{72} = 139\,\text{pF}$ gives, together with a coupling capacitor of $C_{c1} = 970\,\text{pF}$, an expectation for the pulse height ratio

$$\frac{U_{\text{out},72}}{U_{\text{out},360}} = \frac{1 + C_0^{360}/C_{c1}}{1 + C_0^{72}/C_{c1}} = 1.5 \ . \tag{8.16}$$

For the calculation of capacitances, see sec. 8.3. Comparison with the data, shown in fig. 8.7 reveals, that this effect is not the whole story, since the measured ratio of 6.5 is considerably larger.

It has been observed in other measurements, that the pulse height rises, if a capacitor C_{c2} between the mesh and ground i.e. the detector housing is included. For a capacitor $C_{c2} = 0.47\,\text{nF}$ the pulse height becomes larger by a factor of 1.7, for $C_{c2} \gtrsim 2\,\text{nF}$, the pulse height increases saturated to a factor of ≈ 3.3.

This behavior can be understood, by recalling the evolution of the measurable signal on the anode. As the ions drift to the mesh, they draw electrons onto it, releasing the same number of electrons on the anode. For the separation of positive and negative charges on the mesh, energy is necessary, since they attract each other. This would not be the case, if the mesh was grounded i.e. if it could fall back on an infinitely large charge reservoir. It is thus plausible to assume, that the amount of energy necessary to create the image charge on the mesh is smaller, if an additional capacity is connected to the mesh. If it is energetically favorable, to trap electrons on the anode instead of drawing electrons onto the mesh, less electrons on the anode can be released during the ion drift. Of course, even without an additional capacity the electrons are released, when the ion charge leaves the mesh. Since this happens over a $10\,\text{M}\Omega$ charge resistor with a time constant of $7\,\text{ms}$, these electrons cannot contribute to the fast $100\,\text{ns}$ signal.

It should be noted, that the term ion charge stands for the net ion charge on the mesh. Since the mesh is on a negative potential of about -550 V, it carries of course a considerable negative charge. However, this is irrelevant in the discussion above.

Now, the strongly increased pulse height, when reading out a subsample of n readout strips, can be understood. The $360 - n$ strips, that are not read out, are grounded. Thus they form an additional capacitor between the mesh and ground. This has the same effect as an additional capacitor, described in the previous paragraph. Loosely speaking, the induced observable positive pulse can flow off the mesh to ground over the capacity, formed by the mesh and the grounded anode strips, allowing the electrons trapped on the anode to flow off, into the charge sensitive preamplifier. The ion pulse's propagation over the mesh-grounded-strips capacitor leads to a small positive signal on the grounded strips. This has indeed been observed.

To investigate, whether the observed behavior of the pulse height can indeed be explained solely by the capacitances involved, a simulation, described in the following section, has been developed.

8.3   Simulation of Signal Formation with LTSpice IV

The circuit simulation program LTspice IV [Linear Technology Corporation, 2010], which is a free graphical implementation of Spice III, is used to investigate the influence of the capacitor network, formed by the detector, on the pulse height. By this means a detailed analysis of the signal formation and identification of possibilities to enlarge pulse height is possible. In this section the general model will be described, results and comparison with experimental data will be shown in sec. 8.4.

Two kind of measurements are simulated: The behavior of the pulse height when reading out a subsample of n shorted strips, whereas the other $360 - n$ are grounded via a $1\,\mathrm{k\Omega}$ resistor, and the pulse height's behavior when different capacitors between $0.47\,\mathrm{nF}$ and $10\,\mathrm{nF}$ are included between the mesh and ground.

Fig. 8.9 shows the input schematic for the simulation. The Micromegas' relevant parts are modeled by discrete capacitors, any inductance is neglected. Since the backplane of the detector PCB as well as the detector housing is grounded, most parts in the detector also form a capacitor directly to ground.
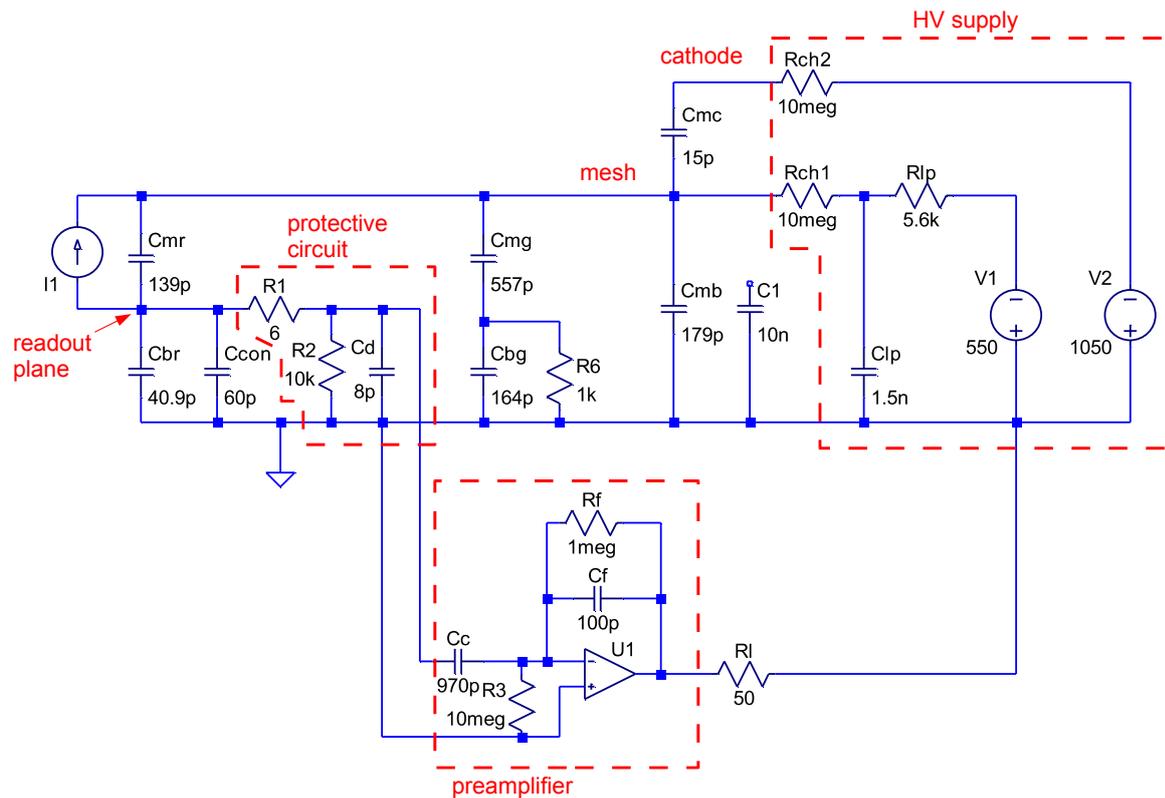

Figure 8.9: Schematics of the capacitors and resistors in a Micromegas model.

A constant current pulse is given onto the point, symbolizing the readout plane, and onto the mesh. The charge applied within the $10\,\mathrm{ns}$ duration of this pulse with $I = 17.6\,\mathrm{\mu A}$ is equal to $1.1 \cdot 10^6\,\mathrm{e}$, the amount of charge created by a $5.9\,\mathrm{keV}$ photon in argon after a gas gain of 5000. No significant difference in the pulse height's behavior was observed, when applying the same amount of charge over a duration of $100\,\mathrm{ns}$.

All capacitances in the Micromegas are calculated using the formula for parallel-plate capacitors

$$C = \varepsilon_0 \varepsilon_r \frac{A}{d} \ , \tag{8.17}$$

where $\varepsilon_0 = 8.85 \cdot 10^{-12}$ As/Vm is the vacuum permittivity, ε_r is the relative permittivity of the dielectric[1], A is the area and d the distance of the two plates.

symbol	description
C_{mr}	capacitance between mesh and read out anode strips
C_{br}	capacitance between read out anode strips and backplane
C_{mg}	capacitance between mesh and grounded anode strips
C_{bg}	capacitance between grounded anode strips and backplane
C_{mb}	capacitance between mesh and backplane
C_{mc}	capacitance between mesh and cathode
C_{con}	capacitance of ERNI connector; when reading out 360 strips, a total connector capacitance of $C_{\mathrm{con}} = 300$ pF is assumed
C_{d}	capacitance of two BAV99 diodes
C_{c}	coupling capacitor in preamplifier
C_{f}	feedback capacitor in preamplifier
C_{lp}	capacitor in the low pass, used to filter the mesh HV
C_1	additional variable capacitor from mesh to ground
I_1	current source, exhibits a single constant current pulse $I = 17.61$ µA with 10 ns duration
V_1, V_2	HV sources
U_1	ideal operational amplifier

Table 8.1: Summary of the not self explaining components in fig 8.9.

The other values are either directly measured, or the imprinted value is taken. The only estimated capacitance is the connector's capacitance C_{con}, which is impossible to measure, since the female part is installed on the detector and cannot be determined separately. A value of 60 pF for a single couple and thus 300 pF for five couples seem reasonable. Tab. 8.2 summarizes the assumptions and the results for the calculated capacities.

Capacitor	A [m^2]	d [m]	$\varepsilon_{\mathbf{r}}$	capacitance [pF]
$C_{\mathrm{mr,1}}$	$0.1 \cdot 150 \cdot 10^{-6}$	$128 \cdot 10^{-6}$	1	1.037
$C_{\mathrm{mr,2}}$	$0.024 \cdot 150 \cdot 10^{-6}$	$128 \cdot 10^{-6}$	3.6	0.897
C_{mr}				1.933
C_{br}	$0.19 \cdot 150 \cdot 10^{-6}$	$1.6 \cdot 10^{-3}$	3.6	0.568
C_{mb}	$9.53 \cdot 10^{-3}$	$1.7 \cdot 10^{-3}$	3.6	179
C_{mc}	$1 \cdot 10^{-2}$	$6 \cdot 10^{-3}$	1	15

Table 8.2: Calculated capacitances, values are given for one strip, if possible. The total values used in the simulation are then simply calculated while assuming that all single strip capacitors are in parallel. C_{mr} consists of two parts, the capacitance in the sensitive area and the capacitance resulting from the mesh's overlap with the strips outside the active area.

A single step charge sensitive preamplifier is also added to achieve an integration over the current signal since LTspice is only able to display voltages and currents. As both preamplifiers, the ideal simulated one and the used Canberra 2004 should exhibit a linear charge to voltage conversion, there will be no distorting effect on the pulse height apart from a scaling factor, but the exact signal timing e.g. rise time, will not be reproducible. The latter was not

---

[1] ≈ 1 for gas, $= 3.6$ for PCB material

the motivation for this simulation anyway. Nevertheless, the basic pulse shape is reproduced as can be seen in fig. 8.10.
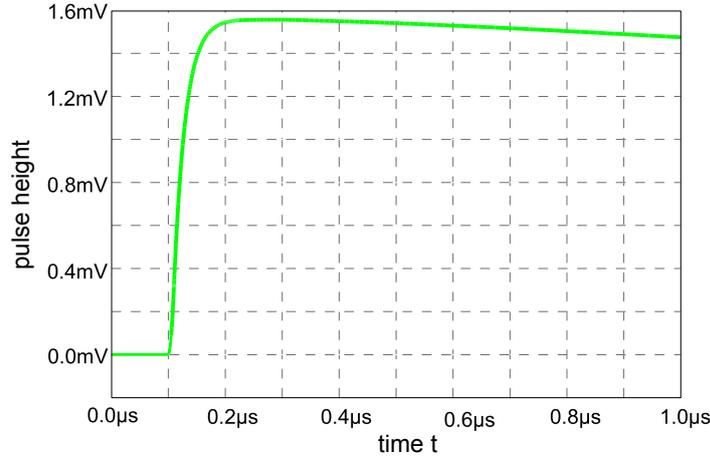

Figure 8.10: Ideal charge amplifier's output into the 50 Ω load, simulated with LTSpice.

The HV side is just added for the sake of completeness, signals are very efficiently blocked by the two 10 MΩ charge resistors R_{ch1} and R_{ch2}.

LTSpice calculates the temporal behavior of the shown schematic, reacting to the current pulse. The pulse height though is the only value extracted for the following discussion.

8.4   Experimental Results

The behavior of the pulse height of ^{55}Fe's 5.9 keV line under variation of the number of read out strips can be seen in fig. 8.11. The measurements were conducted using Ar:CO$_2$ 80:20 at NTP and an amplification field of $E_{amp} = 46.5$ kV/cm. The error bars correspond to the 5.9 keV line's standard deviation, assuming a Gaussian shape. Predictions from the LTSpice simulation described above, are superimposed as red triangles. To obtain the good agreement visible, the simulated output voltage values are scaled by a factor of $f_{46.5} = 217$, corresponding to the difference in amplification between simulated and real preamplifier.

Fig. 8.12 shows the behavior of the 5.9 keV line's pulse height as a function of the additional capacitance between mesh and ground. The data were measured at an amplification field of $E_{amp} = 48.0$ kV/cm. The agreement between data and simulation is acceptable. Since the field is different in these measurements, a different scaling factor of $f_{48.0} = 287$ is used. The gas gain and thus the expected pulse height at the two amplification fields can be extracted from fig. 6.7: $G_{46.5} = 2700$ and $G_{48.0} = 4250$. Comparing the gain ratio $G_{48.0}/G_{46.5} = 1.57$ and the ratio of scaling factors $f_{48.0}/f_{46.5} = 1.32$, a deviation of 15% is visible. This might be due to different environmental conditions, as quite considerable deviations of the 5.9 keV line's pulse height between measurements with the same electric field parameters have been observed (see e.g. fig. 6.6).

A single step charge sensitive preamplifier outputs a voltage $U_{out} = -Q_{in}/C_f$ proportional to charge and feedback capacitance. Thus, if the whole charge of -176 fC, being injected into the detector in the LTSpice simulation, would be detected in the charge sensitive preamplifier with feedback capacitor $C_f = 100$ pF, an output voltage of 1.76 mV would be expected. The actually determined values are smaller, since some charge cannot leave the detector due to its finite capacitance and the remaining "ion" charge on the mesh. The values determined in the simulation for different readout strip configurations, can be found in tab. 8.3.
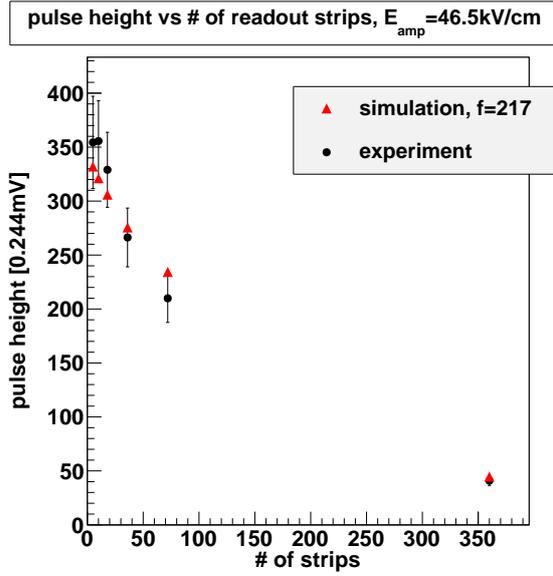
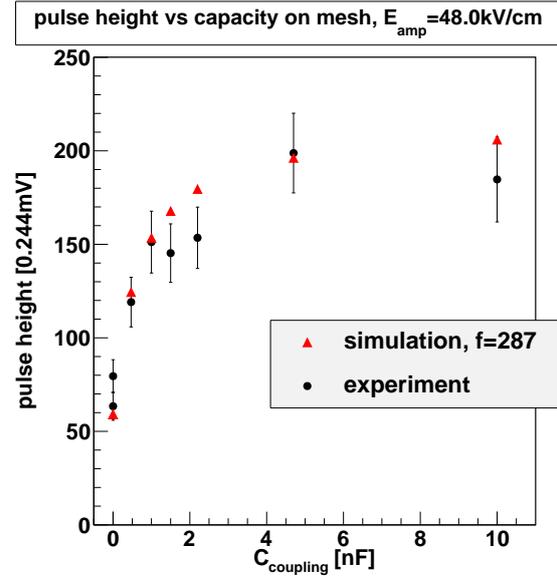Figure 8.11: Pulse height of 5.9 keV X-rays as a function of the number of read out strips.

Figure 8.12: Pulse height of 5.9 keV X-rays as a function of the additional capacitor between mesh and ground.

Number of strips	5	10	18	36	72	360
Q_{preamp}/Q_{total}	0.88	0.85	0.81	0.73	0.62	0.12

Table 8.3: Results of the LTSpice simulation: Fraction of created charge, reaching the preamplifier. A charge of $Q_{total} = -1.76 \cdot 10^{-13}$ C is injected.

8.5 Rise Time of Cosmic Muon Signals

The rise time of muon signals reflects the drift of electrons in the drift gap between mesh and cathode. A muon traversing the detector, ionizes the detector gas along its path. The signal starts, as soon as the electrons, created very close to the mesh, reach the amplification gap. Electrons, created in the cathode's proximity, reach the amplification region after a time

$$t_d = d_{\mathrm{d}}/v_d \ , \tag{8.18}$$

determined by their drift velocity v_d and the drift gap's width d_{d}.

The electron drift velocities in the gas mixtures at different electric fields can be calculated with MAGBOLTZ. Thus, using eq. (8.18), the time, after which the electrons, produced directly at the cathode, have reached the amplification region can be calculated. It is expected, that the muon signal's rise time is the quadratic sum of the intrinsic signal's rise time and the drift time

$$t_{r,\mu} = \sqrt{t_{r,^{55}\mathrm{Fe}}^2 + t_d^2} \ . \tag{8.19}$$

The measured rise times though are systematically smaller. Fig. 8.13 shows the measured signal rise times in 80:20 and 93:7 Ar:CO_2 mixtures as well as the calculated maximum drift times. It should be stressed, that the shown maximum drift time t_d is smaller than the expected rise time $t_{r,\mu}$. The drift behavior of electrons is clearly visible in the signal's rise time, since the graphs have similar shape.
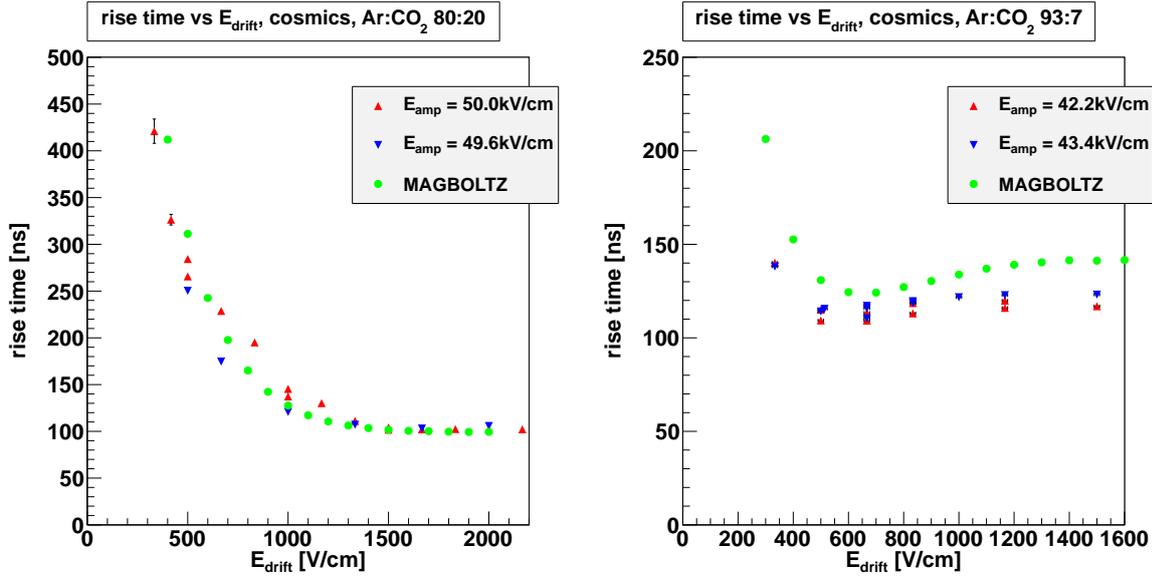
Figure 8.13: Rise time of muon signals as a function of the drift field for two different mixtures of Ar:CO$_2$ and two different amplification fields.

The observed deviation might be caused by several effects: First, the amplification field close to the mesh is not constant as assumed in this discussion, but it is larger, as has been shown in sec. 6.3. Ions might thus have a considerably larger drift velocity close to the mesh. Trying to approximate this contribution, one can assume a 17% larger Townsend coefficient instead of assuming a 17% larger amplification region of 150 μm as has been done in the discussion of the gas amplification. This would correspond to homogenous but by a factor of 1.08 larger amplification field (see fig. 2.7). Thus also the ion's drift velocity and with it the expected signal rise time $t_{r,^{55}\mathrm{Fe}}$ would be 8% smaller.

Second, the cathode might be deformed, due to electrostatic forces, forming a smaller drift gap than expected. This would directly influence the maximum drift time of electrons t_d.

Third, the rise time is derived by fitting the signals' rising edge with a Fermi function (eq. (4.5)). This allows for accurately determining the pulse height, but it is not optimized for determining the rise time. The difference in shape of the fit and the actual signal might introduce an error of a few percent.

Nevertheless, a qualitative agreement is visible, the details though, still need further investigation.

8.6   The Whole Picture

It could be shown, that the signals in Micromegas are due to the drift of ions in the amplification gap. A very fast electron component, corresponding to 14% of the total charge, could in principle be detected with a very fast current sensitive preamplifier. Thus, if the gas gain is high enough, this component could be used for timing measurements with a resolution < 1 ns. It has furthermore been shown, that the pulse height of signals is determined by the detector capacitances. For single plane readout, it is advantegous to include an additional capacitor between mesh and ground to enlarge pulse height. When reading out all single strips seperately, as done in the Gassiplex strip readout, an additional capacitor is not necessary, since the strips not hit are drawn to "virtual" ground and fulfill the function of an additional

capacitor. It should be noted, that an additional capacitor has a negative effect, too. The amount of charge, stored on the mesh is proportional to its capacitance. In a discharge, the whole charge flows onto a single strip, thus an additional capacitor increases potential damage.

It could furthermore be shown, that the drift of electrons in the drift gap influences the rise time of muon signals, although the details deserve further investigation.

The Micromegas model allows for numerical investigation of the detector's signal response. This has e.g. been used to estimate the series resistor's value in the signal line, necessary for stable Gassiplex readout operation, by simulating discharges of the mesh onto single strips.

Chapter 9

Summary and Outlook

The goal of this thesis was to develop and commission a micro mesh based micro-pattern gas detector, known as Micromegas, as well as to investigate and describe its behavior and performance. Bulk Micromegas were studied, where the micro mesh is laminated in one single step with a photo resistive film onto a printed circuit board, carrying the readout structure. The readout structure consisted of 360 Au and Ni plated copper strips, $100\,\text{mm}$ long with a pitch of $250\,\mu\text{m}$. Several prototypes, with an active area of $90 \times 100\,\text{mm}^2$, an amplification gap of $128\,\mu\text{m}$ and drift gaps between 6-7 mm were put into operation (chap. 3). Tests with cosmic muons and a ^{55}Fe source, using Ar:CO_2 mixtures of 93:7, 90:10 and 80:20 % vol composition at normal pressure were performed.

Two different readout electronics were set up. Signal studies were performed by recording signals from a charge sensitive preamplifier with a $1\,\text{GHz}$ flash ADC (chap. 4). Complete signal cycles could be recorded and analyzed with respect to pulse height and rise time. Spark rates were examined by remotely monitoring the high voltage supplies.

A Gassiplex based strip readout, capable of multi event buffering, originally developed for the HADES RICH detector, was adapted to negative charge signals and protected against discharges, encountered in Micromegas (chap. 5). This was used to ultimately read out three detectors with in total 1080 channels. Stable operation over several days was possible, when capacitively coupling the readout strips to the Gassiplex frontends and improving discharge diversion by additional grounding.

It has been shown, that muon efficiencies of up to 98% at amplification fields of $E_{\text{amp}} = 50\,\text{kV/cm}$ and an energy resolution of 24% can be reached for single plane readout applying a single charge sensitive preamplifier. The rate of discharges, resulting from heavily ionizing particles and particle showers, could be minimized to $f_{\text{spark}} < 0.1\,\text{min}^{-1}$ at full efficient strip readout, by using Ar:CO_2 80:20 at $p \approx 1013\,\text{mbar}$. It could be shown, that the experimentally determined gas gain of 600 to 8000 are in good agreement with predictions from MAGBOLTZ calculations, assuming a slightly larger amplification region. This is necessary due to the slightly higher field in the mesh region (chap. 6). It has been argued, that the energy resolution is expected to improve considerably in Micromegas with thin electroformed meshes. This might directly influence the achievable spatial resolution. It is thus planned to build new prototypes with 384 strips, $250\,\mu\text{m}$ pitch and an active area of $96 \times 500\,\text{mm}^2$ using bulk technology and electroformed meshes. These large prototypes will be able to provide a cosmic trigger and track monitor for small ATLAS muon tubes in neutron irradiation tests. Still larger Micromegas with 1024 strips and an active area of $256 \times 1000\,\text{mm}$ are able to provide a radiation hard tracking system for cosmic muon tests of ATLAS muon tubes in different geometrys and different gas mixtures in the Gamma Irradiation Facility at CERN. It is furthermore under investigation, whether sparking can be substantially reduced by inserting

a GEM foil on top of the mesh or including a second micromesh. Measurements in the COMPASS Micromegas indicate, that the use of a low Z detector gas like Ne, improves the sparking behavior considerably. This should be investigated in the present detectors.

The Gassiplex strip readout performed as expected for cosmic muons. Efficiencies of $\approx 99\%$ and $\approx 97\%$ have been achieved for two Micromegas at considerably reduced amplification fields of $E_{\mathrm{amp}} = 41\,\mathrm{kV/cm}$, enabling the low spark rates, described above. The reduction is possible, due to a higher preamplifier sensitivity and an intrinsically higher pulse height in single strip readout. Track reconstruction with a single detector spatial resolution of $(62 \pm 6)\,\mu\mathrm{m}$ was possible. It could be shown, that multiple scattering, due to the low energy part of the cosmic muon spectrum has a considerable influence on the measured spatial resolution. The measured hit and inclination distributions were in agreement with the expectation (chap. 7).

It is planned, to upgrade the three Micromegas setup to a muon beam track reference system with six or eight detectors, possibly including one or more micro-pattern GEM detectors [von Zuydtwyck, 2010], developed in the same group. The relatively small $100 \times 90\,\mathrm{mm}^2$ detectors would be suitable for this purpose at the H8 beamline at CERN. $140\,\mathrm{GeV}$ muons are going to be detected at a rate of $3\,\mathrm{kHz}$. To reduce data size and improve readout speed, the on board channel discrimination must be used in such high rate environments. It should be carefully evaluated if a periodic offset recalibration is necessary. New bus cards are going to be designed, capable of carrying six frontend modules. This will simplify the setup considerably, rendering the two dummy frontends and cable connections between frontends and bus cards unnecessary. Furthermore, eight detectors could be read out by a single readout controller, since only one port would be necessary per detector, in contrast to two per detector right now.

The measurements with the strip readout, presented in this thesis, have not yet been optimized with respect to efficiency, spark rate, pulse height and spatial resolution by optimization of gas and electric field parameters. The dependence of the spatial resolution on diffusion in several gas mixtures at different pressures still needs to be investigated. To show the Micromegas' suitability for replacement of cathode strip chambers in the ATLAS forward region, the influence of neutron and gamma irradiation on the spatial resolution will be examined. Tests with cosmic muons and a ^{252}Cf source or neutrons, produced in an α+Be reaction at the Tandem accelerator in Munich are planned [Ruschke, 2010]. Furthermore, muon beam tests at the H8 experimental area of CERN's SPS, with and without additional irradiation by a neutron source are intended.

A simulation model, describing the Micromegas' relevant parts as capacitors, has been developed, that allows for calculating the detector's response to current pulses. The behavior of the pulse height as a function of the number of read out strips could be explained, as well as the pulse height's dependence on an additional mesh to ground capacity. The analytically calculated pulse forms agree with the measured, although a deviation in the pulse's rise time still needs to be investigated. As soon as a fast current sensitive preamplifier, with a rise time $< 1\,\mathrm{ns}$ is available, the anode and mesh current signals will be studied, to verify conformity with the analytically calculated pulses.

Bibliography

[Alexopoulos et al.(2010a)] T. Alexopoulos, D. Attié, M. Boyer, P. Colas, J. Derré, F. Diblen, G. Fanourakis, E. Ferrer-Ribas, E. Gazis, T. Geralis, A. Giganon, I. Giomataris, S. Herlant, F. Jeanneau, S. Kirch, E. Ntomari, Th. Papaevangelou, M. Titov, A. Tomás, and G. Tsipolitis. Micromegas study for the sLHC environment. *JINST*, 5(02):P02003, 2010a.

[Alexopoulos et al.(2010b)] T. Alexopoulos et al. Development of large size Micromegas detector for the upgrade of the ATLAS Muon system. *Nucl. Instr. and Meth. A*, 617(1-3):161 – 165, 2010b.

[Allison and Cobb(1980)] W.W.M. Allison and J.H. Cobb. Relativistic charged particle identification by energy loss. *Ann. Rev. of Nucl. and Part. Sc.*, 30(1):253–298, 1980.

[Barkas and Berger(1964)] W.H. Barkas and M.J. Berger. Nuclear science series report 39, 1964.

[Bay et al.(2002)] A. Bay, J. P. Perroud, F. Ronga, J. Derr, Y. Giomataris, A. Delbart, and Y. Papadopoulos. Study of sparking in micromegas chambers. *Nucl. Instr. and Meth. A*, 488 (1-2):162 – 174, 2002.

[Bernet et al.(2005)] C. Bernet, P. Abbon, J. Ball, Y. Bedfer, E. Delagnes, A. Giganon, F. Kunne, J.-M. Le Goff, A. Magnon, C. Marchand, D. Neyret, S. Panebianco, H. Pereira, S. Platchkov, S. Procureur, P. Rebourgeard, G. Tarte, and D. Thers. The gaseous microstrip detector Micromegas for the high-luminosity COMPASS experiment at CERN. *Nucl. Instr. and Meth. A*, 536(1-2):61 – 69, 2005.

[Beusch et al.(1994)] W. Beusch, S. Buytaert, C.C. Enz, E.H.M. Heijne, P. Jarron, F. Krummenacher, F. Piuz, and J.C. Santiard. Gasplex a low noise analog signal processor for readout of gaseous detectors. Internal note, CERN-ECP/94-17, 1994.

[Bichsel(2006)] H. Bichsel. A method to improve tracking and particle identification in TPCs and silicon detectors. *Nucl. Instr. and Meth. A*, 562(1):154 – 197, 2006.

[Bittner et al.(2010)] B. Bittner, J. Dubbert, S. Horvat, O. Kortner, H. Kroha, F. Legger, R. Richter, S. Adomeit, O. Biebel, A. Engl, R. Hertenberger, F. Rauscher, and A. Zibell. Development of fast high-resolution muon drift-tube detectors for high counting rates. *Nucl. Instr. and Meth. A*, In Press, Corrected Proof:–, 2010.

[Böhmer(1999)] M. Böhmer. Das Auslesesystem für den Ringabbildenden Čerenkovdetektor im HADES Spektrometer. Master's thesis, Technische Universität München, 1999.

[Brooks Instrument(2008a)] Brooks Instrument. Brooks Smart (DMFC) MFC/MFM. http://www.brooksinstruments.com, 2008a.

[Brooks Instrument(2008b)] Brooks Instrument. Brooks Models SLA5850, SLA5851, SLA5853 Mass Flow Controllers and Models SLA5860, SLA5861, SLA5863 Mass Flow Meters. http://www.brooksinstruments.com, 2008b.

[Burnens(2009)] J. Burnens. BULKX Infos Pratiques V2 en. not published, 2009.

[Burr-Brown Corporation(2005)] Burr-Brown Corporation. 10-bit, 20 MHz Sampling Analog-to-Digital Converter. http://www.ti.com, 2005.

[CAEN S.p.A.(1991)] CAEN S.p.A. Technical Information Manual Mod. N 93 B. http://www.caen.it, 1991.

[CAEN S.p.A.(2003)] CAEN S.p.A. Technical Information Manual Mod. N1145. http://www.caen.it, 2003.

[CAEN S.p.A.(2004)] CAEN S.p.A. Technical Information Manual Mod. V977. http://www.caen.it, 2004.

[CAEN S.p.A.(2010)] CAEN S.p.A. Technical Information Manual Mod. V1729. http://www.caen.it, 2010.

[Canberra Industries, Inc.(2007)] Canberra Industries, Inc. Canberra 2004 data sheet. http://www.canberra.com, 2007.

[Charles and Cooke(1968)] M.W. Charles and B.A. Cooke. Proportional counter resolution. *Nucl. Instr. and Meth.*, 61(1):31 – 36, 1968.

[Charpak et al.(2002)] G. Charpak, J. Derr, Y. Giomataris, and Ph. Rebourgeard. Micromegas, a multipurpose gaseous detector. *Nucl. Instr. and Meth. A*, 478(1-2):26 – 36, 2002.

[Dafni et al.(2009)] T. Dafni, E. Ferrer-Ribas, Y. Giomataris, Ph. Gorodetzky, F. Iguaz, I.G. Irastorza, P. Salin, and A. Toms. Energy resolution of alpha particles in a microbulk micromegas detector at high pressure argon and xenon mixtures. *Nucl. Instr. and Meth. A*, 608(2):259 – 266, 2009.

[Deile et al.(2004)] M. Deile, J. Dubbert, S. Horvat, O. Kortner, H. Kroha, A. Manz, S. Mohrdieck-Mck, F. Rauscher, R. Richter, A. Staude, and W. Stiller. Resolution and efficiency of the ATLAS muon drift-tube chambers at high background rates. *Nucl. Instr. and Meth. A*, 535(1-2):212 – 215, 2004.

[Demtröder(2004)] W. Demtröder. *Experimentalphysik 2 - Elektrizität und Optik*. Springer, 2004.

[Deslattes et al.(2005)] R.D. Deslattes, E.G. Kessler Jr., P. Indelicato, L. de Billy, E. Lindroth, J. Anton, J.S. Coursey, D.J. Schwab, C. Chang, R. Sukumar, K. Olsen, and R.A. Dragoset. X-ray transition energies (version 1.2). http://physics.nist.gov/XrayTrans [2010, Oct 18th], National Institute of Standards and Technology, Gaithersburg, MD, 2005.

[Elantec(1994)] Elantec. EL4441C data sheet. http://www.e12.physik.tu-muenchen.de/~mboehmer/, 1994.

[Engl(2010)] A. Engl. MDT-Upgrade for sLHC. presentation, held at group seminar LS Schaile, http://www.etp.physik.uni-muenchen.de/dokumente/seminar_de.html, 6 2010.

[Engl et al.(2010)] A. Engl, O. Biebel, R. Hertenberger, A. Mlynek, T. A. Mueller, and F. Rauscher. ATLAS monitored drift tube chambers for super-LHC. *Nucl. Instr. and Meth. A*, 623(1): 91 – 93, 2010.

[Espargilière et al.(2009)] C. Espargilière, C. Adloff, D Attié, J. Blaha, et al. Micromegas chambers for hadronic calorimetry at a future linear collider. *JINST*, 4, 2009.

[G. Aad et al. (The ATLAS Collaboration)(2008)] G. Aad et al. (The ATLAS Collaboration). The ATLAS experiment at the CERN LHC. *JINST*, 3:S08003, 2008.

[Giomataris et al.(1996)] Y. Giomataris, Ph. Rebourgeard, J.P. Robert, and G. Charpak. Micromegas: a high-granularity position sensitive gaseous detector for high particle-flux environments. *Nucl. Instr. and Meth. A*, 376:29 – 35, 1996.

[Giomataris et al.(2006)] Y. Giomataris, R. De Oliveira, S. Andriamonje, S. Aune, G. Charpak, P. Colas, G. Fanourakis, E. Ferrer, A. Giganon, Ph. Rebourgeard, and P. Salin. Micromegas in a bulk. *Nucl. Instr. and Meth. A*, 560(2):405 – 408, 2006.

[Groom et al.(2001)] D.E. Groom, N.V. Mokhov, and S.I. Striganov. Muon stopping power and range tables 10 MeV - 100 TeV. *Atomic Data and Nuclear Data Tables*, 78(2):183–356, 2001.

[Grupen and Shwartz(2008)] C. Grupen and B. Shwartz. *Particle Detectors*. Cambridge University Press, 2008.

[Hashiba et al.(1984)] A. Hashiba, K. Masuda, T. Doke, T. Takahashi, and Y. Fujita. Fano factor in gaseous argon measured by the proportional scintillation method. *Nucl. Instr. and Meth. A*, 227(2):305 – 310, 1984.

[Hoek et al.(2007)] M. Hoek, L. Rubáček, M. Düren, M. Hartig, T. Keri, S. Lu, B. Seitz, W. Sommer, and H. Stenzel. Performance and response of scintillating fiber modules to protons and pions. *Nucl. Instr. and Meth. A*, 572(2):808 – 816, 2007.

[Hornbeck(1951)] J.A. Hornbeck. The drift velocities of molecular and atomic ions in helium, neon and argon. *Phys. Rev.*, 84(4):615–620, 1951.

[Hubbell et al.(1980)] J.H. Hubbell, H.A. Gimm, and I. Øverbø. Pair, Triplet, and Total Atomic Cross Sections (and Mass Attenuation Coefficient) for 1 MeV - 100 GeV Photons in Elements Z = 1 to 100. *Jour. of Phys. and Chem. Ref. Data*, 9(4):1023–1147, 1980.

[Iseg Spezialelektronik(2009)] Iseg Spezialelektronik. Bedienungsanleitung für Präzisions-Hochspannungs-Netzgeräte der Baureihe SHQ-HIGH-PRECISION. http://www.iseg-hv.de, 2009.

[Jeanneau et al.(2000)] F. Jeanneau, Y. Benhammou, R. Blaes, J. M. Brom, F. Charles, F. Didierjean, F. Drouhin, J. C. Fontaine, J. M. Helleboid, D. Huss, A. Pallars, I. Ripp-Baudot, P. VanLaer, and A. Zghiche. First results of micromegas detector with fast integrated electronics. *Nucl. Instr. and Meth. A*, 450(2-3):313 – 324, 2000.

[K. Nakamura et al. (Particle Data Group)(2010)] K. Nakamura et al. (Particle Data Group). Review of particle physics. *J. Phys. G*, 37(075021), 2010.

[Kaye & Laby Online(2005)] Kaye & Laby Online. Tables of physical & chemical constants 2.5.7 refractive index of gases. http://www.kayelaby.npl.co.uk/, 2005.

[Kleinknecht(1992)] K. Kleinknecht. *Detektoren für Teilchenstrahlung*. Teubner, 1992.

[Landau(1944)] L. D. Landau. On the energy loss of fast particles by ionization. *Jour. of Exp. and Theoret. Phys. (USSR)*, 8:201, 1944.

[Leo(1994)] W.R. Leo. *Techniques for Nuclear and Particle Physics Experiments*. Springer, 1994.

[Linear Technology Corporation(2010)] Linear Technology Corporation. Ltspice user's guide. http://www.linear.com/designtools/software/, 2010.

[MacDaniel and Mason(1973)] E. W. MacDaniel and E. A. Mason. *The Mobility and Diffusion of Ions in Gases*. Wiley, 1973.

[Magboltz(2010)] Magboltz. Magboltz cross sections. http://rjd.web.cern.ch/rjd/cgi-bin/cross, 2010.

[Mathieson and Smith(1988)] E. Mathieson and G. C. Smith. Charge distributions in parallel plate avalanche chambers. *Nucl. Instr. and Meth. A*, 273(2-3):518 – 521, 1988.

[MKS Instruments(1997a)] MKS Instruments. MKS Type 248A. http://www.mksinst.com, 1997a.

[MKS Instruments(1997b)] MKS Instruments. MKS Type 690A Absolute High Accuracy Pressure Transducer. http://www.mksinst.com, 1997b.

[Mlynek(2006)] A. Mlynek. Ortsauflösung der Driftrohre des ATLAS-Myonspektrometers bei Neutronenuntergrund. Master's thesis, Ludwig-Maximilians-Universitä München, 2006.

[ORTEC(2008)] ORTEC. 474 timing filter amplifier. http://www.ortec-online.de, 2008.

[P. Abbon et al. (The COMPASS Collaboration)(2007)] P. Abbon et al. (The COMPASS Collaboration). The COMPASS experiment at CERN. *Nucl. Instr. and Meth. A*, 577(3):455 – 518, 2007.

[Ruschke(2010)] Alexander Ruschke. Ageing Studies of ATLAS MDT Detectors and Irradiation with Protons and Neutrons. Master's thesis, Ludwig-Maximilians-Universität München, 2010.

[Sauli(1977)] F. Sauli. Principles of operation of multiwire proportional and drift chambers. *CERN-77-09*, 1977.

[Schade and Kaminski(2010)] P. Schade and J. Kaminski. A large TPC prototype for a linear collider detector. *Nucl. Instr. and Meth. A*, In Press, Corrected Proof:–, 2010.

[Sternheimer and Peierls(1971)] R.M. Sternheimer and R.F. Peierls. General expression for the density effect for the ionization loss of charged particles. *Phys. Rev. B*, 3(11):3681–3692, Jun 1971.

[Thomson et al.(2009)] A.C. Thomson et al. *X-Ray Data Booklet*. LBNL University of California, 2009.

[TUM Physik Dep. E12(2000)] TUM Physik Dep. E12. 64 channel analog multiplexing frontend, schematics. http://www.e12.physik.tu-muenchen.de/~mboehmer/, 2000.

[von Loeben et al.(2010)] J. von Loeben et al. Performance of Fast High-Resolution Muon Drift Tube Chambers for LHC Upgrades. IEEE Nucl. Scien. Sympos. and Med. Im. Conf., 2010.

[von Zuydtwyck(2010)] D. Heerman von Zuydtwyck. Development of Micro-Pattern Gaseous Detectors – GEM. Master's thesis, Ludwig-Maximilians-Universität München, 2010.

[Zeitelhack et al.(1999)] K. Zeitelhack, A. Elhardt, J. Friese, R. Gernhäuser, J. Homolka, A. Kastenmüller, P. Kienle, H. J. Körner, P. Maier-Komor, M. Münch, W. Przygoda, W. Schön, A. Ulrich, and J. Wieser. The HADES RICH Detector. *Nucl. Instr. and Meth. A*, 433 (1-2):201 – 206, 1999.

[Zibell(2010)] A. Zibell. Pulsformanalyse an MDT-Myondetektoren. Master's thesis, Ludwig-Maximilians-Universität München, 2010.

Appendix A

Index of Programs

In the following, programs and simulations, written in the course of this thesis are listed, together with a short description. All source files can be found under `/data/etp/bortfeldt/src`.

- `ana.c, ana2.c, ana3.c`: Programs, used to analyze data acquired with the Gassiplex strip readout for one, two and three detectors. Usage of the program by "./ana.3 0123 2", where "0123" is the data file's number. The second parameter can be "2" for a three detector event display of each event, "1" for plotting all events in three detectors seperately and "0" for only performing the normal analysis and plotting summary histograms. The basics were discussed in sec. 5.5.

- `buildmap.c, scaling.c`: ROOT macros, used to create the configuration files for `ana.c`. They build the channel and frontend adress to strip number mapping and the strip specific scaling factor, accounting for the different amplification factor of Gassiplex channels.

- `signals.c, signalsneg.c`: ROOT macros, used analyze data from the flash ADC for anode and mesh readout, respectively. The functionality was presented in sec. 4.5.

- `effsim.c, effsimgas.c`: ROOT macros, used to determine the geometric correction factors for efficiency calculation in the single detector and in the multi detector setup from a Monte Carlo simulation. Their principle has been discussed in sec. 4.4. The source code of `effsim.c` can be found in the appendix B.

- `inclsim.c`: ROOT macro, used to simulate the hit distribution in two Micromegas. Furthermore, the track inclination distribution was calculated (Monte Carlo). Results were compared with measurements in secs. 7.2 and 7.7.

- `driftsim.c`: ROOT macro, used to estimate the number of hit strips as a function of track inclination (Monte Carlo) for non uniform charge distribution along the particle's track. Results were implicitly used in sec. 7.6.

- `mirror.c, mirrordis.c`: ROOT macro, used to numerically calculate the induced charge on two grounded planes by the method of images. Discussed in sec. 8.1.

- `isegcontrol.c, isegload.c, isegSHQdef.c`: ROOT macros, used to control the iseg SHQ high voltage supplies via RS232. Mandatory libraries must be loaded before execution (`isegload.c`). High level routines to execute certain commands are defined in `isegSHQdef.c` and summarized in tab. A.1. The programs were introduced in sec. 3.4.

- `scattering.c`: ROOT macro, used to estimate the multiple scattering's influence on the spatial resolution (Monte Carlo). Discussed in sec. 7.6.

function	parameters	return value	description
`int initserial(TMrbSerialComm*device)`	serial port handle	0 upon success	set device parameters: baud rate 9600 bit/s, 8 bits/character, 1 stop bit, no parity, postfix (= end of each command): carriage return line feed (= \x0d\x0a in C++ code).
`TString setvoltage(*device,Int_t Channel,TString Volt)`	serial port handle, channel number, voltage (*nnnn.nn* in V)	set voltage	set the desired voltage value.
`TString setramp(*device,Channel, TString Ramp)`	serial port handle, channel number, ramp (*nnn* in V/s)	set ramp	set the desired ramp speed between 2 and 255 V/s. Hardware default is 500 V/s.
`TString getstatus(*device,Channel)`	serial port handle, channel number	status word	read the status of Channel. Reading the status register is also necessary to continue after a trip or other error.
`TString getvoltage(*device,Channel)`	serial port handle, channel number	actual voltage	get the actual voltage in V. Format is *polarity nnnnn exponent with sign* e.g. -06250-01 corresponds to 625.0 V
`TString getcurrent(*device,Channel)`	serial port handle, channel number	actual current	get the actual current in A. Format is *nnnnn exponent with sign* e.g. 00201-09 corresponds to 201 nA
`TString voltchange(*device,Channel)`	serial port handle, channel number	status word	execute voltage change to preset value.

Table A.1: High level functions written to control and monitor the parameters of the high voltage supplies iseg SHQ. Types of variables in function declarations are given only at first appearance.

Appendix B

Efficiency Simulation

```
//**********************************************************
//***    effsim.c           *****************************
//***    author: Jona Bortfeldt  ***************************
//***    date: 04.11.2010    *****************************
//***    MonteCarlo simulation of muon tracks in two   ******
//***    scintillators and one Micromegas, used to determine*
//***    the efficiency's geometric correction factor  ******
//***    execute by: .x effsim.c   **************************
#include <iostream>
#include "TF1.h"
#include "TRandom.h"

int effsim(){
  const Double_t pi=3.1415926536;
  Double_t poslow[3]; //position lower scint. (x,y,z)
  Double_t posup[3];  //position upper scint.
  Double_t posmm[3];  //position micom
  Double_t sizemmx,sizemmy,sizesclowx,sizesclowy,sizesclowz,sizescupx,sizescupy,sizescupz;
  Double_t phi, theta;
  Double_t direc[3];  //muon's direction vector
  Double_t check[3];
  Double_t checkup[3];
  Double_t checklow[3];
  Double_t ran;
  Double_t posx,posy,posz;
  Double_t hitsup,hitsmm;
  Double_t ratio;
  const Int_t kmax=10000; //number of muons to do for each grid point

  //set detector positions
  posup[0]=20.;
  posup[1]=-5.;
  posup[2]=100.;
  posmm[0]=10.;
  posmm[1]=5.;
  posmm[2]=72.;
  poslow[0]=0.;
  poslow[1]=0.;
  poslow[2]=0.;

  //set detector dimensions
  sizesclowx=130.; //lower scint.
```

```
sizesclowy=90.;
sizesclowz=45.;
sizescupx=90.;    //upper scint.
sizescupy=130.;
sizescupz=45.;
sizemmx=100.;     //micromegas
sizemmy=90.;

TF1* f1 = new TF1("f1","(cos(x)*cos(x))",0.,pi/2.);
hitsup=0;
hitsmm=0;

for(posz=poslow[2];posz<=sizesclowz;posz+=sizesclowz){
  for(posx=0;posx<=sizesclowx;posx+=10){
    for(posy=0;posy<=sizesclowy;posy+=10){
      for(Int_t k = 0;k<kmax;k++){
        //draw muon's direction of flight
        phi = gRandom->Uniform(0.,2.*pi);
        theta=f1->GetRandom();
        //calculate the direction-vector
        direc[0]=cos(phi)*sin(theta);
        direc[1]=sin(phi)*sin(theta);
        direc[2]=cos(theta);

        //check if the muon hit the upper scintillator
        for(Int_t i=0;i<3;i++){
          check[i]=direc[i]/direc[2];
          checkup[i]=check[i]*(posup[2]+sizescupz-posz);
          checklow[i]=check[i]*(posup[2]-posz);
        }
        checkup[0]=checkup[0]+posx;
        checkup[1]=checkup[1]+posy;
        checklow[0]=checklow[0]+posx;
        checklow[1]=checklow[1]+posy;
        if(((checkup[0]>posup[0])&&(checkup[0]<(posup[0]+sizescupx))
        &&(checkup[1]>posup[1])&&(checkup[1]<(posup[1]+sizescupy)))
        ||((checklow[0]>posup[0])&&(checklow[0]<(posup[0]+sizescupx))
        &&(checklow[1]>posup[1])&&(checklow[1]<(posup[1]+sizescupy)))){
          hitsup++;

          //check if the muon also hit the mm
          for(Int_t i=0;i<3;i++){
            check[i]=direc[i]/direc[2];
            check[i]=check[i]*(posmm[2]-posz);
          }
          check[0]=check[0]+posx;
          check[1]=check[1]+posy;
          if((check[0]>posmm[0])&&(check[0]<(posmm[0]+sizemmx))
          &&(check[1]>posmm[1])&&(check[1]<(posmm[1]+sizemmy))){
            hitsmm++;
          }
        }
      }//end of k-loop
    }
  }
}
ratio=hitsmm/hitsup;
cout<<"total hits upper scintillator = "<<hitsup<<endl;
```

```
  cout<<"total hits micromegas = "<<hitsmm<<endl;
  cout<<"ratio = "<<ratio<<endl;
  return 0;
}
```

Acknowledgments

Selbständigkeitserklärung

Ich versichere hiermit, die vorliegende Arbeit mit dem Titel

Development of Micro - Pattern Gaseous
Detectors – Micromegas

selbständig verfasst zu haben und keine anderen als die angegebenen Quellen und Hilfsmittel verwendet zu haben.

Jonathan Bortfeldt

München, den 23. November 2010